Exploration Investigation Requirements Document

For

SAME

a.k.a.

Smoke Aerosol Measurement Experiment

Rev. 2.0

February 25, 2005

Principal Investigator: David Urban; NASA Glenn Research Center
Co-Investigators:
George Mulholland: National Institute for Standards and Technology
Zeng-guang Yuan: National Center for Microgravity Research.
Jiann Yang: National Institute for Standards and Technology.
Thomas Cleary: National Institute for Standards and Technology

Signature Page

Title of Experiment: SAME

Final Post RDR version

Date: February 25, 2005

Revision: 2.0

David Urban Principal Investigator		Signature		Date

CONCURRENCES
NASA Glenn Research Center

Gary Ruff SAME Project Scientist / FPDS Center Element Lead		Signature		Date

William Sheredy SAME Project Manager		Signature		Date

Tom Sutliff FPDS Center Element Program Manager		Signature		Date

Merrill King FPDS HQ Program Element Manager		Signature		Date

Carl Walz Assoc. Director: Life Support and Habitation		Signature		Date

Executive Summary

Smoke detection for spacecraft fires is not fully developed. To date, the only data on the smoke size distribution for spacecraft fires are from the CSD experiment and the only background dust measurements are from a single shuttle mission. Existing spacecraft smoke detectors either suffer from insensitivity to certain events or form numerous false alarms due to dust. Future missions will require increased reliability that cannot be assured with the current state of knowledge. To address this concern, an experiment is defined to determine the particle size distribution of the smoke from a variety of overheated spacecraft materials relevant to microgravity fires. The experiment will enhance the concept of the Comparative Soot Diagnostics (CSD) experiment with additional diagnostic measurements and modifications to enable operations in the Microgravity Science Glovebox (MSG) on the International Space Station (ISS). The objective of the program is to provide the data that spacecraft designers need to properly design and implement fire detection in spacecraft. This proposed work ties directly to NASA's exploration goal of improving the safety and reliability of our spacecraft and extraterrestrial habitats.

Spacecraft smoke detectors must detect smoke consisting of a variety of particulate types. Hydrocarbon flames typically produce soot while overheated plastics produce structures assembled from recondensed polymer fragments. Other materials (paper and silicone rubber), when smoldering, produce a smoke that is composed of liquid droplets of recondensed pyrolysis products. Systems such as the solid-fuel oxygen-generators are likely to produce particulate that is composed of metal oxides and inorganic particles composed of elements from the oxygen generator fuel. The nucleation and growth processes for these different types of smokes are quite varied and consequently the particle structure varies with the source material. Given the increased residence times caused by the absence of buoyant acceleration it is logical that low-gravity smoke particulate size distributions could be significantly different from smoke produced in 1-g. In the absence of low-gravity aerosol data, the current spacecraft smoke detector designs are based upon 1-g experience. The CSD experiment, which flew in the Glovebox on STS 75, provided the first practically useful μg data concerning the performance of NASA's smoke detectors and provided particle size information for 3 types of solid smoke particulate. The most important finding of CSD was that for liquid smoke aerosols, the microgravity performance of the space shuttle (STS) smoke detector was substantially reduced from that in normal gravity. It is hypothesized that this performance difference was due to extended growth of the liquid smoke particulate in low-gravity due to the enhanced residence times in high smoke concentration regions.

One of the major goals of the space experiment is to quantify the sizes that the liquid smoke particulate achieves in low gravity and to relate the droplet size distribution to the smoke generation and smoke transport conditions in the experiment. This will be accomplished by extending the CSD concept to provide in situ particle size information for several smoke aerosols (solid and liquid). The enhancements will be made by using commercial diagnostic techniques to provide droplet size information. Due to space, crew time and mass limitations, the measurements will be aggregate moments of the aerosol size distribution. By combining three such moments, it is possible to calculate the particle arithmetic mean diameter, the diameter of average mass and, by assuming a log-normal particle distribution, the geometric mean diameter and standard deviation. The experimental design and practical application of the data will be enhanced by the development of a numerical code to predict the smoke droplet growth as a function of the fuel pyrolysis rate, the thermodynamic properties of the pyrolysis vapor, and the flow environment.

The results of the experiment will include statistics of the smoke particle size distribution for several practical spacecraft materials for a range of smoke generation conditions and measurement of a readily modeled reference material for validation of smoke growth models. The work fits directly into critical needs of the future manned exploration missions by providing the data needed for the design and implementation of spacecraft smoke sensors for future manned missions.

Table of Contents

List of Tables

List of Figures

Nomenclature

μg	microgravity
n(d)	number of particles of size d
N	total number of particles
N_o	particle number concentration at time t=0 (particles/volume)
K_o	particle coagulation coefficient (volume / time)
t	time
N(t)	particle number concentration at time t (particles/volume)
$f_N(D)$	probability density function of the number distribution (particles/volume/ diameter)
D, d_p, Dp	particle diameter
dN	number of particles per volume with diameter between D and D + dD.
M_i	The ith moment of the number distribution

λ	wavelength
θ	scattering angle
D_g, d_g	geometric mean diameter (arithmetic mean of the distribution of ln d_p)
CMD	Count Median Diameter, for a lognormal distribution CMD = D_g
σ_g	geometric standard deviation (GSD) a(standard deviation of the distribution of ln d_p)
M_0	number concentration (zeroth moment of the number distribution)
M_1	first moment (first moment of the number distribution)
M_3	mass concentration moment (third moment of the number distribution)
M_i	ionization detector moment
M_s	light scattering moment
$D_{0.5}$	arithmetic mean diameter
$D_{1.5}$	diameter of average mass = $\left[\sum nd^3 / N\right]^{1/3}$

Acronyms/Abbreviations

AMD	Arithmetic mean diameter
CMD	Count Median Diameter, for a lognormal distribution CMD = D_g
CSD	Comparative Soot Diagnostics
COTS	Commercial-off-the-shelf
DOP	Dioctyl phthalate
DBP	Dibutyl phthalate
EIRD	Exploration Investigation Requirements Document
IR	infra-red
ISS	International Space Station
MMAD	Mass Median Aerodynamic Diameter
MMD	Mass mean diameter
MSG	Microgravity Science Glovebox
NASA	National Aeronautics and Space Administration
NIST	National Institute for Standards and Technology
RDR	Requirements Definition Review
STS	Space Transportation system, a.k.a the Space Shuttle and the Orbiter
UV	ultra-violet
TEM	transmission electron microscope

1 Introduction and background

In the earliest missions (Mercury, Gemini and Apollo), the crew quarters were so cramped that it was considered reasonable that the astronauts would rapidly detect any fire. The Skylab module, however, included approximately 30 UV-sensing fire detectors (Friedman, 1992). These devices were limited to line-of sight and were reported to have difficulties with false alarms. The Space Shuttle was developed in a time (1970's) of rapid progress in smoke detection for terrestrial applications (Bukowski and

Mulholland, 1978). At the time, ionization detectors were becoming readily available but photoelectric (scattering or obscuration detectors) were generally unavailable due to the difficulty of producing stable light sources. There was no data available concerning the smoke particle size distribution in low-gravity and the database of normal-gravity smoke characteristics was a fraction of what is available today. There was also no data on spacecraft dust particle size distributions but the absence of gravitational settling suggested that there would be more large particles than are seen on earth. Consequently it is understandable that the Orbiter design employed a variant of the accepted ground based approach (ionization detectors). The Orbiter has 9 particle-ionization smoke detectors in avionics cooling air return lines in the mid-deck and flight deck and SpaceLab had six additional particle-ionization smoke detectors in the avionics lines. (Martin and DaLee 1993) While the design rationale is not completely known, Celesco™ (later Brunswick Defense™) based their design on data that suggested incipient fires could be discriminated by looking for particulate in the 0.4 to 0.7 μm range (L.G. Barr in National Research Council 1975). Use of a pump provided the opportunity to employ a particle separator allowing rejection of particulate larger than 1μm consistent with their understanding that incipient smoke particulate was smaller than 1 μm. Furthermore, since ionization chambers are susceptible to the ambient air velocity, implementing an ionization detector in a flow duct was probably facilitated by the use of an air pump to control the air flow through the smoke detector. This air pump increased the power requirements and reduced the operational life for the detectors.

At the time the International Space Station (ISS) was being developed, stable laser-diode light sources were readily available. Consequently, terrestrial smoke detectors using light scattering were becoming more readily available. This provided the opportunity to produce a detector that was substantially lower power (1.5 Watts versus 9 Watts for the shuttle detector) (Steisslinger et al. 1993) and with no moving parts and therefore quieter with a much longer operational life. The choice was supported by data indicating that early smoldering fires produce larger particulate than established flaming fires (Bukowski and Mulholland 1978). The designated detectors for the ISS are laser-diode, forward-scattering, smoke or particulate detectors. Their sensitivity is greatest for particles larger than 1 μm with sensitivity extending down to 0.6 μm. The current requirements for the ISS call for two detectors in the open area of the module, and detectors in racks that have cooling air-flow (McKinnie, 1997). It is interesting to note that the ISS and the Orbiter detectors have particle sensitivities that are nearly mutually exclusive. In both cases the designs were based upon the best available data however, due to the complete absence of low-g data concerning the nature of particulate and radiant emission from incipient and fully developed low-g fires, all of these detector systems were designed based upon 1-g test data and experience. As planned mission durations and complexity increase and the volume of spacecraft increases, the need for and importance of effective, crew-independent, fire detection grows significantly. At this point there are very limited measurements of low-gravity smoke particulate size distributions and limited measurements of the ambient cabin dust size distribution. The objective of this project is to improve the reliability of spacecraft fire detection systems by measuring the critical characteristics of microgravity smoke and ambient dust needed to properly design and implement spacecraft smoke detectors.

1.1 Scientific background

1.1.1 Spacecraft fire detection

In 1996 the Comparative Soot Diagnostics Experiment (CSD) flew in the Orbiter Middeck as a Glovebox payload (Urban, 1997, A & B). The CSD experiment was designed to produce small quantities of smoke from several sources and determine the response of the ISS and Orbiter smoke detectors to these sources. In addition, a goal was to obtain particulate samples from these sources. As will be described below, the experiment operated very effectively and marked differences in the performance of the detectors compared to their behavior in 1-g were observed. In extreme cases, the detector used in the Orbiter was completely blind to easily visible smoke from sources that were readily detected in 1-g. It is hypothesized but as yet unverified that this performance difference was due to enhanced growth of liquid smoke droplets in low-g.

As described by Friedman (1994) there have been six overheat and failed component failures in the NASA Orbiter fleet (Space Transportation System or STS). None of these events spread into a real fire but as mission durations increase, the likelihood of failures increases. The experience on Mir in 1997

has shown that failure of oxygen generation systems can have significant consequences. As a result, improved understanding of spacecraft fire detection is critically needed. As will be shown below, the CSD results clearly demonstrate that solid-particulate smoke-aerosols in low-g have larger average dimensions than those produced in 1-g and that spacecraft smoke detector design cannot be based on 1-g understanding and experience. Consequently a more complete data base of likely spacecraft smoke particulate is needed, particularly in the pre-fire pyrolysis period. The CSD experiment provided significant data on solid particle smoke sources but due to limitations in the design did not produce particle sizes for liquid aerosol smokes. Liquid smoke aerosols are produced by many pyrolyzing flammable materials and the smoke droplets can be expected to coalesce on contact, producing spherical particles, with significantly different properties from the aggregate structures produced by solid particulate. The objective of the SAME experiment is to bring improved diagnostic technology to the measurement of smoke particulate for various practical materials to allow more effective characterization of the particle size distribution. A modeling program will be developed to examine the parameters that control the growth of these smoke droplets between the source and the sensor. These results are critically needed to allow design of reliable smoke detection systems for long duration low-gravity missions.

1.1.2 Other results in low-gravity smoke properties and detection

Prior to CSD, no combustion-generated particulate samples had been collected near the flame zone for well-developed microgravity flames. All of the extant data either came from drop tower tests and therefore only corresponded to the early stages of a fire or were collected far from the flame zone. The fuel sources in the drop tower tests were restricted to laminar gas-jet diffusion flames (Ku et al. 1995) and very rapidly overheated wire insulation (Paul et al. 1993). The gas-jet tests indicated, through thermophoretic sampling, that soot primaries and aggregates (groups of primary particles) in low-gravity may be significantly larger than those in normal gravity (1-g). This raises new scientific questions about soot processes as well as practical issues for particulate size sensitivity and detection/alarm threshold levels used in on-orbit smoke detectors. Preliminary tests in the 2.2 second drop tower suggest that particulate generated by overheated wire insulation may be larger in low-g than in 1-g. Transmission Electron Microscope (TEM) grids downstream of the fire region in the Wire Insulation Flammability experiment (Greenberg, Sacksteder and Kashiwagi 1995) as well as visual observation of long string-like aggregates, further confirm this suggestion. The combined impact of these limited results and theoretical predictions is that, as opposed to extrapolation from 1-g data, direct knowledge of low-g combustion particulate is needed for more confident design of smoke detectors for spacecraft.

Subsequently, the Laminar Soot Processes (LSP) experiment sampled soot from ethylene and propane gas jet diffusion flames in long-term low gravity (Urban, 1997) the soot primary particles were typically twice the size of soot from similar normal gravity flames and the aggregates were more than an order of magnitude larger. Srivastava, McKinnon and Todd (1998) studied particulate from overheated Teflon wire in the 2.2 second drop tower; although detailed particle statistics were not reported, the aggregates were generally larger than in 1-g. One of the most surprising results was the determination that the Teflon wire coloring agent had a very strong effect on the particle size distribution and morphology.

The only spacecraft background aerosol particulate measurements to date were made on the shuttle on STS 32 in 1990 (Liu et al. 1991). These measurements included the results from two cascade impactors and a light scattering device. The two impactors reported a bimodal particle size distribution with ~ 40% of the particles in each of the 2.5 to10 μm and >100 μm ranges. The other two ranges <2.5 μm and 10to 100 μm were very lightly populated (Table 1-1). Each impactor samples approximately 15 m3 of air over approximately 30 hours. These results showed substantially higher concentrations than typical indoor measurements. These results were supported by the light scattering instrument which made 17 measurements in 12 locations, all of these reported mass concentrations ranging from 50 to 70 $\mu g/m^3$.The low particle levels in the < 2.5 μm bin suggest a zone of opportunity for spacecraft fire detection since typical normal gravity fires produce substantial particulate in this size range (Bukowski et al. 2003, Bukowski and Mulholland 1978), and the average sizes that were recorded by CSD (below) are in this size range. However more complete particle size statistics are needed.

Table 1-1: Impactor data from STS 32

(from Liu et al., 1991)

Airborne Particle Mass Concentration: Comparison of STS-32 to Indoor Environments

Sample Location[1]	Sampler[6]	Particle Size Range <2.5µm	2.5-10µm	10-100µm	≥100µm	Total
		Mass Concenetration, µg/m³				
Shuttle[2]	SPS-1	2.3	24.1	4.8	28.1	59.3
Shuttle[3]	SPS-2	2.1	13.4	6.2	31.8	53.5
Home[4]	Ave	3.0	3.0	1.0	1.5	8.5
Office	Ave	3.4	3.2	2.7	1.9	11.2
Laboratory[5]	Ave	2.9	4.8	2.0	2.4	12.1
		Ave Mass Concenetration, µg/m³				
Ave. Shuttle		2.2	18.7	5.5	30.0	56.4
Ave. Indoor Environment		3.1	3.7	1.9	1.9	10.6
		Ratio of Mass Concentration				
Shuttle/Indoor		0.71	5.1	2.9	15.8	5.3

[1]Sampling time 24 hours except for STS-32 samples

[2]STS-32: MET 0/21:34 - 1/23:09: sampling time = 25 hr 35 min

[3]STS-32: MET 6/21:26 - 8/6:34: sampling time = 33 hr 8 min

[4]Typical of data obtained from 2 days in home and 1 day in apartment

[5]Typical of data obtained from 3 days in laboratory

[6]Ave = average of data from SPS-1 and SPS-2

1.1.3 Residential fire detection

An excellent review of fire detection technology at the approximate time the Space shuttle was under development is provided by Bukowski and Mulholland (1978) and a summary of the performance of current technology can be found in Bukowski et al. (2003). In general, well ventilated flames and established fires emit particulate with sizes tending toward the size range to which ionization detectors are more sensitive than optical detectors. On the other hand, smoldering fires and over-heated (pyrolyzing) materials produce larger particulate, owing to the large amount of condensed, unoxidized fuel pyrolysis products and the incomplete oxidation. For these larger particles, light scattering/obscuration detectors are more appropriate. Ionization detectors were favored in the 1970's though the mid 1990's due to the difficulty of producing light sources that would remain stable for several years. The advent of improvements in light emitting diode and diode laser technology has reduced the cost and increased the stability of photoelectric fire detectors.

The relative sensitivity of the two technologies is shown in figure 1-1 (Mulholland and Liu, 1980)

which shows that below particle diameters of approximately 0.2 μm, ionization detectors are more sensitive. For particle sizes above this, light-scattering is exponentially more sensitive. This further sensitivity difference is amplified by the fact that particle mass increases with diameter cubed so for the same mass loading of smoke, the particle number count will decrease as the diameter increases. Ionization detectors are, to first order, proportional to the particle diameter whereas light scattering is proportional to the diameter cubed. The net result is that as particle diameter increases beyond the wavelength of the light, light scattering detectors become more sensitive than ionization detectors.

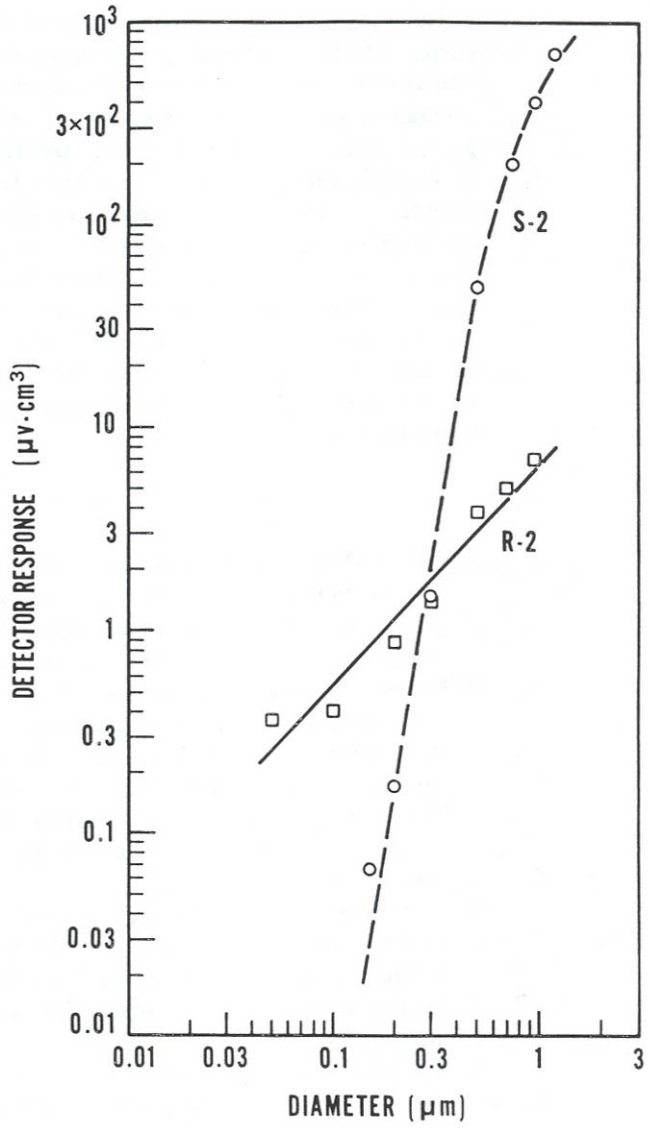

Figure 1-1. Ionization and scattering detector response as a function of particle size.
The size response function ((detector output –background)/ particle concentration) is plotted against the diameter for monodisperse aerosol for light scattering (S-2) and ionization (R-2) detectors (Mulholland and Liu, 1980).

In an extensive comparative performance characterization in residential housing, Bukowski et al. (2003) tested ionization, photoelectric and CO detectors against a variety of smoke and nuisance sources. No detector was the clear winner. As expected, the ionization detectors performed better than the others for flaming fires but responded much more slowly than the scattering detector for the smoldering cases. The CO detector performance was similar to but slightly slower than the scattering detector. In general, both smoke detector designs provided positive escape times if detectors were placed on every level

and every bedroom. Ionization detectors were prone to nuisance alarms during early stages of cooking activities even when no visible smoke was present. Although further work is still indicated to implement the results of the residential testing to date, the effectiveness of residential smoke detector technology and acceptable nuisance alarm levels have been demonstrated. Corresponding understanding for the spacecraft environment is needed to ensure adequate protection for future spacecraft.

1.1.4 Current spacecraft smoke detector designs

As discussed previously, the shuttle smoke detector was designed by Celesco/Brunswick Defense™ to discriminate smoke from dust via an inertial separator which limited the material entering the detector to particles below 1 μm to provide false alarm rejection. This was supported by results which showed that, for some materials heated slowly as in the very early stages of some fires, the particulate can be very small, (Chuan and Chen 1986), (L.G. Barr in National Research Council 1975). The design (Fig. 1-2) consists of a dual-chamber ionization detector that is in the flow path created by a vane pump. This vane pump provides some active sampling capability and also the flow for an inertial separation system which is designed to make the detector insensitive to particulate larger than 1 to 2μm, depending upon the particle density. These advantages are offset by fairly large power consumption (9 Watts), fan noise, and limited life due to the moving parts. The detector produces a discrete alarm signal and two analog signals related to the detected smoke density.

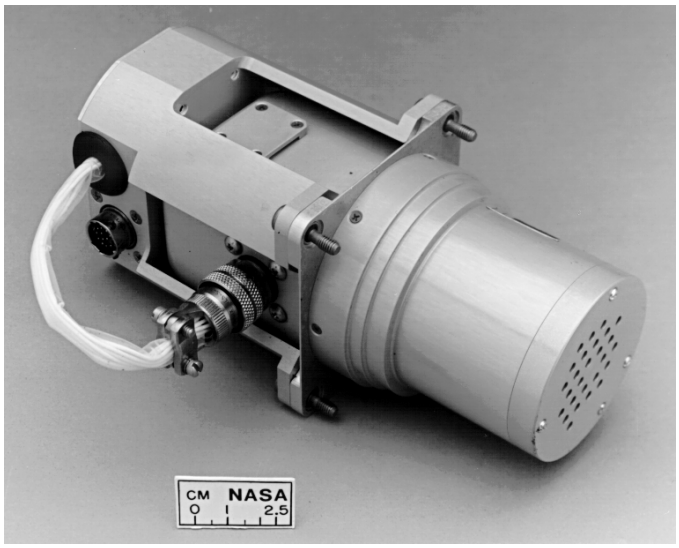

Figure 1-2. Brunswick Defense™ smoke detector used in the NASA shuttle fleet.
The inlet is on the right and the gas is expelled out the small plate on the top.

The design developed for the ISS by Allied Signal™ (Fig. 1-3) consists of a 2-pass laser diode to sense forward scattered light (30 degrees). There is also a zero degree obscuration system that is used as a measure of the beam strength. The system is designed to alarm based on the magnitude of the scattered light signal referenced to the beam intensity. Some level of dust discrimination is provided based on frequency analysis of the scattered light signal. The system is less sensitive to particles smaller than the wavelength of the laser (near IR) than it is to larger particles. The minimum reported sensitivity is 0.3 μm (Steisslinger et al 1993). It draws relatively little power (1.5 W) and it has a long operational life. The current planned alarm value is 2 volts which is calibrated to 1% obscuration per foot (visible light) for punk type smoke in a smoke box. The net result of these design choices is that that these two detector systems have nearly non-overlapping particle size sensitivities. The STS detector deliberately rejects particles in the size regime to which the ISS detector is most sensitive.

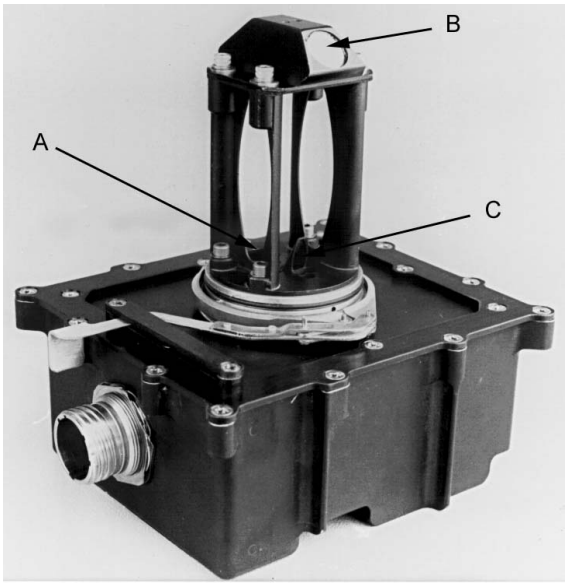

Figure 1-3. Allied Signal/Honeywell light-scattering smoke detector used in the ISS.
The near IR laser beam emerges from the enclosure into the top assembly (A) and is reflected by two mirrors (one visible at top right (B)) and is then reflected back to the sensors in the enclosure (C). One sensor detects the forward scattered light and is referenced by another sensor that looks directly at the incident beam.

The performance of these two detectors has been compared in normal gravity (Steisslinger et al 1993, McLin 1993). Consistent with expectations, for cases where large particles were expected (punk smoke) the initial response of both detectors was about the same but the ISS detector reached the alarm threshold more rapidly. For sources of smaller particle-size smoke (over heated wire) the STS detector was quicker both in initial response and in time to alarm. The implementation (alarm threshold selection) of both of these systems in microgravity is hampered by the lack of knowledge of their performance against low-gravity combustion generated particulate. This performance difference is consistent with the differences in their mutually exclusive particle size sensitivity. These tests suggest that sensitivity to a range of particle sizes is desirable given the performance differences seen for two expected smoke types (wire insulation and cellulose pyrolysis products).

1.2 Background: CSD experiment design and results

1.2.1 Experiment design

The CSD experimental hardware consisted of two modules named the Near-Field Module and Far-Field Box as shown in figure 1-4.The Near-Field Module was installed inside the Glovebox and contains the sample and the near field diagnostics. The Far-Field Box was external to the Glovebox and contains two spacecraft smoke detectors. Products from the near field tests were transported to the Far-Field Box and subsequently back into the Glovebox via Teflon hoses which entered the Glovebox through ports in the airlock door. All of the combustion products were contained in either the Glovebox or the Far Field Box; by the time the experiment was completed, all of the products were returned to the Glovebox.

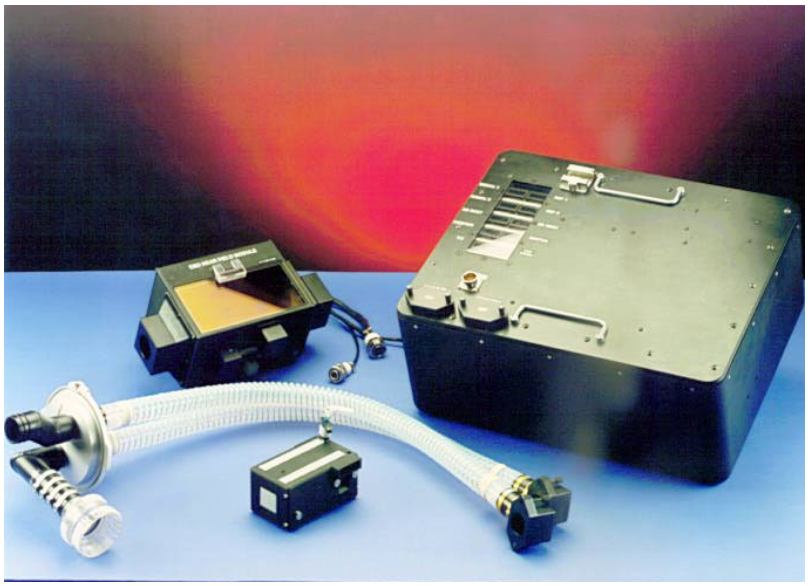

Figure 1-4. CSD Hardware

The Near Field Module is to the back left and the Far Field Box is to the right. Connecting hoses and thermophoretic sampler are in the front.

The Near-Field Module (Fig 1-5) consisted of a small test chamber fitted with a sample carrier that held the sample being tested. A small fan blew air from the Glovebox into the right side of the chamber past the sample and out the left side where it entered the hose to the Far-Field Module. The sample was ignited or overheated by a resistively heated Kanthal™ wire. The smoke particulate was sampled by a rake of thermophoretic probes and smoke production was detected by a laser light extinction system.

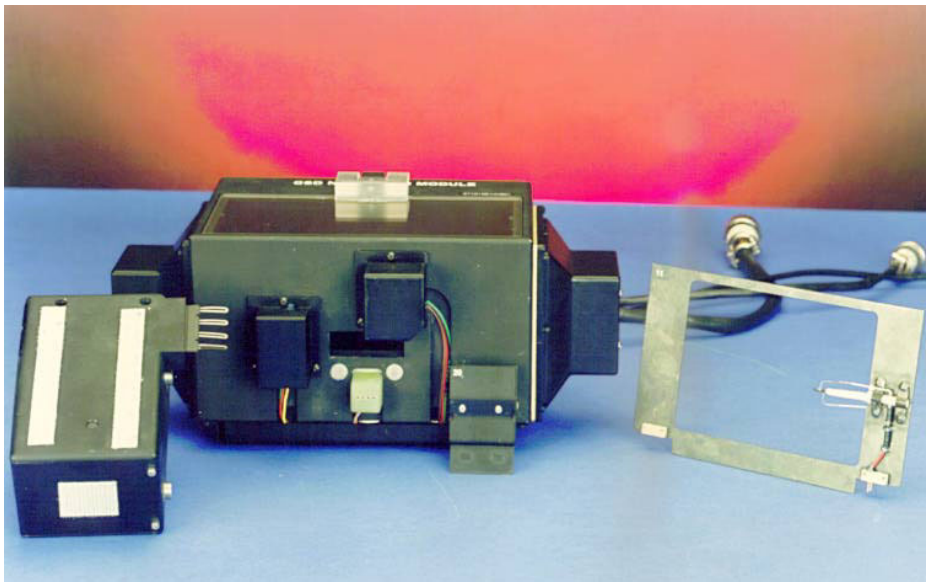

Figure 1-5. Near Field Module
Deployed thermophoretic probe on left and a sample card holding a candle to the right.

The Far Field Box (Figure 1-6) contained a duct and a fan to transport the smoke from the Near Field Module to two spacecraft smoke detectors, one matching the STS detector and the other identical to the ISS detector except that its signal was amplified by a factor of 6.6 over the ISS standard. The

analog signals from the various instruments were displayed by digital readouts on the Far Field Box where they were recorded by a video camera for later transcription.

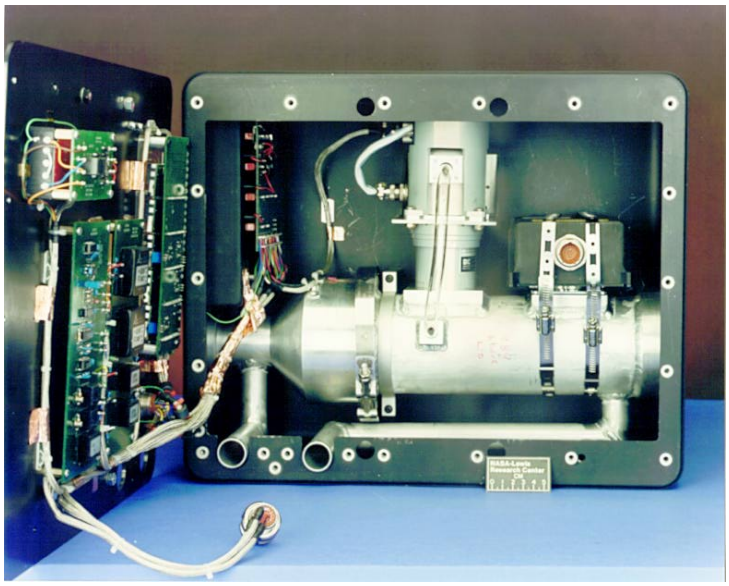

Figure 1-6. Interior of Far Field Box

Visible is the interior duct with the ISS detector on the right and the STS detector in the center.

1.2.2 Procedure and operational sequence and data reduction

The crew installed the near field hardware in the Glovebox, attached the Far Field Box to the Glovebox, and positioned the video cameras. The operator then ran the self diagnostic procedures on the two smoke detectors and activated the video cameras, turned on the igniter for a predefined period of time (15 to 60 seconds), and initiated the thermophoretic soot samplers to sample the smoke. The actual duration of each combustion event was typically 2 minutes. After flight, the particulate collected on the thermophoretic probes were analyzed using a Transmission Electron microscope (TEM) to determine primary and aggregate particle dimensions. The remains of the samples were weighed to determine their mass loss. The digital data was transcribed from the video record and analyzed to determine the response of the detectors. Once the flight mass loss rates were determined, 1-g operation conditions to produce the same loss were determined.

1.2.3 CSD results

In all, 25 tests were performed, the bulk of which were overheated material tests in which the heating level was established to produce a target weight loss rate without causing the sample to develop a sustaining combustion reaction. The intent of these tests was to produce smoke typical of an incipient fire where much of the material is being heated but has not yet ignited. The candle tests and one of the paper tests were combustion tests where the samples were ignited so the combustion products could be observed. The results of these tests are discussed in detail in Urban, Griffin and Gard (1997 a & b), however a general summary follows.

The smoke sources can be divided into three types based upon the type of smoke they emitted: the candle and burning paper produced soot, the Teflon and Kapton produced particles composed of ,solid, recondensed polymer and the silicone rubber and p[pyrolyzing paper produced liquid droplets of pyrolysis products. For the candle tests, the duct air flow was used to drive the candle flame past the smoke point, causing it to emit soot. These soot tests produced varied results between the two detectors as shown below (Figs. 1-7 and 1-8). In figure 1-7, both detectors showed rapid detection of the soot. In the case of figure 1-8, the STS detector shows a strong signal while the ISS detector signal

is quite weak considering this detector has a higher than normal amplification level. Figure 1-9 is a video image of the candle flame, the horns on the edges for the flame tip are indicative of soot emission (Urban et al. 1997).

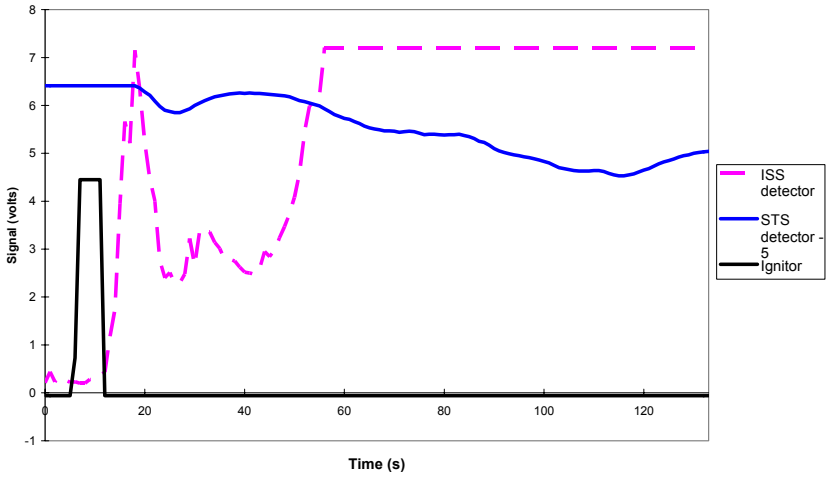

Figure 1-7. CSD results from candle test 16

Traces of smoke detector signals as a function of time for a candle test 16. The initial peak on both detectors is wax vapor released by the ignition process. The STS detector shows increasing downward deflection with increased smoke level, the ISS detector deflects upward.

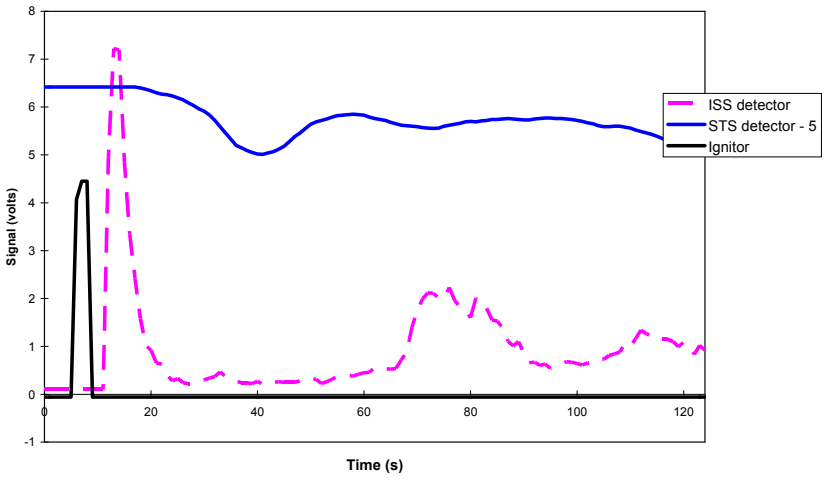

Figure 1-8. CSD results from candle test 6

Traces of smoke detector signals as a function of time for a candle test 6. The initial peak on both detectors is wax vapor released by the ignition process. The STS detector shows increasing downward deflection with increased smoke level, the ISS detector deflects upward.

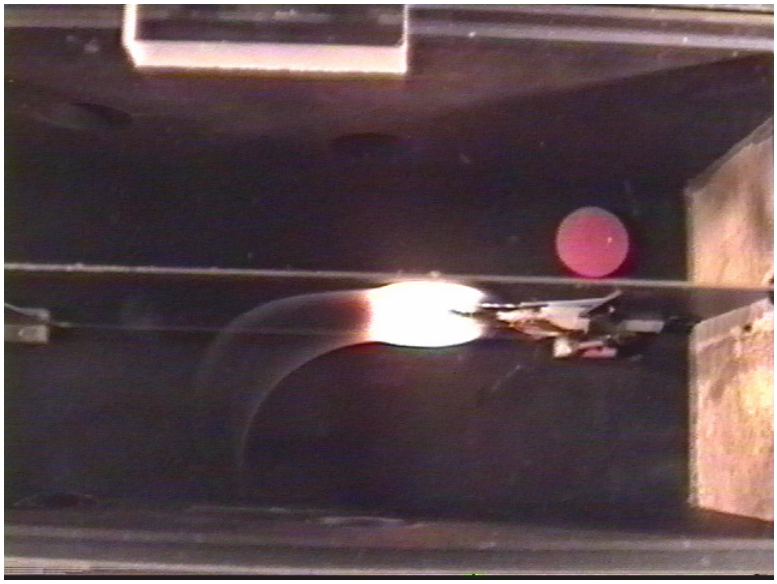

Figure 1-9. Image of candle test 16

Air flow is from right to left.

Testing with the Teflon™ and Kapton™ produced lower overall smoke concentrations. In the case of the Kapton tests, the STS detector showed an early peak followed by a rapid return to baseline while the ISS detector reported signal for another minute (fig 1-10). This result may be an artifact of the flow environment or a result of the fact that the Kapton wire used on the shuttle uses a combination of Kapton™ and Teflon™ layers and so the STS detector may be responding to only one of these materials. Figure 1-11 shows the smoke emission during the test. Similar results were seen with the Teflon™ testing (figs 1-12 and 1-13).

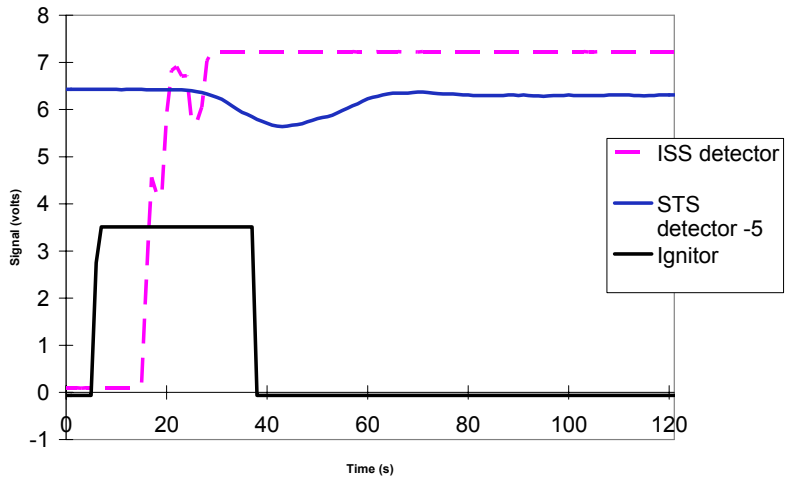

Figure 1-10. CSD results from Kapton™ test 9

Traces of smoke detector signals as a function of time for a Kapton™ test 9. The STS detector shows increasing downward deflection with increased smoke level, the ISS detector deflects upward.

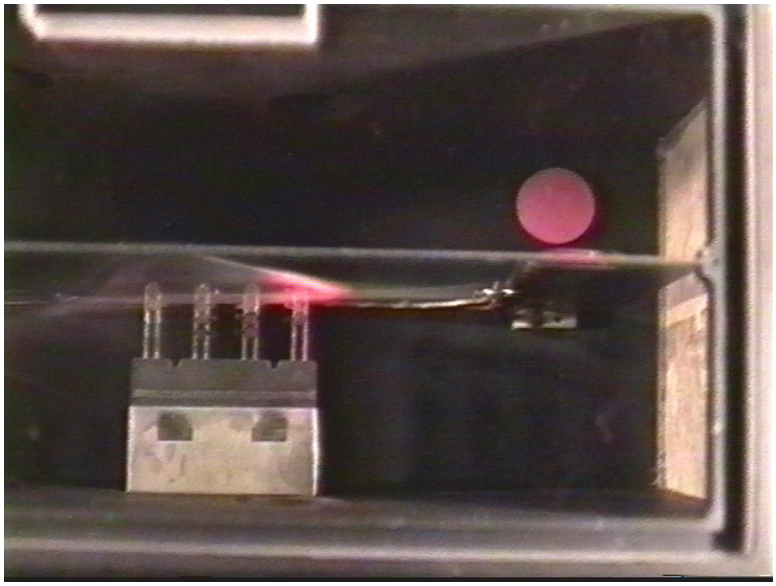

Figure 1-11. Image of smoke production during Kapton™ test 9

Air flow is from right to left. The thermophoretic sampler probe is in the deployed position in the middle of the image. The red glow from the smoke is light scattered from a laser.

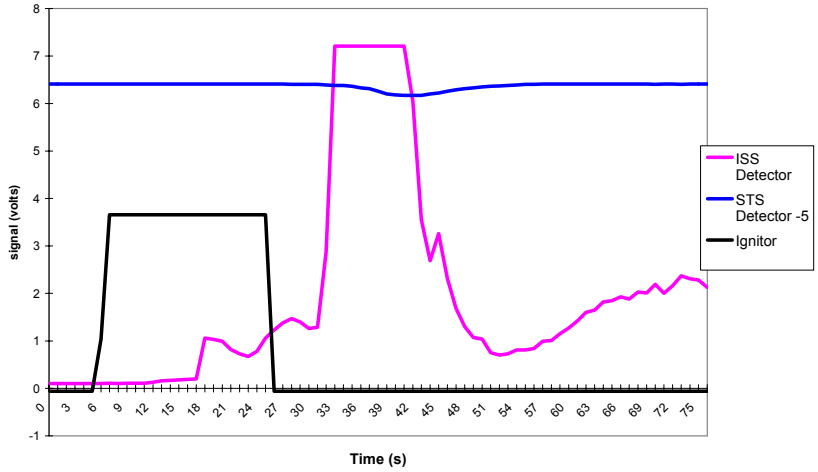

Figure 1-12. CSD results from Teflon™ test 13

Traces of smoke detector signals as a function of time for a Teflon™ test 3. The STS detector shows increasing downward deflection with increased smoke level, the ISS detector deflects upward.

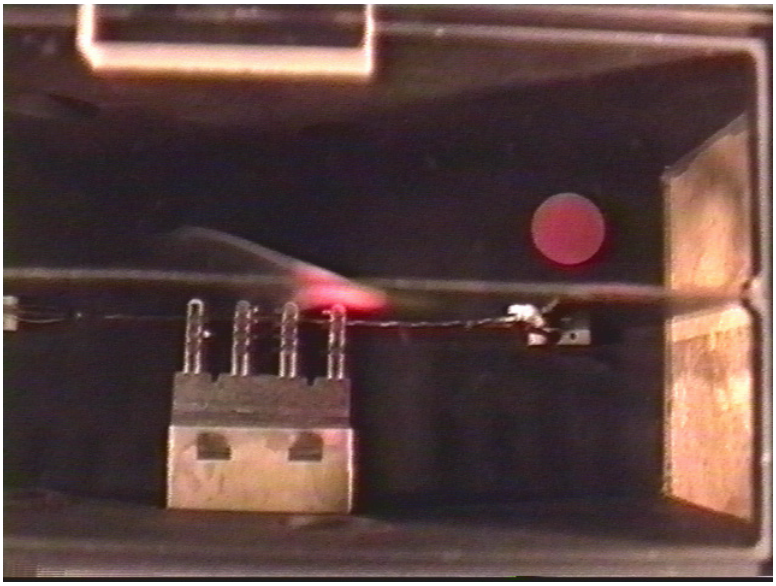

Figure 1-13. Image of smoke production during Teflon™ test 13

Air flow is from right to left. The thermophoretic sampler probe is in the deployed position in the middle of the image. The red glow from the smoke is light scattered from a laser.

The liquid smoke producing samples produced very different results as seen in figure 1-14 and 1-15 for the silicone rubber. Despite producing dense smoke that was clearly visible, the STS detector showed virtually no signal while the ISS detector saturated.

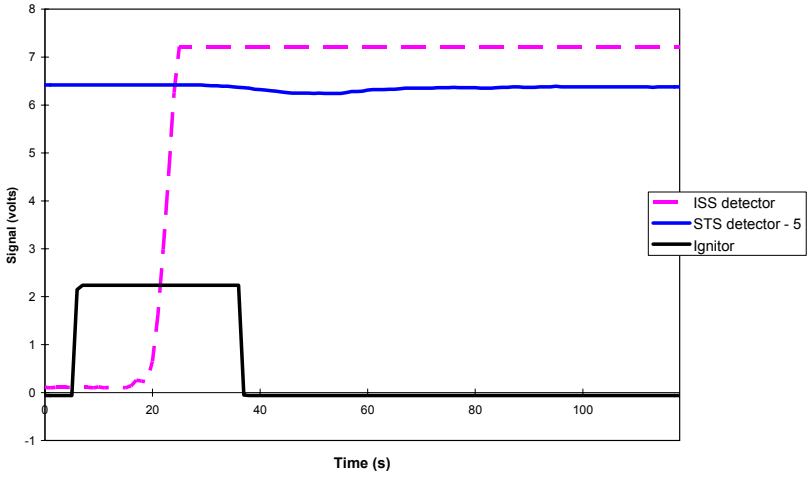

Figure 1-14. CSD results from silicone rubber test 7

Traces of smoke detector signals as a function of time for a silicone rubber test 7. The STS detector shows increasing downward deflection with increased smoke level, the ISS detector deflects upward.

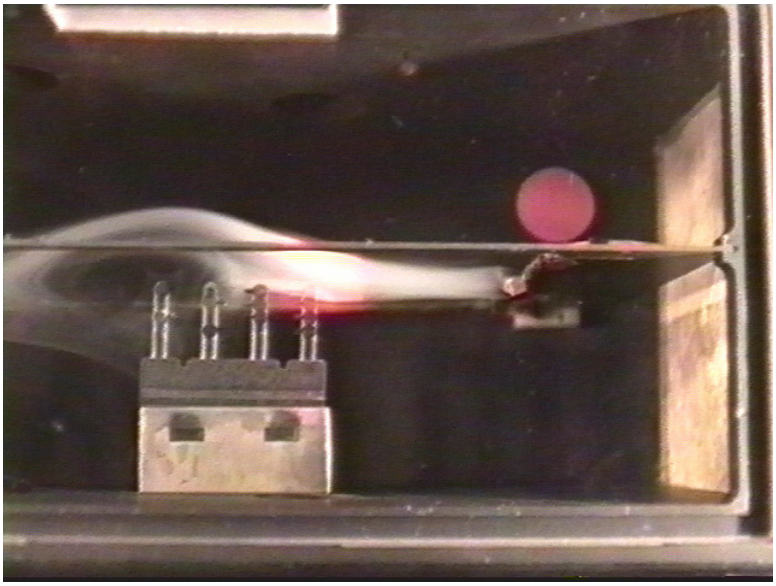

Figure 1-15. Image of smoke production during silicone rubber test 7

Air flow is from right to left. The thermophoretic sampler probe is in the deployed position in the middle of the image. The red glow from the smoke is light scattered from a laser.

The approach for the pyrolyzing paper samples was to heat them below the ignition temperature so they produced smoke without ignition. This produced similar results to the silicone rubber with virtually no signal on the STS detector and a strong signal on the ISS detector. Notably in one test the sample ignited and the STS detector signal changed from the baseline to a substantial peak (Figures 1-16 and 1-17).

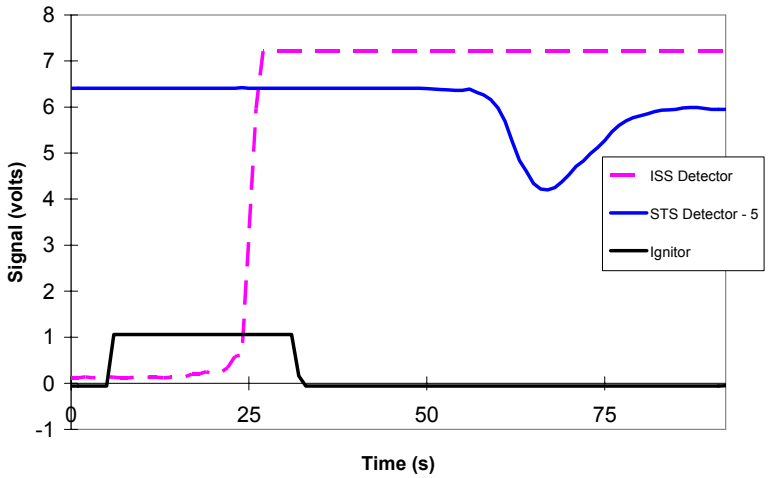

Figure 1-16. CSD results from paper test 15

Traces of smoke detector signals as a function of time for a paper test 15. The STS detector shows increasing downward deflection with increased smoke level, the ISS detector deflects upward. The onset of signal for the STS detector correlated with ignition of the paper.

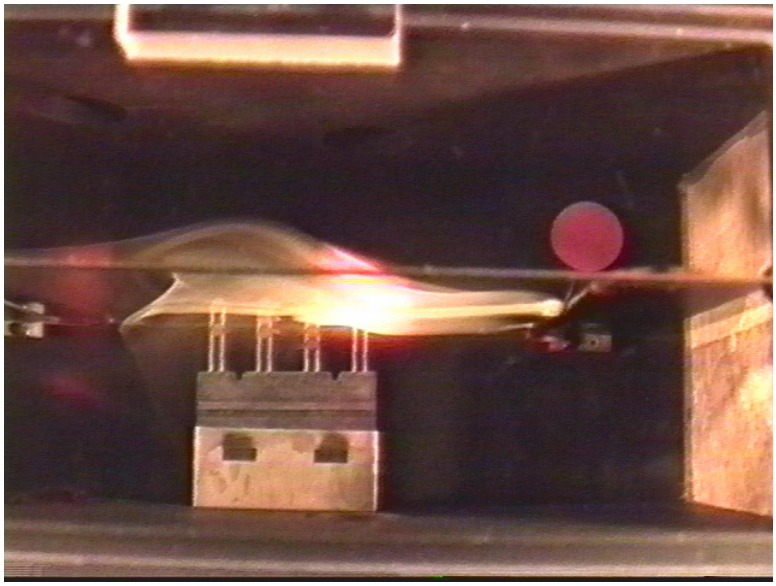

Figure 1-17. Image of smoke production during paper test 15

Image taken during the period when the paper ignited. Air flow is from right to left. The thermophoretic sampler probe is in the deployed position in the middle of the image. The red and white glow from the smoke is light scattered from a laser.

Figure 1-18 contains TEM images of typical particulate from Teflon, Kapton and Candle tests. The three images are at the same magnification and show the significant variation in the particulate morphology for the three materials. The Teflon and Kapton particulate are recondensed polymer material while the candle particulate is typical of hydrocarbon soot. Table 1-2 summarizes the results for the tests for which comparable particulate samples were collected for 1-g and low-g. Significantly, despite strong smoke levels visible in the video record, no particulate material was found on the TEM grids for overheated paper and silicone rubber tests. The suspected cause of this is that the particulate for these materials is actually liquid droplets which later evaporated or spread out on the grids' surface, rendering them undetectable by the TEM.

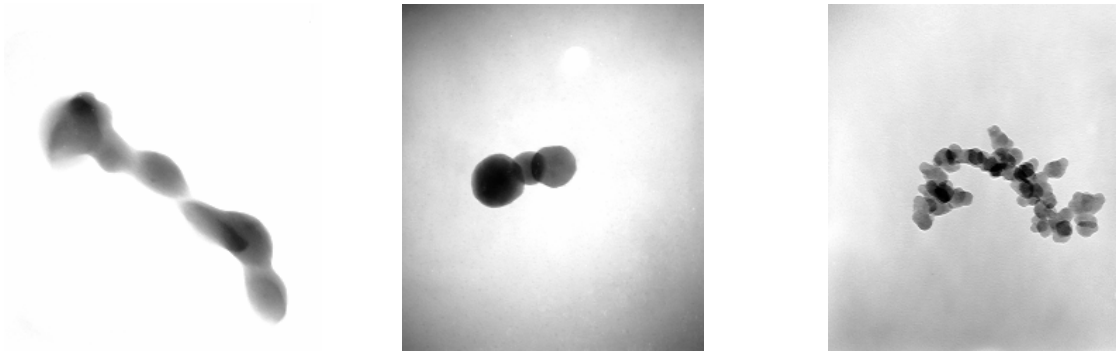

Figure 1-18. Transmission Electron Microscope Images of smoke particles from Teflon, Kapton and Candle tests.

Images are at the same magnification, candle soot primary particles are approximately 20 nm.

Table 1-2: Properties of smoke particulate generated in reduced gravity and in normal gravity

Material	Low-g Primary Diameter (nm) geometric mean	1-g Primary Diameter (nm) geometric mean	Low-g Aggregate Length (nm) geometric mean	1-g Aggregate Length (nm) geometric mean
Kapton	76	35	223	35
Candle	34	17	976	265
Teflon	136	75	662	277

1.3 Current status of understanding and key issues where knowledge is still lacking

As described in the background section above, the CSD experiment saw a significant difference in smoke detector response for 1-g tests versus μg tests. The most noticeable differences were enhanced performance of the ISS detector for Kapton™ smoke in low-gravity and decreased performance for the STS detector for paper and silicone rubber (liquid aerosol) smoke in low-gravity. The particulate data for the Kapton™ smoke indicate a substantial increase in the primary and aggregate dimensions for the Kapton smoke in low-gravity. This result is consistent with the increased signal seen on that detector. The difference in performance for the STS detector in low-gravity is suspected to be a result of increased droplet sizes for the liquid aerosol producing materials. Unfortunately, the thermophoretic sampling technique used in CSD was not able to produce droplet size information for these liquid-smoke-producing materials due to the long stowage interval before the samples could be examined in a microscope. Consequently, the reason for the poor performance of the STS detector for liquid smokes has not been determined with certainty. It is proposed, however that the change in signal seen in the CSD experiment was due to droplet size growth in the extended high droplet concentration region seen in low gravity.

Although other fire detection strategies (e.g. thermal, species or radiation) are continuously being evaluated for use in spacecraft, due to the nearly universal tendency of combusting or pyrolyzing systems to produce particulate, it is nearly certain that smoke particulate detection will continue to be a favored method of spacecraft fire detection. Despite its demonstrated effectiveness, smoke detection is not fully developed for spacecraft applications. To date, the only data on spacecraft smoke size distribution are the results provided by CSD. Early spacecraft fire detection will be increasingly important on long duration missions in large spacecraft where unattended equipment will be powered for long times. The current state of knowledge is insufficient to truly assure that existing space craft smoke detection systems provide the needed sensitivity. Rational smoke detector implementation requires better smoke particulate size distribution information from materials typical of spacecraft. Since many of the fire threats on spacecraft involve materials that produce liquid smokes in the incipient ignition phase, it is critical that the droplet growth be better understood. The value of this research is that it will directly improve crew safety and mission assurance by providing data necessary to ensure reliable detection of incipient spacecraft fires, ensuring the safety of future crews and missions.

Based upon this rationale, the motivation of this program can be summarized as three hypotheses:

In a μg environment, with the absence of the strong buoyancy-induced flows, smoke particle growth from a pyrolyzing/smoldering source, as a result of nucleation, condensation, and coagulation, will lead to larger particles compared to those produced in 1g. The formation of the larger particles is favored by the expected higher vapor concentration and smoke residence times near the source due to the reduced velocities and mixing at μg conditions. In particular, it is hypothesized that liquid aerosol smokes produced in microgravity will exhibit substantially larger droplet sizes than under the same conditions in normal gravity (with a corresponding decrease in the particle number density for the same mass of smoke). The change in the size distribution and number density will, in turn, affect the response of the smoke detectors and possibly result in some detectors not producing an alarm when exposed to this smoke.

The large smoke particles produced at μg will increase the difficulty of detecting this smoke because of the need to prevent other suspended particulate from entering the detector. In particular, detectors with built-in particle size separators (e.g. the STS detectors) may exhibit changes in their performance. Differentiation between dust and smoke particulate will require accurate smoke particulate size information.

Even with ventilation flow through a space vehicle at μg conditions, there will be regions of the vehicle where generated smoke would require long periods (tens of minutes) of time to enter existing non-aspirated smoke detectors. It is hypothesized that the aerosol size distribution will continue to change as a result of particle coagulation, albeit at a slower rate as the smoke is transported to the detector.

2 Flight experiment definition

2.1 Objectives of the flight investigation

The overall objective of the experiment is to improve the reliability of future spacecraft smoke detectors by making measurements of the smoke particulate size distribution to enable rational design of smoke detectors.

To achieve this, the detailed experiment objectives (in priority order) are:

1. Make measurements of three moments of the particle size distribution for the μg smoke from several materials found in spacecraft considering the effects of sample temperature, air flow, smoke residence time (near the source) and smoke aging. The primary targets are materials that produce liquid smoke particulate but solid smoke producers will also be considered.

2. Make measurements of the effect of μg and 1-g on the size distribution of liquid aerosol smokes (using an idealized smoke e.g. DBP) to provide data for numerical model comparison.

3. Evaluate the performance in μg of the two existing U.S. spacecraft smoke detector designs for the test conditions.

4. Evaluate other smoke detection/sensing devices (e.g. CO and CO_2 species sensors and E-Nose) at NASA's request for the test materials.

2.2 Experimental approach of the flight investigation

The planned approach for the experiment is to build upon the design heritage from the CSD experiment by adding new diagnostic techniques to allow improved in-flight characterization of the smoke particulate. The experiment will utilize the MSG facility for power, data acquisition and containment. Using resistive heating, a variety of materials will be overheated, producing smokes of differing particle characteristics. These smokes will be produced under different heating and flow conditions and will be allowed different aging durations. Although complete measurements of the particle size distribution would be desirable, this requires either extensive up and down mass or instruments that are too large to be implemented in a space experiment. The alternative is to make integrated measurements (moments) of the particle size distributions and concentrations using simpler particulate diagnostics systems and spacecraft smoke detectors. As will be described in detail in section 7.1, the measurements will be processed to provide distribution statistics including the particle arithmetic mean diameter, the diameter of average mass and, using the assumption of a log-normal distribution, the geometric mean diameter and geometric standard deviation. Due to these simplifications, this approach has its limitations (e.g. it cannot readily recognize a bimodal distribution) nevertheless, it will provide data that will be critically useful in defining smoke detection systems that can discriminate against the background dust levels.

This approach has been demonstrated successfully by Cleary, Weinert, and Mulholland (2003) who applied the moment method described in section 7 to a series of aerosol smokes (Cotton Wick, Polyurethane Foam, Wood, Corn Oil, and Toast). The cumulative size distributions from the impactor results for the smoke aerosols are shown in figure 2-1. The aerosol measurements included the: ionization moment, number concentration, mass concentration, and the aerodynamic diameter

distribution from a cascade impactor. These results were processed using the properties of a log-normal distribution consistent with the approach described in section 7. The resulting Mass Median Aerodynamic Diameter (MMAD) and standard deviations are compared to the values obtained directly from an impactor in table 2-1. Overall the moment results are consistent with the direct impactor data, providing support for the use of the moment approach for characterizing smoke aerosols.

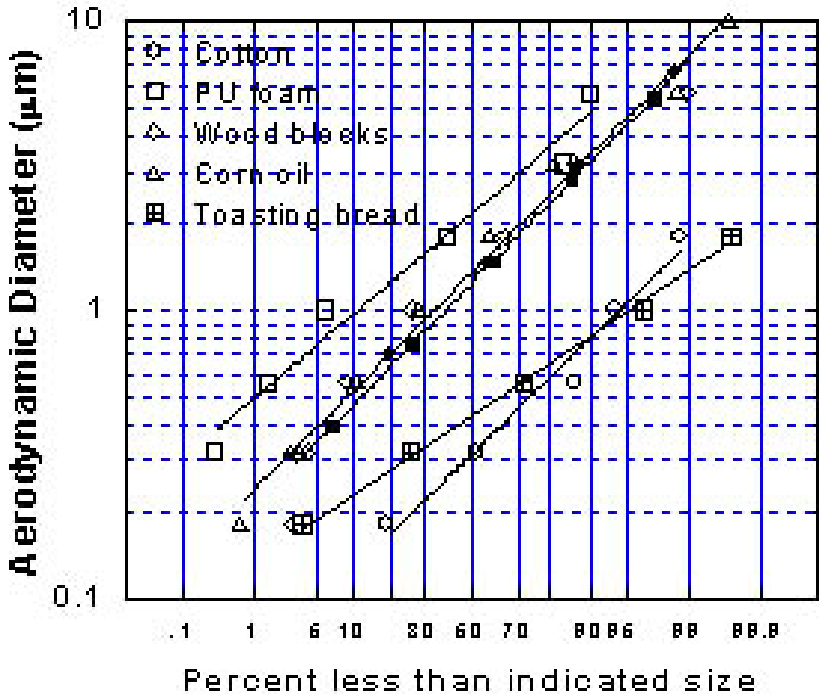

Figure 2-1. Cascade impactor results for the test smokes.

Table 2-1: Properties of smoke particulate comparing calculated values with values from the cascade impactor

Smoke	Mean D_{30} (mm)	Mean σ_g	Predicted MMAD (mm)	Impactor MMAD (mm)	Impactor σ_g
Cotton Wick	0.24	1.4	0.28	0.31	1.7
PU foam	1.0	1.6	1.4	2.0	1.6
Wood	0.53	2.25	1.4	1.5	1.9
Corn Oil	0.50	2.5	1.8	1.6	2.2

Toast	0.32	invalid	invalid	0.43	1.6

The new Microgravity Science Glovebox (MSG) planned for ISS is substantially different from the predecessor facility used by CSD: the Microgravity Glovebox (MGBX) flown in SpaceLab and the Shuttle mid-deck. Consequently substantial repackaging will be required to implement the experiment in the MSG even though the changes primarily consist of the addition of commercial-off-the-shelf (COTS) aerosol measurement systems. A schematic of the experiment is shown in figure 2-2. The design is based upon the increased size of the MSG and also the limitations imposed upon the design by the size of the MSG openings. As shown in the schematic, the hardware concept consists of several interconnected modules. Smoke will be generated in the smoke generation duct with flow induced by the aging chamber. Once the smoke generation is complete, the smoke can either be held in the aging chamber for a desired interval or immediately expelled to the diagnostics duct. The diagnostics duct contains the interface to the various moment measurement devices and the smoke detectors. After passing through the diagnostics duct, the smoke will be filtered and exhausted.

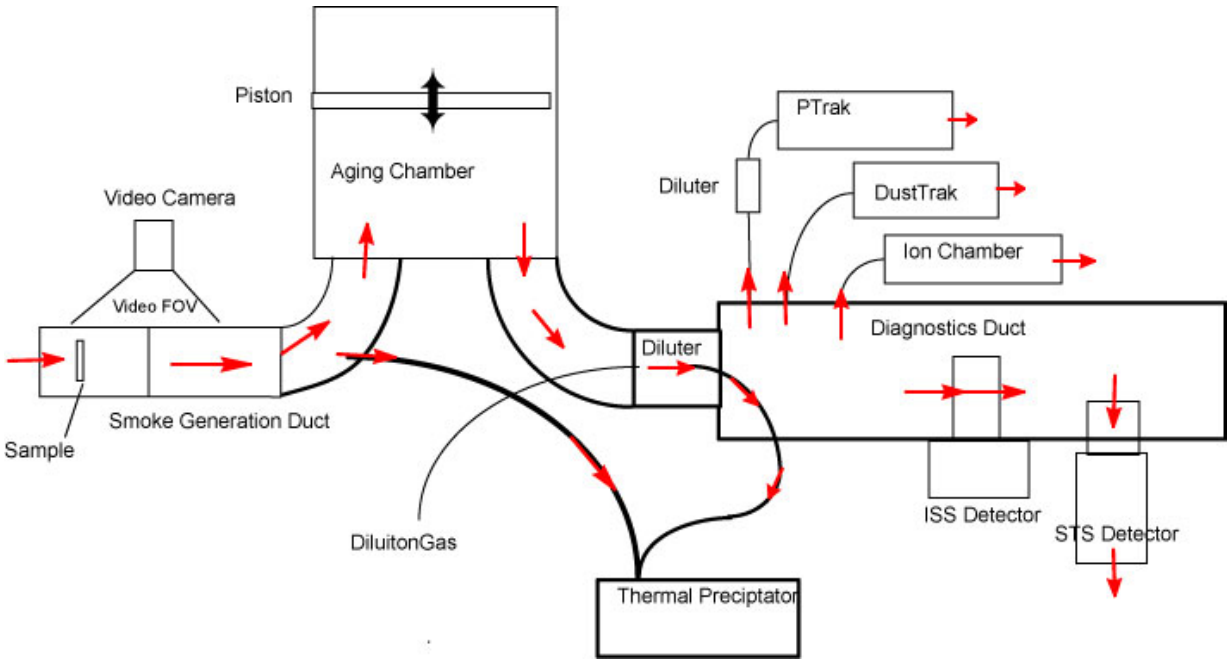

Figure 2-2. Schematic of the planned experiment implementation

The smoke is generated by heating the sample and travels down the Smoke Generation Duct to the Aging Chamber drawn by the piston motion. The piston then pushes the smoke into the diagnostics duct where it is extracted by the various diagnostic instruments.

2.3 Science data end products

To achieve the aforementioned objectives, the following data products must be obtained. (See section 7.1 for explanation of the determination of these values)

For each material as a function of mass loss/unit area, air flow rate, and smoke aging determine:

Arithmetic mean diameter, (objectives 1 & 2)

Diameter of average mass, (objectives 1 & 2)

Geometric mean diameter, (objectives 1 & 2)

Geometric standard deviation, (objectives 1 & 2)

Spacecraft smoke detector signals normalized by number density, (objective 3)

Transmission Electron Microscope (TEM) images of particulate morphology (objective 1)

Signals from other smoke sensing devices (objective 4).

2.4 Anticipated knowledge to be gained, value, and application

Upon completion of the data analysis, NASA will have a measurement of the average size and standard deviation of the smoke particulate from several materials that are representative of materials used on spacecraft. This will provide data critically needed for design of future smoke detectors, determination of the alarm setpoints and reduction of false alarms. The associated smoke growth modeling will support extension of these results to additional geometries. If the desired diagnostics are provided, they will support understanding of the performance of NASA's current smoke detectors and alternate strategies for fire detection.

3 Experiment requirements

The following section presents the requirements and the rationale/justification for the requirements. The requirements are presented in table 1 with supporting text and justification in corresponding sections.

Table 3-1: Summary of science requirements

Experiment configuration

1. **Smoke generation duct**
   a) Configuration: Square or round duct with air flow through the duct.
   b) Optical access: One view is required of the sample and the downstream flow. This view should be illuminated and imaged by a color video camera (visible light only). The orientation of the light relative to the imager should permit the visualization of the light scattered by the smoke.
   c) Length: The straight section of the duct downstream of the sample shall be at least 30 cm long and shall be known within 1 cm.
   d) Width: The test section width shall be based upon the sample size (see sample size below). The smallest duct dimension shall be at least twice the largest sample dimension.
   e) Flow rate: 1 to 10 (+/- 0.5) cm/s average flow velocity.
   f) Transverse spatial flow variation: Induced maximum flow velocity (no sample present) shall be at the center of the duct with monotonic decrease to the walls. The ratio of the centerline flow velocity to the average velocity shall be no greater than fully developed laminar flow +10%.
   g) Flow profiles well characterized (cold flow, no sample present) in ground based testing (hot wire anemometry adequate, test plan to be approved by the project scientist).
   h) Temporal flow variation: Less than +/- 10% variation of average velocity (measured with 1 Hz resolution).
   i) Flow linearity: for cold flow without the sample present, flow stream lines (from the centerline to ¾ of the distance to the wall) shall be linear (distance from wall shall not change more than 10% throughout the test section). Can be validated by smoke tracers (1-g).
   j) Sample location: Sample shall be located so its long dimension is oriented perpendicular to the flow and the sample shall be greater than 5 (10 preferred) times its small dimension from the duct entrance. Samples shall be centered on the duct axis +/- 2mm.
   k) Fan or flow generator: Either end of the duct is acceptable, duct outlet preferred.
   l) Surface coating: Where feasible, objects in the camera field of view should be blackened and roughened to reduce stray reflections. Acceptance will be based on testing with a flight-like unit. With the illumination on, it should be possible to discriminate punk smoke from the wall reflections.
   m) Particle loss by impaction, diffusion, thermophoresis or electrostatic attraction shall be minimized and characterized by test and / or analysis in 1-g. (< 5% desired).

2. **Diagnostics duct (includes all ducting from the aging chamber to the diagnostics)**
   a) Unswept volume minimized (< 5% desired).
   b) Transit time minimized (< 60 s desired) and unaffected by changes in the flow rate in the smoke generation duct
   c) Smoke leaving the aging chamber shall be reliably sampled (< 10% error for each size range) by the diagnostics for the expected particle size ranges (0.02 to 1 μm, 1 to 2.5 μm, 2.5 to 6 μm) with total particle sampling error minimized and characterized by 1-g testing or analysis.
   d) Temporal delay from the smoke source shall be well characterized. Required accuracy of temporal delay calibration: +/- 5 seconds in residence time for all duct flow rates. (Temporal delay includes transit time from the aging chamber to the diagnostics sampling point, transit time in the sampling tube and instrument response time)

Table 3-1: (continued)

Summary of science requirements

e) Volume sufficient to house the inlets to the diagnostics
f) Particle loss by impaction, diffusion, thermophoresis or electrostatic attraction shall be minimized and characterized by test and / or analysis in 1-g. (< 5% desired).
g) Dilution air can be added as long as the smoke concentration is maintained in the operating range of the diagnostics. If dilution is used, either the dilution level must be known +/-10% or the concentration entering the aging chamber must be known.
h) The concentration seen by each of the diagnostics must be the same or at a known dilution level (consistent with achieving the required instrument accuracy).

3. Ambient air quality

a) Particle number concentration less than 10,000 particles /cm^3 (lower desired) as determined by the number concentration system (below). Any dilution air shall be < 50 particles/cc (lower desired).
b) Particle mass concentration less than 30 $\mu g/m^3$ as determined by the mass concentration system (below).
c) Humidity between 20 % and 80 %.
d) Temperature between 20 ^oC and 30 ^oC

4. Smoke aging chamber

a) Residence time controllable from 2 to 100 minutes
b) Displaceable volume sufficient to provide enough sample gas to the diagnostics (including the thermal precipitator) to achieve a steady signal on all the diagnostic systems (based on the sample size and temporal resolution requirements of the diagnostics).
c) Chamber design produces conditions where the rate of change of the number concentration resulting from wall loss is less than 10% of the rate of change of the particle concentration from coagulation (in normal gravity for 1 µm particles). Suggested approaches: minimize surface to volume, fabricate wall materials with conductive materials to reduce electrostatic attraction.
d) The ability to store enough gas for multiple aging durations is strongly desired.
e) The smoke in the aging chamber must be fully mixed within 10% of the residence time.

5. Sample heater

a) Size: sample size and heater design will be established to achieve the required mass loss rate by controlling the sample surface temperature and geometry.
b) Heating rate: achieve target wire temperature (within required accuracy) in 5 seconds.
c) Temperature range, current estimate: 50-500 C. Actual values to be determined based upon the sample mass loss rate.
d) Temperature accuracy: reproducibility and accuracy of the temperature shall be such that the mass loss repeatability (item f below) is achieved.
e) Heater design shall provide active temperature control to adapt to low-gravity environment.
f) Sample mass loss rate: Without igniting the samples, the samples shall produce sufficient mass, at the specified rate (see test matrix) to fill the aging chamber with the target mass concentration. This shall be demonstrated by ground based testing with the 95% confidence interval within +/- 50% of the target mass loss rate. The target concentration in the aging chamber shall be selected so that it is in the operating range of the diagnostic systems.

Table 3-1: (continued)

Summary of science requirements

6. Experimental operating conditions/test samples

a) Spacecraft material samples (Teflon™ wire insulation material, Kapton™, silicone rubber, cellulose).
b) Samples shall be small pieces of these materials selected to be representative of materials used in spacecraft. Sample geometry is unimportant other than through its interaction with the sample heater (based on testing in 1-g).
c) Reference sample design: Porous wick material supporting dibutyl phthalate (DBP). This liquid shall be vaporized by the sample heater producing an aerosol with predictable thermo physical properties.
d) Mass loss for all samples to be established by determining the mass change in the sample. Accuracy: 0.0001 g. This will require reasonably expeditious sample return.
e) Number of tests, 4 per sample required with an additional 4 tests strongly desired for repeats and parameter variation. (see test matrix below).

7. Microgravity requirements

a) Less than 10^{-3} g at frequencies less than 30 Hz during sample heating interval, less than 10^{-2} g at frequencies less than 30 Hz during smoke aging and diagnostics operation.

Experimental monitoring measurements

8. Video Monitoring:

a) 1 view required (2nd orthogonal view desired) of the test section during the smoke generation interval.
b) 30 Hz recording
c) Standard composite color video (equivalent 3 color at 8 bits/color or better), able to image light scattered from smoke, compression acceptable with testing.
d) Field of view at duct midplane:
Transverse: largest sample width plus 20%
Axial: starting at upstream side of sample projecting 3 cm downstream required, more desired
e) Resolution: 0.5 mm
f) Depth of field: depth of smoke plume.

9. Sample temperature measurements:

a) Sampling Rate: 1 Hz
b) Accuracy and Precision: +/- 5 % of reading (Celsius temperature).
c) Location: Provide a temperature representative of the reacting region of the sample near the heater during sample heating.

10. Gas plume temperature measurements:

a) Sampling Rate: 1 Hz
b) Accuracy: +/- 5 % of reading
c) Location: In the center of the duct 1 to 3 cm from the sample
d) Probe wire diameter: as small as possible, less than 0.010” diameter

11. Air flow speed in the duct (average), ambient humidity, pressure and temperature measurements:

a) 0.1 Hz sampling rate
b) Accuracy +/- 10% of reading
c) Location: representative of the duct inlet conditions
d) Range: Air flow 1-15 cm/s, humidity 10 to 90% RH, pressure 0.08 to 0.13 mPa, temperature 15 to 35 C.

Table 3-1: (continued)

Summary of science requirements

Experimental diagnostics measurements

12. Number concentration measurement system (zeroth moment)

a) Location: in diagnostics duct
b) Expected levels at detector location: (10^4 to 3×10^7) part./cm^3 (actual values will be based upon the suite of instruments, calibrated dilution is acceptable)
c) Repeatability: $\pm$ 4 %, accuracy $\pm$ 10%
d) Temporal resolution: 5 s
e) Sampling rate 0.2 Hz
f) Particle size sensitivity: 0.05 µm to 1 µm
g) System calibrated on the ground for monodisperse aerosols over expected range.
h) Suggested approach: TSI PTrak™, dilution will be required for smaller particles due to increased number count.

13. First moment measurement system

a) Location: in diagnostics duct
b) Expected levels at detector location: (0.01 to 7.5) m/cm^3 (actual values will be based upon the suite of instruments, calibrated dilution is acceptable)
c) Repeatability $\pm$ 4 %, accuracy $\pm$ 10 %
d) Temporal resolution 5 s
e) Sampling rate 0.2 Hz
f) Particle size sensitivity 0.05 µm to 4 µm
g) System calibrated on the ground for monodisperse aerosols over expected range.
h) Produce measurement that can be correlated with the first moment. Suggested approach: ionization sensor from residential smoke detector

14. Mass concentration measurement system (third moment)

a) Location: in diagnostics duct (inlet to aging chamber desired)
b) Expected levels at detector location: 0.1 mg/m3 to 400 mg/m^3 (actual values will be based upon the suite of instruments, calibrated dilution is acceptable)
c) Repeatability: $\pm$ 4 %, accuracy $\pm$ 10 %
d) Temporal resolution: 5 s
e) Sampling rate: 0.2 Hz
f) Particle size sensitivity: 0.05 µm to 4 µm
g) System calibrated on the ground for monodisperse aerosols over expected range.
h) Produce measurement that can be correlated with the third moment (mass concentration). Suggested approach: TSI DustTrak™
i) Measurement of this moment at more than one particle size cutoff (e.g. using impactors at the inlets of multiple Dust Traks™) is desired.

15. Thermal precipitator

a) Collect samples of smoke particles on Transmission Electron Microscope (TEM) grids
b) Sampled locations, required location: 5 to 20 cm from sample; desired location: at exit from aging chamber.
c) If sample is aspirated from the duct, sample lines must cause limited particle loss due to diffusion or impaction. Sample line transit time must be characterized (+/- 5 s).
d) At grid location, flow must be 1 cm/s (+/- 20%) with a thermal gradient of 200 (+/- 40) °C/mm above the grid.
e) TEM grid attachment: grids must be removable without damage or dislodging particles as demonstrated by ground-based testing.

Table 3-1: (continued)

Summary of science requirements

f) Handling consideration: Grids must be protected from contamination before and after the tests.
g) Grids must be returned for TEM analysis
h) Grid type: 3 mm copper TEM grid, Formvar/Carbon coated 300 mesh.
i) System performance (sampling efficiency and particle loss) must be demonstrated by 1-g testing (less than 20% variation in number count loss between 0.5, 1 and 2 μm test aerosols, in precipitator).

16. Spacecraft smoke detectors: (desired)
a) Location: in diagnostics duct
b) Sampling Rate: 5 Hz.
c) Shuttle system (ionization): Brunswick Defense™ Engineering Model (supplied by PI)
ISS system (scattering): Allied Signal/Honeywell™ Engineering Model (supplied by PI)

17. Gaseous Constituent Sensors: (desired)
a) Location: in diagnostics duct
b) Sampling Rate: 5 Hz.
Suggested system: CO and CO_2 sensors such as provided by Makel Engineering
Alternate suggested system: E-nose, developed by JPL

The following section provides supporting text and justification for the requirements in table 3-1. In all cases, the requirement as stated in table 3-1 supercedes any discussion here.

3.1 Experiment configuration

3.1.1 Smoke generation duct

The selected configuration for study was an overheated component exposed to cabin ventilation flows. This is expected to be a practical scenario which will show the effects of μg. Higher flow rate cases will reduce the residence time near the sample and will show less change in the particle size. While it would be preferable to have a constant air velocity across the sample, our experience has found that the flow duct geometry need not be overly specified. The duct width must be sufficiently wide that the sample is not unduly affected by the walls and the smoke plume can convect down the center of the duct without substantial losses due to impaction, electrostatics, or diffusion and so it is similar to an unconfined flow. To allow successful modeling, the flow must be predictable and laminar and not have gradients substantially stronger than those seen in fully developed flow. Testing conducted with cold flow will establish the incoming flow profile and the modeling of the reference sample can account for the variation across the sample.

To develop a framework for interpreting the flight data and to guide selection of the duct length requirement, a model and experiment approach was undertaken. The numerical approach is discussed in appendix A and the experimental work is discussed in appendix B. Although the model predicts substantially faster condensation rates compared to the experimental results, both methods indicate that the required duct length is adequate (and not excessive) to achieve the bulk of the condensation of vaporized product. The flow velocity is based upon typical ventilation flows that can be expected in spacecraft.

3.1.2 Diagnostics duct and locations of the diagnostics systems

The primary requirement for the diagnostics duct which houses the inlets to the smoke diagnostics is that sampling by the instruments be as representative as possible and cross contamination between tests be minimized. This can be best achieved by minimizing the unswept volume and limiting the

variation in the flow time to each instrument. The criteria selected for the residence time is expected to be small compared to the aging chamber times and will also be small compared to the transit times for smoke in a space craft.

Since the air velocity in the smoke generation duct or out of the aging chamber will be varied as part of the experimental testing, an imbalance may exist between the flow rates in the diagnostic duct and the smoke generation duct. To prevent this from causing a flow disturbance in the smoke generation duct, it is permissible for the transition between the two ducts to either release excess air from the smoke generation duct or add filtered air.

3.1.3 Ambient air quality

To avoid undue experimental noise and cross contamination between tests, it is important that the ambient particulate conditions be well below the anticipated test conditions. Temperature and humidity must be in the normal, non-condensing range to avoid interference with the particle growth phenomena.

3.1.4 Smoke aging chamber

To allow study of the smoke aging it is necessary that, for some tests, the smoke be allowed to sit in a quiescent environment before it is analyzed by the diagnostics. The chamber could be charged with smoke and after the designated waiting period, the smoke would be sampled. To avoid electrostatic attraction of the particulate, a conductive material is suggested. The design of the aging chamber must consider the competition between particle loss to the walls and particle coagulation. Considering Smoluchowski coagulation for a uniform particle distribution, (Hinds, 1999) the change in the number concentration can be expressed as:

$$\frac{dN}{dt} = -K_0 N^2 \tag{1}$$

This has the solution:

$$N(t) = \frac{N_0}{1 + N_0 K_0 t} \tag{2}$$

Wall losses can be estimated assuming a spherical vessel and particle diffusion. Table 3-2 provides a comparison of the wall loses versus coagulation losses for a range of particle sizes for a 100 mm radius chamber.

The wall loss is modeled as a one-dimensional transient particle diffusion process in spherical coordinates. The formulation of the problem is as follows:

$$\begin{aligned} &\frac{D}{r^2}\frac{\partial}{\partial r}\left(r^2 \frac{\partial C}{\partial r}\right) = \frac{\partial C}{\partial t} \\ &C = C_0 \qquad \text{at} \quad t = 0; \\ &\frac{\partial \mathrm{C}}{\partial \mathrm{r}} = 0 \qquad \text{at} \quad r = 0; \\ &C = 0 \qquad \text{at} \quad r = r_w \end{aligned} \tag{3}$$

where C is the particle number concentration and r_w is the radius of the chamber wall. Note that in the formulation the particle concentration at the wall is assumed to be zero all the time. By solving this problem analytically for the function of $C(r, t)$, we can calculate the average concentration in the chamber as function of time. The solution, in a non-dimensional form, is

$$\frac{C_{avg}(t)}{C_0} = \frac{6}{\pi^2}\sum_{n=1}^{\infty}\frac{e^{-n^2\pi^2\tau}}{n^2} \qquad (4)$$

where $C_{avg}(t)$ and C_0 are the average concentration at t and the initial concentration, respectively. The dimensionless time, τ, is defined such that $\tau = D*t/r_w^2$. The particle diffusion coefficient, D and the coagulation constants are based on formulations from Hinds, 1999.

The diffusion estimate assumes a quiescent chamber. Initially there will be some residual motion from the smoke injection which will decay significantly but not completely over the time scales considered here. However, even in the initial times when the concentrations near the wall are higher, the wall loss is substantially less than the coagulation so increasing the mixing level is unlikely to substantially change the result.

Table 3-2: Estimated particle concentrations in aging chamber

Particle Size	Initial Concentration (C_0)	Time	Particle Diffusivity (D)	Coagulation constant (K_0)	$C(t)/C_0$ due to coagula-tion	$C(t)/C_0$ due to wall loss	$C(t)/C_0$ due to both mechanisms
µm	particles/ cc	s	mm^2/s	mm^3/s			
0.1	$1x10^6$	60	7.2×10^{-4}	8.5×10^{-7}	0.952	0.993	0.945
0.1	$1x10^6$	600	7.2×10^{-4}	8.5×10^{-7}	0.662	0.978	0.648
0.1	$1x10^6$	1800	7.2×10^{-4}	8.5×10^{-7}	0.395	0.962	0.380
1.0	$1x10^6$	60	2.6×10^{-5}	3.3×10^{-7}	0.981	0.999	0.937
1.0	$1x10^6$	600	2.6×10^{-5}	3.3×10^{-7}	0.835	0.996	0.832
1.0	$1x10^6$	1800	2.6×10^{-5}	3.3×10^{-7}	0.628	0.992	0.624
1.0	$1x10^7$	60	2.6×10^{-5}	3.3×10^{-7}	0.835	0.999	0.834
1.0	$1x10^7$	600	2.6×10^{-5}	3.3×10^{-7}	0.336	0.996	0.335
1.0	$1x10^7$	1800	2.6×10^{-5}	3.3×10^{-7}	0.145	0.993	0.144

3.1.5 Sample heater

The samples need to be supported in low gravity while they are heated to their pyrolysis or evaporation temperatures. A simple heater wire wrapped around the samples was found to be very effective for CSD consequently the requirements are based upon this design. It was possible to obtain repeatable (in 1-g) weight loss rates distributed over a range of approximately a factor of 4. However, due to the loss of buoyant cooling of the heater wire, the weight loss in low-gravity cannot be predicted by controlling the heater power, instead, the wire temperature must be controlled; this can be accomplished by measuring the change in the wire resistance. This wire temperature provides a very good indication of the temperature of the reacting portion of the sample.

Other approaches were considered (e.g. radiant heating) however these were all found to pose greater difficulties for controlling the sample temperature in low-gravity. This approach (direct contact with a hot surface) was shown to be effective in CSD and was based upon the heated filament

approach used in some thermogravimetric analysis and evolved gas analysis systems and is similar to other smoke detection test methods (Bukowski et al. 2003).

Two target mass loss rates are specified in the test matrix (Table 3-6) to evaluate the effect of temperature on the particle size distribution. The total mass delivered to the aging chamber will be determined by the operating ranges of the smoke diagnostics and the flow system design. It is acceptable to produce the target smoke concentration either at the sample or by later dilution of a more concentrated smoke stream.

3.2 Experimental operating conditions/test samples

3.2.1 Spacecraft material samples

The selection of test samples was motivated by the goal of identifying materials in common use in spacecraft that may be involved in fire detection scenarios. Furthermore, a variety of smoke morphologies were needed including smokes consisting of liquid and solid particulates. The two solid particulate smokes will be generated using Teflon and Kapton both of which are in the standard wire insulation materials for the ISS and the shuttle respectively and can be expected to be among the early smoke products. As seen in the CSD experiment [Urban, Griffin and Gard 1997 a & b)] these two materials produce significantly different smoke morphology. The two liquid smoke producers are cellulose (cotton lamp wick) and silicone rubber. Cellulose is ubiquitous on spacecraft (clothing, paper and toweling) and silicone rubber is widely used for flexible heaters, wire wrapping, gaskets and tubing. In the preignition, pyrolysis state, both of these materials produce smoke that is largely comprised of condensed liquid materials. In the CSD experiment, these two materials produced a smoke particulate that appeared to be substantially larger in low-gravity than in normal gravity.

3.2.2 Reference sample design

An additional reference source will be used to provide a smoke source that can be readily simulated numerically. To simulate the fuel configuration used for the other samples, a porous wick pre-saturated with a liquid material with appropriate thermophysical properties will be used. The suggested material, dibutylphthalate (DBP), is a pure liquid with well characterized saturation vapor pressure, surface tension, and diffusivity, and it has been widely used in the aerosol community for studying nucleation and condensation of heated vapor flowing into a cooled pipe [Nguyen et al., 1987, Wilck et al., 1997]. DBP has a sufficiently low vapor pressure (< 0.01 mm Hg @ 20°C) that the sample can be predeposited before the mission. The heater design can be similar to the other samples albeit operating at a substantially lower temperature.

3.3 Experimental monitoring measurements

3.3.1 Video

There is no substitute for quality video records of the event. Video recordings of the smoke evolution process are very important for establishing proper operation of the test apparatus and for debugging the system operation. Furthermore, the video provides a helpful and compelling demonstration to the user community of the variability of the smoke evolution. Experience with CSD showed dramatic cases where some clearly visible smoke streams were not always detectable by the smoke detectors while some invisible smoke streams were readily detected. Normal video resolution is acceptable if the smoke is illuminated by forward scattered light from an appropriate light source.

3.3.2 Sample temperatures and other operating parameters

Control and recording of the sample temperatures is required to enable reliable smoke generation at the desired concentrations and for characterizing the plume. Other operating parameters (pressure, fan speed, humidity etc) need to be recorded as part of normal experimental quality assurance.

3.4 Experimental diagnostics measurements

The derivation and physical meaning of the moments is described in detail in section 7.1. In simple terms, the zeroth moment can be thought of as the number concentration, the first moment is, in effect a diameter concentration, and the third moment is a mass concentration. Given the limitations imposed by space experiments, ideal measurements of moments of the particle distribution will not be possible.

Instead statistics of the particle size distribution must be assembled by use of the log-normal particle size distribution and integral measures (moments) of the size distribution. This approach has been shown to be acceptable over an appropriate range of particle sizes (Cleary et al. 2003). This moment analysis requires the assumption of a log-normal particle size distribution and has certain limitations imposed by the non-ideal nature of the instruments that are required by a space flight experiment, however, despite these limitations, these measurements will provide sufficient accuracy to enable design of improved fire detection systems. The relative impact of the accuracy of the diagnostic systems is discussed in appendix C.

At the time of this writing certain work remains in the validation of the diagnostics and the development of the final analysis protocol. These work items are enumerated below and will be addressed aggressively over the next few months.

1. Validation that the chosen instruments will adequately produce useful aerosol statistics via the moment method. This question is currently being addressed analytically with modeling of the light scattering device (DustTrak) to be followed by laboratory comparison of the moment method with impactor data for polydisperse smokes.
2. Completion of the analysis and calibration work needed to characterize the DustTrak response as a function of particle size. This calibration data will be used iteratively as described in section 7 with the moment method to determine the final size distribution statistics.
3. Extend our understanding of the ionization chamber to improve the correlation of the signal with the first moment.

3.5 Particle size Distribution

The central objectives of the SAME experiment relate to characterization of the particle size distribution of smoke from microgravity sources. In an earth based laboratory, this would typically involve use of instruments that would determine the shape of the particle size distribution in addition to the mean particle size e.g. mobility analyzers, classifiers or cascade impactors. Given the limitation of space experimentation, these approaches are not currently feasible. Instead, the approach proposed in the SAME experiment is to measure three moments (zeroth, first and third) of the smoke size distribution and derive specific measures of the size distribution specifically: the arithmetic mean diameter, the diameter of average mass and, using the features of the log-normal distributions, the geometric mean diameter and the geometric standard deviation. Two of these three moments can be measured using COTS (commercial off the shelf) devices and the third can be measured using the sensor from a residential smoke detector or another somewhat larger COTS device. While the discussion below provides a suggested approach, a custom system (or other COTS devices) that met the requirements would be fully acceptable. These devices all have different operating ranges and although the expected particle concentrations in the diagnostic duct are given in the requirements table, the actual values will depend upon the suite of instruments selected and their intersection of their sensitivities. The preflight calibration of these instruments and analysis of the error propagation from the original measurements to the end product statistics (geometric mean diameter and geometric standard deviation) are discussed in appendix C.

All three systems were tested using a monodisperse particle generation system as described by (Mulholland and Liu 1980). The generation system is shown in figure 3-1. The system operated by creating a polydisperse spray of diluted di-octyl phthalate (DOP), evaporating the spray, and then recondensing the DOP vapor into a monodisperse aerosol. The details of the process are discussed in the original paper (Mulholland and Liu 1980) but the number of condensation nuclei was determined by the constant spray number density and the droplet size was determined by the DOP concentration as the droplets grew to uniform size. The system functioned well over 0.05 to 1.3 μm droplet sizes and number concentrations from 2×10^3 to 2×10^6 particles / cm^3.

Figure 3-1. Photo of the monodisperse aerosol generator.

Poly -disperse spray generator is in the center and condensing and drying tubes are to the left.

3.5.1 Number concentration system

The proposed approach for determining the particle number concentration is using a condensation nucleus counter (PTrak™ ultra-fine particle counter from TSI™). (Figures 3-2 a and b) Particles are drawn through a saturator tube where the gas is saturated with isopropyl alcohol vapor. They then flow to a condensing tube where each particle acts as a nucleus and alcohol vapor condenses on them and they grow to a nearly uniform size. The flow passes through a nozzle which directs the particles into the measurement volume of a laser light scattering counter. In low gravity, the alcohol liquid will be contained in a wick just as it is in a one-g environment; however return to the wick of alcohol that condenses on the walls will require some modification since the current design depends upon gravity. Continuous operation for up to 8 hours is expected from one saturated wick. The concentration range is 0 to 5×10^5 particles/ cm^3 and the particle size range is 0.02 μm to greater than 1 μm. The upper size limitation is not a strong restriction because in the typical log-normal distribution, the largest particles contribute substantially to the mass concentration but not to the number concentration. The number concentration of the pyrolysis smoke can be as large as 5×10^6 so that dilution may be required to reduce the concentration within the linear limits of the instrument. We have experience with using a variety of diluters. For this application where a dilution factor of at least 10 is required, one option is a design based on the aspiration of a small flow of smoke into a flow of particle free air.

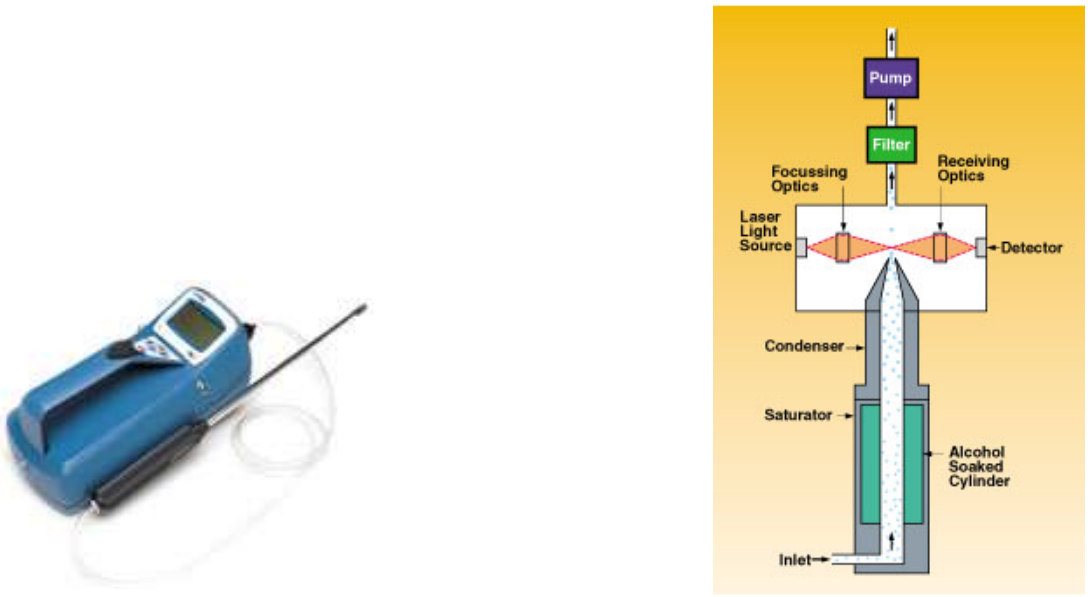

Figure 3-2. External view (a) and schematic (b) of TSI PTrak™ (TSI 2003).

Testing with the TSI PTrak™ using a monodisperse particulate source (Mulholland and Liu 1980) using an Electric Low-Pressure Impactor (ELPI™) for comparison showed excellent correlation over mass median diameters ranging from 0.06 to1.34 µm. (Figure 3-3) Despite the excellent correlation, the ELPI reading is generally twice that of the PTrak, potentially due to charging efficiency effects in the ELPI, the exact cause of the response difference is under study but is suspected to be a calibration issue. Prior to flight the instrument will be calibrated for the range of possible particle sizes to allow transformation of the signal to perform the moment analysis

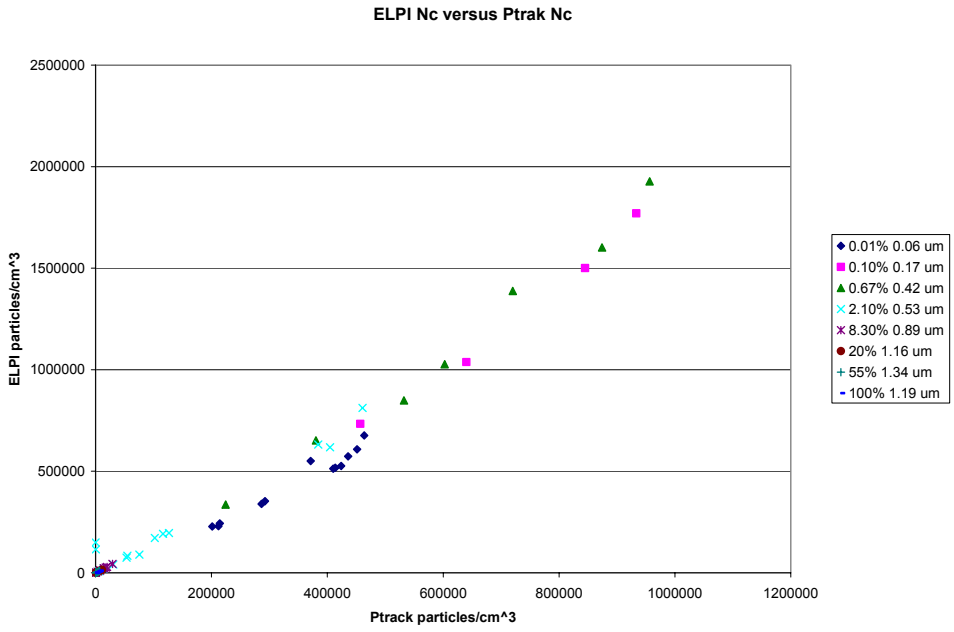

Figure 3-3. Comparison of the output of the PTrak™ with an Electrical Low-Pressure Impactor (ELPI™)

Aerosol particles were prepared using Dioctyl phthalate (DOP) solutions whose concentrations and resulting mass median diameters (μm) are indicated in the legend.

3.5.2 First moment system

The first moment is most conveniently measured using an ionization chamber. The proposed approach uses a chamber from a residential detector with the flow directed into the ion chamber via a tube, thereby overcoming the entry resistance. The major difficulty with the detectors is the high detection threshold, roughly 10^6 particles/cc. The figure (3-4) shows the correlation of the detector output with the first moment calculated using the ELPI™. Overall, the correlation is fairly good given the range of particle size, however the signal variation is less than optimal suggesting that there is some risk of achieving adequate signal or resolution from the device. Prior to flight the instrument will be calibrated for the range of possible particle sizes to allow transformation of the signal to perform the moment analysis. An alternative instrument that provides increased sensitivity with the cost of increased weight is a combination of an electrometer and a corona charger known as an EAD (Electrical Aerosol Detector).

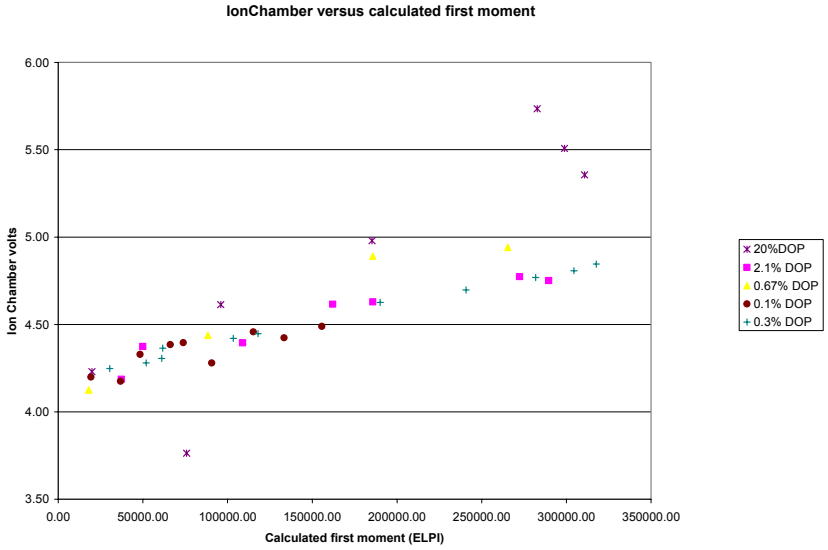

Figure 3-4. Comparison of the output of the Ion Chamber signal with the first moment calculated from the ELPI ™ data
Aerosol particles were prepared using Dioctyl phthalate (DOP) solutions whose concentrations and resulting mass median diameters (μm) are indicated in the legend. Units of the calculated first moment are micrometers/cm^3.

3.5.3 Mass concentration system

The suggested approach for measurement of the mass concentration is a light scattering instrument, which measures the light scattered by the particles at 90^o (TSI DustTrak™ aerosol monitor) shown in figure 3-5. The photometer signal intensity is correlated with the aerosol mass concentration given the particle density and optical properties. The output is approximately proportional to the mass concentration, but given the variation of scattering intensity with particle size, calibration with aerosols of known properties is required. The operating range of the instrument is 0.001 to 100 mg/m^3. The manufacturer provides impactors for the inlet which will provide different cut sizes. Use of a second TSI DustTrak™ with an impactor in place would provide very useful information on the particle size distribution particularly in the case of weak signals from the ionization chamber used for the first moment.

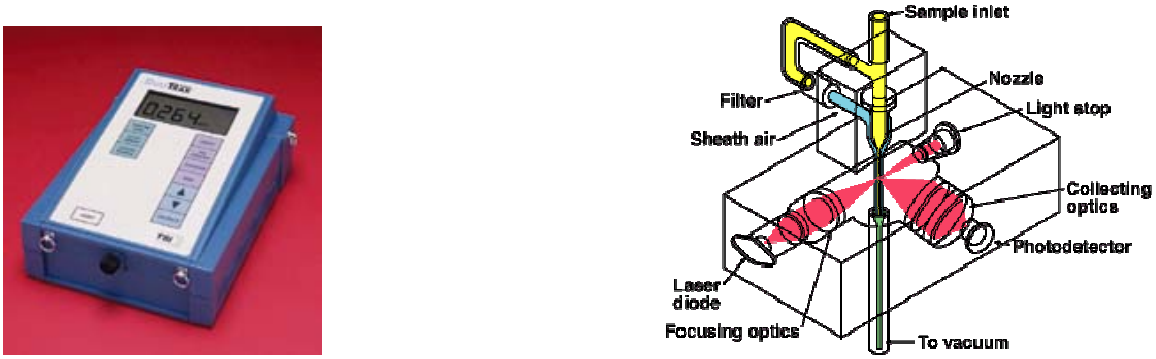

Figure 3-5. External view (a) and schematic (b) of TSI Dust Trak™ (TSI 2003).

The output of the DustTrak™ was compared to a Tapered Element Oscillating Microbalance (TEOM). Over the range of particles studied, the signals showed very good correlation, (Figure 3-6) albeit with a significant (~2.5 to 3) multiplier (under further study), suggesting the DustTrak is a suitable instrument for on-orbit measurement of the mass concentration. Prior to flight the instrument will be calibrated for the range of possible particle sizes to allow transformation of the signal to perform the moment analysis. The output will also be modeled by predicting the scattering behavior for anticipated particle sizes. These predictions can be further validated post-flight for the solid particles via TEM samples.

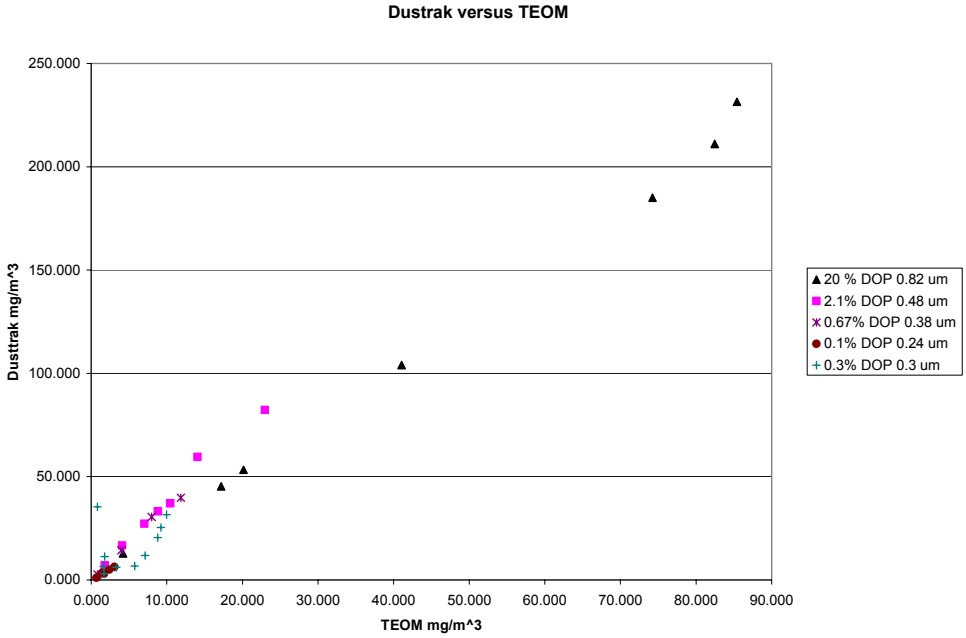

Figure 3-6. Comparison of the output of the DustTrak™ with a Taper Element Oscillating Microbalance (TEOM)
Aerosol particles were prepared using Dioctyl phthalate (DOP) solutions whose concentrations and resulting mass median diameters (μm) are indicated in the legend.

3.5.4 Thermal precipitator

Although the sample size may be statistically limited, use of thermophoretic sampling provides a valuable check of the particle size distribution. There is no substitute for seeing the actual shape and morphology of the particulate. Sampling in flames requires only the thermal gradient imposed by the

cold probe, (Urban et al 1998). In the case of our colder smoke plumes, an external thermophoretic gradient must be imposed to provide adequate sampling. The suggest method has been used previously (Cleary, 1989). Although prior applications inserted the probe directly into the flow, if care is taken, a remote system could be implemented by aspirating the smoke.

3.5.5 Space craft smoke detectors: (desired)

Implementation of the two existing NASA spacecraft smoke detectors (Figures 1-2 and 1-3) in the system will provide direct evidence of the detectability of µg smoke particulate and will be helpful in interpreting the signals from the ISS and STS systems during the remainder of their operational life. However, these instruments do not by themselves provide quantitative particulate measurements that would support design of future smoke detectors. Consequently, the use of these detectors is not required but is strongly desired. The two detector signals are very consistent with their counterparts, the DustTrak™ and the Ion Chamber.

The response of the two detectors is shown in figures 3-7 through 3-9. As seen in figure 3-7 the shuttle detector needs substantial number concentrations to generate significant signal. This is consistent with experience with residential smoke detectors which require substantial smoke concentrations to trigger an alarm. The ISS detector signal shows the expected increase in the slope with increasing particle size. Given the cubic dependence of the scattering signal on particle size in this size regime (Mie scattering), the STS and ISS detector data could not be shown on a single graph.

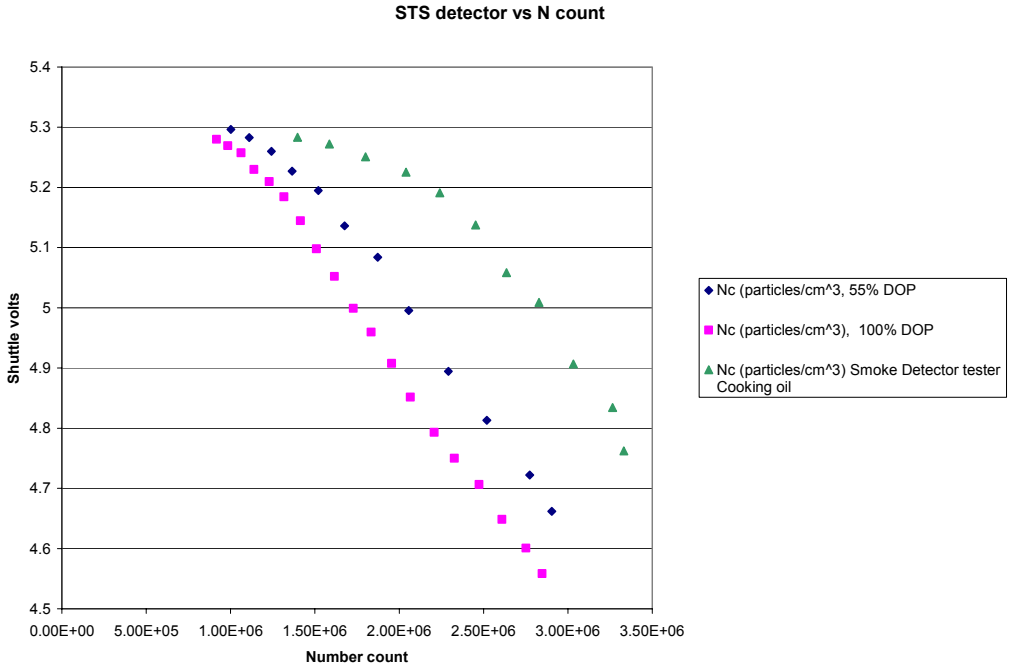

Figure 3-7. Comparison of the output of the STS ionization smoke detector with number concentration from the PTrak™ for poly-disperse aerosols.

Increased smoke concentrations produce a reduction in the voltage reported by the detector. In this plot the voltages are the output of a 2 to 1 voltage divider.

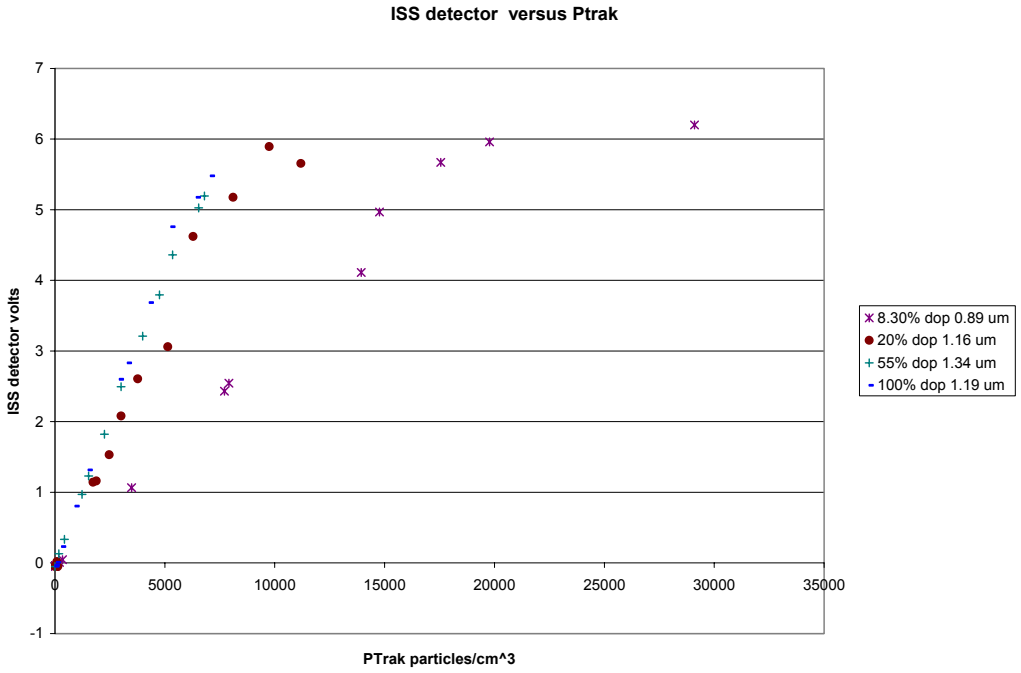

Figure 3-8. Comparison of the output of the ISS light scattering smoke detector with number concentration from the PTrak™ for mono-disperse aerosols (0.9 to 1.3 µm droplets). Aerosol particles were prepared using Dioctyl phthalate (DOP) solutions whose concentrations and resulting mass median diameters (µm) are indicated in the legend.

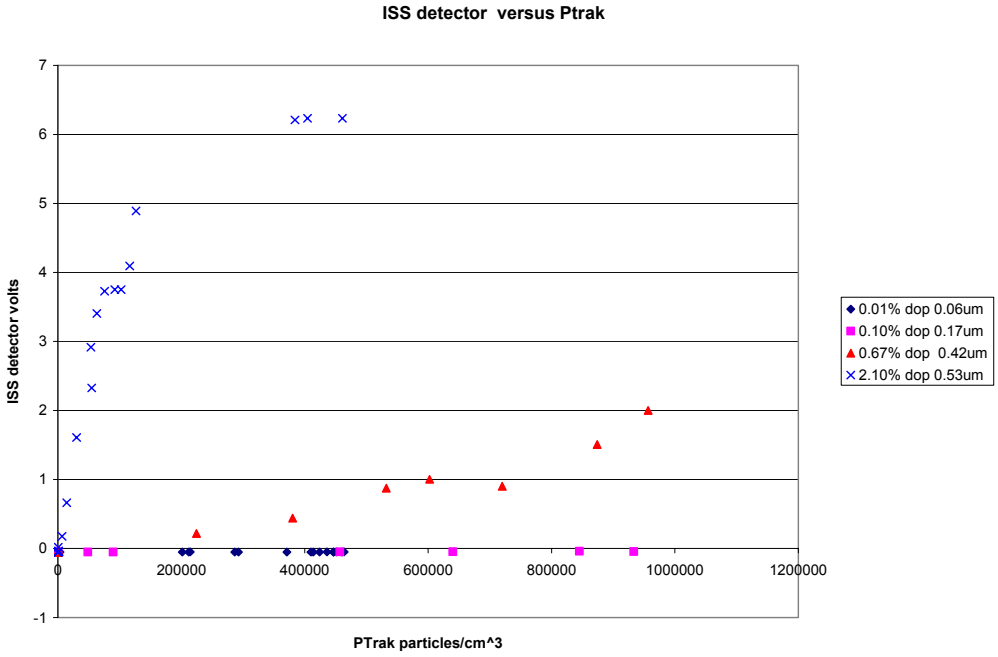

Figure 3-9. Comparison of the output of the ISS light scattering smoke detector with number concentration from the PTrak™ (0.06 to 0.5 µm droplets).

Aerosol particles were prepared using Dioctyl phthalate (DOP) solutions whose concentrations and resulting mass median diameters (μm) are indicated in the legend.

Perhaps the most difficult aspect of implementing these diagnostics is developing conditions where the diagnostics are all operating within their design range. Since each of these systems respond to a different moment of the particle distribution, their sensitivity varies with particle size. Since we are necessarily uncertain about the particle size distribution that we will see during the flight tests, some system flexibility is required to achieve mission success. Testing at NIST has established the nominal instrument sensitivities for these devices for a range of particle sizes. Using these sensitivities, table 3-3 presents the estimated signal levels for the diagnostics. As is evident in the table, it is difficult to obtain a signal on all of the systems at once; consequently dilution will be necessary either for particular instruments or by expelling multiple samples from the aging chamber.

Table 3-3: Estimated signal levels for diagnostics for monodisperse particulate

Estimates based upon calibration data determined using a monodisperse particle generator (Mulholland and Liu 1980) (In this table $\sigma_g = 1.2$)

Particle size (Count Median Diameter)	Diameter of Average mass	Number concen-tration	Mass Concentra-tion	PTrak signal	Dust Trak Signal	Ionization Chamber Signal	STS Detector Signal	ISS Detector Signal
μm	μm	particles/cc	mg/m^3	particles/cc	mg/m^3	V	V	V
0.10	0.11	1×10^4	0.01	1×10^4	0.02	0.005	11.4	1.65
0.10	0.11	1×10^5	0.06	1×10^5	0.10	0.023	11.3	1.7
0.10	0.11	1×10^6	0.61	Saturated	1.50	0.19	10.68	2.21
1.0	1.05	1×10^4	6.08	1×10^4	20.0	0.023	11.37	Saturated
1.0	1.05	1×10^5	60.81	1×10^5	Saturated	0.19	11.30	Saturated
1.0	1.05	1×10^6	608.08	Saturated	Saturated	0.95	10.69	Saturated

3.5.6 Gaseous Constituent Sensors: (desired)

Gaseous constituent sensors are a desired portion of the proposed investigation and there is less reason to suspect that the gaseous product distribution will change in low gravity compared to the expected changes in the particle size distribution. However, hybrid fire detectors combining aerosol and species sensors are receiving increased consideration for terrestrial applications and they hold the potential of reduced false alarm sensitivity for spacecraft applications. Even if the constituent distributions are less impacted by gravitational effects, interpreting the signal level requirements for both sensor types will be substantially facilitated by a series of simultaneous measurement in a relevant environment. The SAME experiment offers an opportunity to make these measurements that will not be seen again for quite some time. To evaluate whether candidate gaseous constituent sensors are likely to have reasonable signals for the SAME tests, a series of tests were conducted with several candidate gaseous constituent sensors.

A schematic of the test configuration is shown in figure 3-10. The samples are placed at the entrance to the aging chamber inlet elbow. The geometry of this component is the same as planned for the space flight experiment and is used for all testing to maintain flow consistency. The elbow is mounted vertically 20 – 25 cm from the top of the work platform and inside an enclosure to prevent room air currents from interfering with the sample. The cap on the outlet of the aging chamber elbow has a nipple with a flexible tube that will be connected to the manifold for the gas sensors. The flow across the sample and through the diagnostics was produced by a vacuum source and controlled by a mass flow controller. The SAME space flight experiment requires that a velocity of 5 cm/s is maintained through the flow duct and this was provided for each test condition. A photo of the test facility including flow enclosure, sensor package, and data acquisition and control computers is shown in figure 3-11.

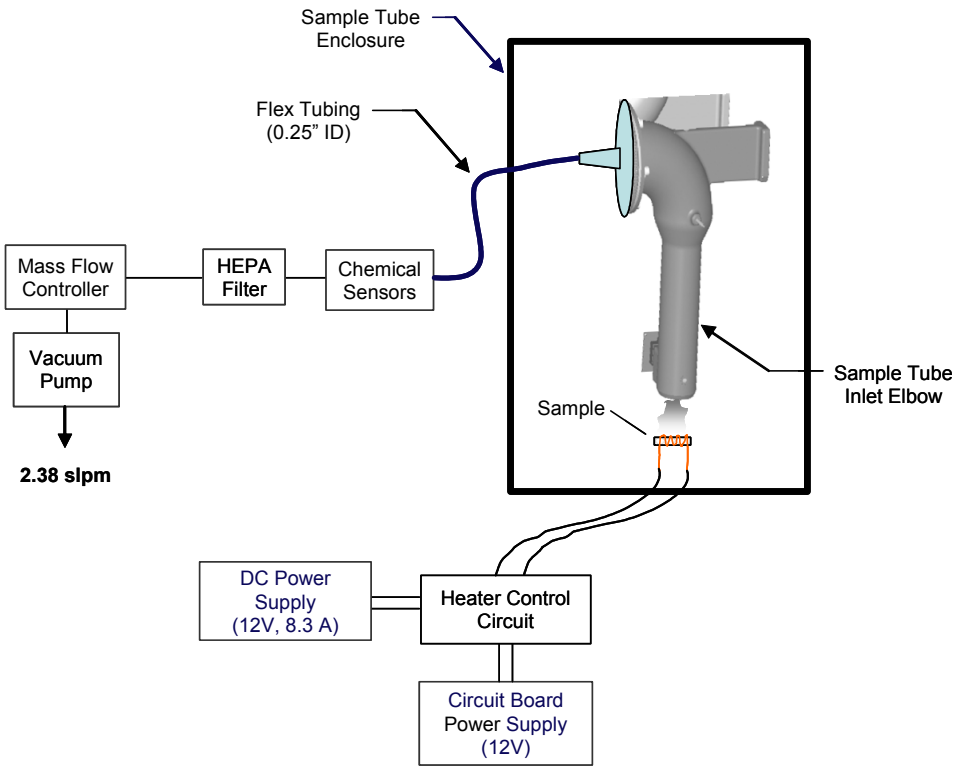

Figure 3-10. Schematic of the Test Facility

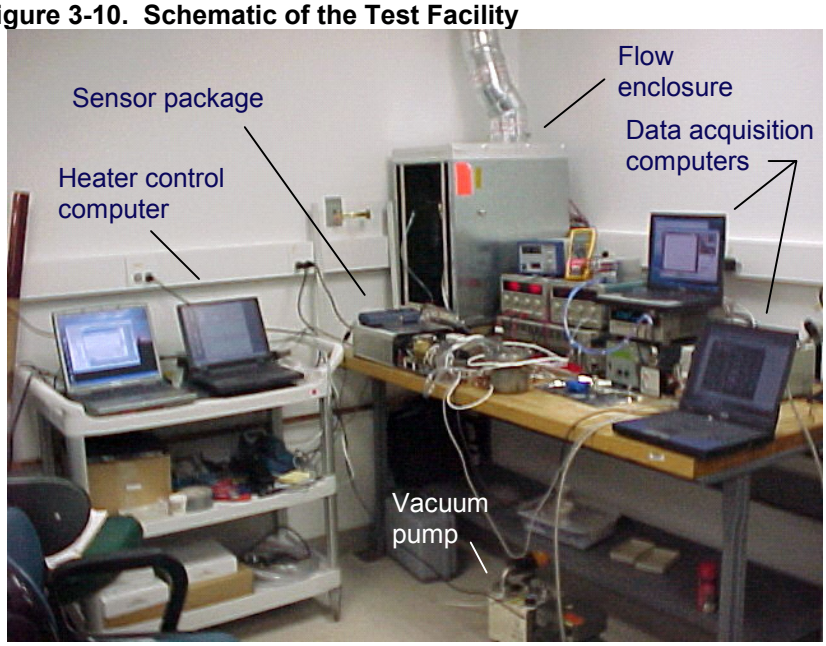

Figure 3-11. Photograph of the test facility

The sensor package used in these tests contained the following sensors: CO, CO_2, total HC, humidity, H_2, and an ion barrier cell particulate sensor. These were packaged together into a box approximately 13" x 8" x 5" high. A photo of this package is shown in figure 3-12.

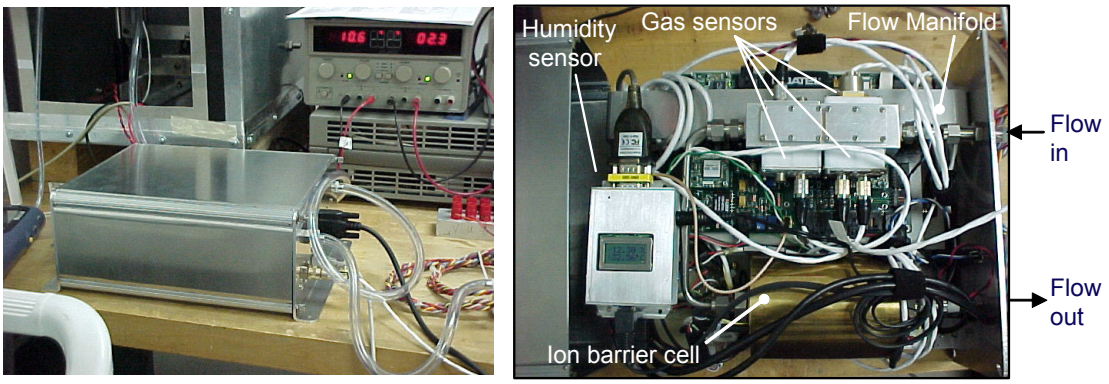

a. sensor package with cover b. Internal view of sensor package

Figure 3-12. Sensor package

The test conditions were selected to duplicate the planned operation of the SAME experiment. Previous testing had determined the heater temperature required to yield a mass loss of 2 mg from each sample within 60 sec and correlated this to the resistance of the heater wire. A heater control circuit adjusted the current through the wire to maintain the desired resistance and thereby, maintain the wire temperature. The mass of each sample had been determined prior to the test so that measuring the post-test mass could verify the operating condition in terms of desired mass loss.

The test was conducted by installing a sample into the flow facility, verifying the desired air flow rate over the sample and that the sensors were at a proper operating level. When all instruments were ready, the power to the heater was initiated and the time recorded for correlation with the sensor output which was recorded by the data acquisition computers. The heater power turned off automatically after 60 seconds and data collection was continued until the sensor output began to decrease toward the baseline levels.

Test Matrix

Tests were conducted on four sample materials to be used in the SAME experiment. These were (1) Teflon, (2) cotton lamp wick, (3) silicone rubber, and (4) Kapton. The initial test for each sample was conducted at the resistance ratio (R_T/R_0) that produced the desired 2 mg mass loss within 60 sec. Subsequent tests were conducted at higher ratios (higher temperatures) although these were always within the operating range of the SAME experiment. (If adequate sensor performance was not obtained within this operating range, a modification would be required to the design, operation, and/or the safety documentation of the baselined experimental package. This would make the addition of these sensors to the diagnostic package much less viable.) Nine conditions were performed for the cotton lamp wick samples to quantify measurement repeatability while five were performed for the other samples. The complete test matrix is shown in table 3-4.

Table 3-4: Test Matrix

Sample	R_T/R_0								
	1	2	3	4	5	6	7	8	9
Teflon	1.447	1.5	1.46	1.455	1.447	**	**	**	**
Cotton	1.24	1.24	1.35	1.24	1.3	1.275	1.24	1.275	1.35
Silicone rubber	1.327	1.45	1.35	1.375	1.327	**	**	**	**
Kapton	1.221	1.22	1.45	1.3	1.221	**	**	**	**

Preliminary Test Results

The detailed sensor output is still being analyzed; however, qualitative notes taken during the tests indicate which sensors were responding for each test condition shown in table3-5. Teflon, cotton, and silicone rubber produced readings on the HC and CO gas sensors and the ion barrier cell (IBC) particulate sensor at the SAME baseline resistance ratio. The cotton sample produced no output on the CO_2 sensors although this sensor did respond for Teflon and silicone rubber. There was no noticeable response for the Kapton samples other than some production of particles.

At higher resistance ratios, the CO, HC and IBC sensors responded for all samples. The CO_2 sensor responded for Teflon, cotton, and silicone rubber but not for Kapton. Teflon and silicone rubber even produced an output from the H_2 sensor. (Data from these tests will be presented at the SAME requirements review.)

Table 3-5: Qualitative Sensor Results from Overheated Samples

Sample	Baseline R_T/R_0					Elevated R_T/R_0				
	HC	CO	CO_2	H_2	IBC	HC	CO	CO_2	H_2	IBC
Teflon	x	x	x		x	x	x	x	x	x
Cotton	x	x			x	x	x	x		x
Silicone rubber		x	x		x	x	x	x	x	x
Kapton					x	x	x			x

Based on these preliminary data, it can be concluded that the suite of sensors used in this advanced fire detector can respond to the samples and test conditions in the SAME experiment. Most sensors respond satisfactorily at the SAME baseline conditions except for Kapton where only particles were detected. At slightly higher heating levels, the majority of the chemical sensors responded for all samples although there was no response on the CO_2 sensor for Kapton and no H_2 response for cotton and Kapton. All of these conditions are within the planned operational range of the SAME experiment.

3.5.7 Microgravity requirements

The presence of forced flow in the duct and the relatively low temperatures makes this experiment less sensitive to gravity than some low inertia flames. Based upon scaling analysis it is expected that the g-level requirements should keep the gravitational induced velocities below the duct flow velocity.

3.6 Test matrix

The exact operating conditions will be varied based upon the results of prior tests; however the test matrix is anticipated to cover two weight loss rates, two air flow rates, and two aging durations. Depending upon the implementation of the experimental design, multiple aging durations may be possible with sample. This would be preferable from an up mass standpoint. More test points are strongly desired as the test matrix below has no margin for repeats of test points and each parameter is not varied over more than 2 conditions.

Table 3-6: Test matrix

Test Number	Sample Material	Air Flow	Weight loss rate	Aging Duration
		(cm/s)	mg/minute	minutes
1	Teflon™	5	2	1
2	Teflon™	5	1	1
3	Teflon™	5	2	20
4	Teflon™	10	2	1
5-8	Kapton™: same conditions as 1-4			
9-12	Silicone Rubber: same conditions as 1-4			
13-16	Lamp Wick: same conditions as 1-4			
17-20	Dibutyl Phthalate: same conditions as 1-4			
21-40	Additional desired points to provide repeats and to fill in test parameters			

4 Success criteria

4.1 Science success criteria

Minimal success: Video data and required moment data obtained for at least two DBP runs and at least 4 of the lamp wick and silicone rubber runs or two of the three moments are obtained for all samples.

Significant success: Minimal Success plus video and required moment data from all three instruments returned from 75% of the runs or from 50% of the runs with at least one from each sample and with successful TEM samples from at least one Teflon and one Kapton run.

Complete success: Aging chamber functions properly with all required data (plus smoke detector data) returned and TEM grids provided effective particle size measurements.

4.2 Hardware success criteria

Minimal success: Sample heater system and flow/diluter system functions properly. Required moment instruments function for at least half of the runs or two different moment instruments function for all samples.

Significant success: Minimal success plus the required moment systems function for 75% of the runs or for 50% of the runs with at least one from each sample with successful thermal precipitator operation during the Teflon, and Kapton runs.

Complete success: Significant success plus all required systems and the smoke detectors function properly for the entire test matrix with sensor data returned for all test points and the aging chamber providing requested aging durations.

5 Post-flight data deliverables

The following deliverables must be supplied by NASA to the PI for post-flight analysis:

1. Sample masses before and after each test.

2. Operations log with start times for each test point.

3. Video recording of smoke generation process with time correlation to activation of the sample heater.

4. Data from experimental monitoring measurements and experimental diagnostics.

5. TEM grids from the thermal precipitator.

6. Post-flight calibration records (if available) for the monitoring sensors.

7. Turnover of the moment diagnostic instruments (if available) for post flight calibration.

6 Justification for extended duration microgravity environment

The CSD experiment demonstrated unequivocally that buoyancy affects the detectability of smoke particulate by spacecraft smoke detectors. This effect is believed to be the result of growth of the smoke particles in the weak flows seen in spacecraft conditions. More detail is needed on the particle size distribution of smoke from practical materials, particularly from materials that produce liquid smoke aerosols. The objective of this program is to study preignition particulate release from various spacecraft materials under conditions typical of those seen on spacecraft. These conditions include ventilation flow velocities as low as 5 cm/s under non-buoyant conditions and low heating rates typical of a slow component failure or overheat. It is the hypothesis of this program that the absence of buoyancy induced convection together with the low ventilation flow at μg will reduce the mixing rate, allowing the smoke particles to persist in a high concentration zone for long times. The convection times for smoke in open areas in spacecraft cabin can be on the order of several minutes. Even in more actively ventilated systems, times substantially longer than those available in ground based facilities are needed before the smoke reaches the detector. A secondary hypothesis of this program is that further changes in the particle size distribution can occur under these lower-concentration “smoke aging” conditions. This aging process cannot readily be simulated in normal gravity as gravitational settling will limit the particle size distribution.

Ground based experience has shown that repeatable generation of precombustion particulate from a variety of materials requires heating times on the order of 30 to 60 seconds. After the smoke is generated, time is needed to convect the smoke from the source to the detectors followed by the several second response times of the instruments. To determine the effect of aging of the smoke, the aging time must be at least several times as long as the original smoke residence time in the high concentration zone near the source and be commensurate with expected aging times in spacecraft (order of minutes). The cumulative time required for the smoke generation and particle growth periods, suggest that test times of at least several minutes are required with the aging interval required being tens of minutes. Times of this duration are not available in ground based facilities.

7 Science operations and data analysis plan

This program will be conducted by two teams based at NASA GRC and at NIST (Gaithersburg MD). The GRC team consists of the P.I. (D. Urban) and Z.G. Yuan. They will be responsible for the daily experiment operations and test planning. It is anticipated that the TEM grid analysis will be conducted at GRC but this task may be transferred to NIST if appropriate. In the year immediately following the flight, budget augmentation will be needed to cover TEM charges.

The NIST team will consist of (G. Mulholland, J. Yang and T. Cleary). The NIST team will assist with the data analysis and will be entirely responsible for the numerical modeling.

7.1 Post flight data analysis

The average particle size and an estimate of the width of the size distribution will be estimated from various moments of the size distribution. The number distribution, $f_N(D)$, is defined as

$$f_N(D) = \frac{dN}{dD} \tag{5}$$

where dN is the number of particles per cm^3 with diameter between D and D + dD. The moments of interest consist of the number concentration, M_0, the ionization detector moment, M_1, the mass concentration moment, M_3, and the light scattering moment, M_s.

$$M_i = \int D^i f_N(D) dD \qquad i = 0,1,3 \tag{6}$$

$$M_s = \int S(\vartheta, \lambda, D) f_N(D) dD \tag{7}$$

The function $S(\theta,\lambda,D)$ represents the light scattered at angle θ from monochromatic light at wavelength λ by a spherical particle with diameter D. The D dependence for $S(\theta,\lambda,D)$ varies as D^6 for particle diameter less than 0.1λ, approximately as D^3 for particles sizes from 0.3λ to about 3λ, and then approaching the geometric optics limit of D^2 for large D.

From these moments, two mean diameters can be computed The arithmetic mean diameter ($D_{0.5}$) or $(\overline{d})$, which is equal to M_1/M_0 and the diameter of average mass ($D_{1.5}$) or $(d_{\overline{m}})$, is equal to $(M_3/M_0)^{1/3}$. The lognormal size distribution is widely used for describing the size distribution of aerosols including both flaming and non-flaming smoke. The form of the distribution is the same as the normal distribution except that the diameter is replaced with the ln D so that one has

$$f_N(D) = \frac{N_t}{(2\pi)^{1/2} D \ln \sigma_g} \exp\left(- \frac{\ln D - \ln D_g}{2 \ln^2 \sigma_g} \right) \tag{8}$$

where N_t is the total number concentration of the aerosol (=M_0), and D_g and σ_g are the geometric mean number diameter and geometric standard deviation defined by

$$\ln D_g = \int_0^\infty \ln D f_N(D) dD \Big/ \int_0^\infty f_N dD \tag{9}$$

$$\ln \sigma_g = \left[\int_0^\infty (\ln D - \ln D_g)^2 f_N(D) dD \Big/ \int_0^\infty f_N(D) dD \right]^{1/2} \tag{10}$$

For the lognormal distribution, one finds that the various diameter definitions are related to the geometric mean number diameter, D_g, via the equation [Raabe, 1971, Reist, 1984]:

$$D_p = D_g \exp(p \ln^2 \sigma_g) \tag{11}$$

For the arithmetic mean diameter, $D_{0.5}$, and the diameter of average mass, $D_{1.5}$, the corresponding values of p are 0.5 and 1.5. As an example, for a lognormal distribution with D_g=1.0 μm and σ_g=2.0, the corresponding values of $D_{0.5}$ and $D_{1.5}$ are1.27μm and 2.06 μm. Using Eq(9), one can relate σ_g to the ratio of $D_{1.5}$ and $D_{0.5}$ via the equation:

$$\sigma_g = \exp\left(\ln(D_{1.5} / D_{0.5})\right)^{1/2} \tag{12}$$

Equation (12) will be used for estimating σ_g from the moments of the size distribution function.

The analysis above will require modification for the case of the light scattering instrument, since the moment depends on particle size. In this case, the dependence of $S(\theta,\lambda,D)$ on D will be determined by the calibration measurements made with monosize aerosols that are presented in section 3.6.3. An iterative procedure will be developed to obtain the best estimates of the lognormal size distribution parameters when the moment M_s is included. The basic procedure will be as follows:

1. Determine values for the 3 moment instruments at the same time interval.
2. Calculate $D_{0.5}$, $D_{1.5}$, σ_g, D_g as described above.
3. Evaluate the change in the 3rd moment measurement due to the calculated particle size and standard deviation using instrument calibration with monodisperse particles and scattering calculations.
4. If measurement change is significant, recalculate 3rd moment and repeat steps 2 and 3.
5. When the TEM samples are available, review particle size estimates and refractive indices using TEM data.

8 References

Bukowski, R.W. and G.W. Mulholland. 1978. Smoke Detector Design and Smoke Properties. NBS Technical Note 973.

Bukowski, R. W, Peacock, R. D., Averill, J. D., Cleary, T. G., Bryner, N. P., Walton, W. D., Reneke, P. A., and Kuligowski, E. D. 2003. Performance of Home Smoke Alarms, Analysis of the Response of Several Available Technologies in Residential Fire Settings NIST Technical Note 1455, December.

Chuan, R. L. and H. D. Chen. 1986. Aerosol Characterization in an Incipient Fire. Second International Aerosol Conf., Berlin, Sept.

Cleary, T.G., 1989. Measurement of the Size Distribution and Aerodynamic Properties of Soot, Masters Degree from the University Of Maryland.

Cleary, T.G., D W. Weinert, and G.W. Mulholland, 2003."Moment Method for Obtaining Particle Size Measures of Test Smokes", Natl. Inst. Stand. Technol., NISTIR 7050.

Friedman, R., 1992. Fire Safety Practices and Needs in Human-Crew Spacecraft, *Journal of Applied Fire Science*, 2:243-259.

Friedman, R., 1994. Risks and Issues in Fire Safety on the Space Station, NASA TM 106430.

Ku, J.C., D.W. Griffin, Greenberg, P. S., and J. Roma. 1995: *Combustion and Flame*, 102:216-218.

Greenberg, P. S., K. R. Sacksteder and T. Kashiwagi. 1995. Wire Insulation Flammability Experiment, NASA CP 3272 V II.

Hinds, W. C. 1999. *Aerosol Technology*, Second Edition, Wiley Interscience, New York.

Liu, B. Y. H., K. L. Rubow, P. H. McMurry, T. J. Kotz and D. Russo. 1991. Airborne Particulate Matter and Spacecraft Internal Environments, SAE Technical Paper 911476, 21st International Conference on Environmental Systems, San Francisco, CA , July 15-18.

Martin, C.E. and R.C. DaLee, 1993. Spacecraft Fire Detection and Suppression (FDS) Systems: An Overview and Recommendations for Future Flights, SAE Technical Paper 932166, 23rd International Conference on Environmental Systems, Colorado Springs, CO, July 12-15.

McGrattan, K.B., Baum, H.R., Rehm, R.G., Hamins, A., and Forney, G.P., 2000a. Fire Dynamics Simulator – Technical Reference Guide, NISTIR 6467, U.S. Department of Commerce, Washington D.C.

McGrattan, K.B. and Forney, G.P., 2000b. Fire Dynamics Simulator – User's Manual, NISTIR 6469, U.S. Department of Commerce, Washington D.C.

McKinnie, J., 1997. Fire Response Aboard the International Space Station, SAE Technical Paper 972334, 27th International Conference on Environmental Systems, Lake Tahoe, NV, July 14-17.

McLin, J. 1993. Smoke Comparison Test Report Doc. # 93-05902, Allied Signal Aerospace.

Mulholland, G.W. and Liu, B.Y.H., 1980. Response of Smoke Detectors to Monodisperse Aerosols, *J. Research of the National Bureau of Standards*, 85:223-238.

Mulholland, G.W. and Ohlemiller, T.J., 1982. Aerosol Characterization of a Smoldering Source, *Aerosol Science and Technology,* 1: 59-71.

Mulholland, G.W., 1985. Global Soot Growth Model, Proceedings of the First International Symposium on Fire Safety Science, edited by C.E. Grant and P.J. Pagni, Hemisphere Pub, Washington, 709-718.

Mulholland, G.W., Bryner, N., Liggett, W., Scheer, B.W., and Goodall, R.K., 1996. Selection of Calibration Particles for Scanning Surface Inspection Systems, *Proceedings of the Society of Photo-Optical Instrumentation Engineers*, 1996: 2862: 104-118.

National Research Council, 1975. Fire Detection for Life Safety, National Academy of Sciences, Washington D.C.

Nguyen, H.V., Okuyama, K., Mimura, T., Kousaka, Y., Flagan, R.C., and Seinfeld, J.H., 1987. Homogeneous and Heterogeneous Nucleation in a Laminar Flow Aerosol Reactor, *J. Colloid Interface Sci.*, 119:491-504.

Paul, M., F. Issacci, G. E. Apostalakis and I. Catton. 1993. *ASME-HTD* Vol. 235:59-66.

Peterson, T.W., Gelbard, F., and Seinfeld, J.H., 1977. Dynamics of Source-Reinforced, Coagulating, and Condensing Aerosols, *J. Colloid and Interface Sci.,* 63: 426-445.

Raabe, O.G., *J. Aerosol Sci.*, 1971. 2: 289.

Reist, P.C. 1984, *Introduction to Aerosol Science*. Macmillan Pub. Co., NY, NY.

Srivastava. R., J.T. McKinnon and P. Todd1998. Effect of Pigmentation in Particulate Formation from Fluoropolymer Thermodegradation in Microgravity, AIAA 98-0814, Aerospace Sciences Meeting, Reno NV, Jan 12-15, 1998.

Steisslinger, H. R., D. M. Hoy, J. A. McLin and E. C. Thomas. 1993. SAE Paper 932291.

TSI Incorporated, 2003. Product literature, 500 Cardigan Road, Shoreview, MN 55126 USA

Urban, D. L., D. W. Griffin and M.Y. Gard, 1997a. “Detection of Smoke from Microgravity Fires,” 1977 Technical Meeting of the Combustion Institute Central States Section, Point Clear, Alabama, Proceedings pp. 6-11.

Urban, D. L., D. W. Griffin and M.Y. Gard, 1997b. “Comparative Soot Diagnostics: 1 Year Report,” Proceedings of the USML-2 and USMP-3 Joint Launch plus 1 Year Conference, National Academy of Science, Washington D.C. February.

Urban, D.L., Z.-G. Yuan, P.B. Sunderland, G.T. Linteris, J.E. Voss, K.-C. Lin, K. Sun and G.M. Faeth, 1998. Structure and Soot Properties of Nonbuoyant Ethylene/Air Laminar Jet Diffusion Flames, *AIAA Journal*, V36 p1346-1360.

Wilck, M. and Stratmann, F., 1997. A 2-D Multicomponent Modal Aerosol Model and Its Application to Laminar Flow Reactors, *J. Aerosol Sci.*, 28: 959-972.

Yang, J.C., Donnelly, M.K., Prive, N.C., and Grosshandler, W.L., 1999. “Dispersed Liquid Fire Suppression Screen Apparatus,” NISTIR 6319, U.S. Department of Commerce, Washington D.C, July.

Dobbins, R.A. and Mulholland, G.W., 1984. Interpretation of Optical Measurements of Flame Generated particles, *Combustion Science and Technology,* 40: 175-191.

McGrattan, K.B., G.P. Forney, J.E. Floyd, and S. Hostikka, 2001. Fire Dynamics Simulator (Version 2) – User’s Guide, NISTIR 6784, U.S. Department of Commerce, Washington DC, November.

Fuchs, N.A. and A.G. Sutugin, 1970. Highly Dispersed Aerosols, Ann Arbor Science Publishers, Ann Arbor.

Appendix A: Aerosol Dynamics Modeling

The main objective of the aerosol dynamics modeling effort is to determine the distance from the condensable vapor source at which condensational aerosol growth essentially ceases. This distance is needed to facilitate the design of the SAME experimental hardware. Two approaches have been taken to address this problem. The first involved the use of detailed computational fluid dynamical (CFD) calculations with nucleation and growth of the aerosol, and the second involved the use of a simplified global aerosol dynamics model based on the results from the CFD calculations without aerosol dynamics coupling.

For the detailed CFD approach, the NIST Fire Dynamics Simulator (FDS version 2) was modified to incorporate homogeneous nucleation and diffusion-limited condensational growth to model aerosol dynamics with two-phase heat and mass transfer. The computational procedure involves the following steps. The velocity, temperature, and concentration fields were first determined. From these results, the saturation ratio field was computed. Homogeneous nucleation occurred when a critical saturation ratio was reached. The critical saturation ratio used in the calculations was based on a homogeneous nucleation rate of 1 nuclei/cm3 s, the only parameter assumed a priori. The critical aerosol diameter at nucleation was then calculated. Condensational droplet growth followed. The flow fields were then corrected for interfacial heat and mass transfer. The output from the original FDS was also configured to obtain droplet number density data and size distribution at single or multiple location(s) or to obtain average values over the entire plane (if desired). Other modified output features included the moments of the size distribution (from the zeroth to the sixth and the log moments) as a function of time and position. Figure A-1 is a flowchart summarizing the calculation procedure used in the modified FDS. Detailed description of the original FDS (without aerosol dynamics) can be found in McGrattan et al. (2001). Note that aerosol growth by coagulation was not considered in this work because the Lagrangian treatment of droplet dynamics used in FDS is not ideal for aerosol coagulation calculations and is therefore too computationally intensive.

The test case for the detailed CFD calculations was selected to mimic the experimental set-up, which will consist of a condensable vapor source located at a distance downstream from the entrance of the duct. The condensable vapor used in the simulation was dibutyl phthalate (DBP). This chemical compound will also be used in the experiments as a reference material for condensable liquid aerosol. The computation domain (40 cm in length, 2.8 cm $\times$ 2.8 cm cross section) used in the calculations was comparable to the proposed experimental test section. In the simulation, the aerosol generator was located at the middle of the duct and at 5 cm downstream from the inlet, the generator had a dimension of 1.1 cm x 0.44 cm x 0.44 cm, and the DBP vapor was generated through the four lateral sides of the generator with a mass flux of 5.0E-04 kg/m^2 s at 200 °C. The inlet air velocity was set at 5 or 10 cm/s at 25 °C. Both normal and zero gravity cases were run. The initial condition in the duct was set at 25 °C. The thermophysical properties of DBP were obtained from DIPPR (AIChE Design Institute for Physical Property Data) database. The number of grids used was 30 x 30 x 320. A typical run took at least 3 days to complete.

Figures A-2, A-3, and A-4 show the center x-z plane contours of mass fraction of DBP, temperature profile, and aerosol number density in the test section at 9 s respectively for normal and zero gravity conditions with 5 cm/s airflow. The z-axis is the downstream direction. These figures were generated using the SMOKEVIEW graphic package accompanied with FDS.

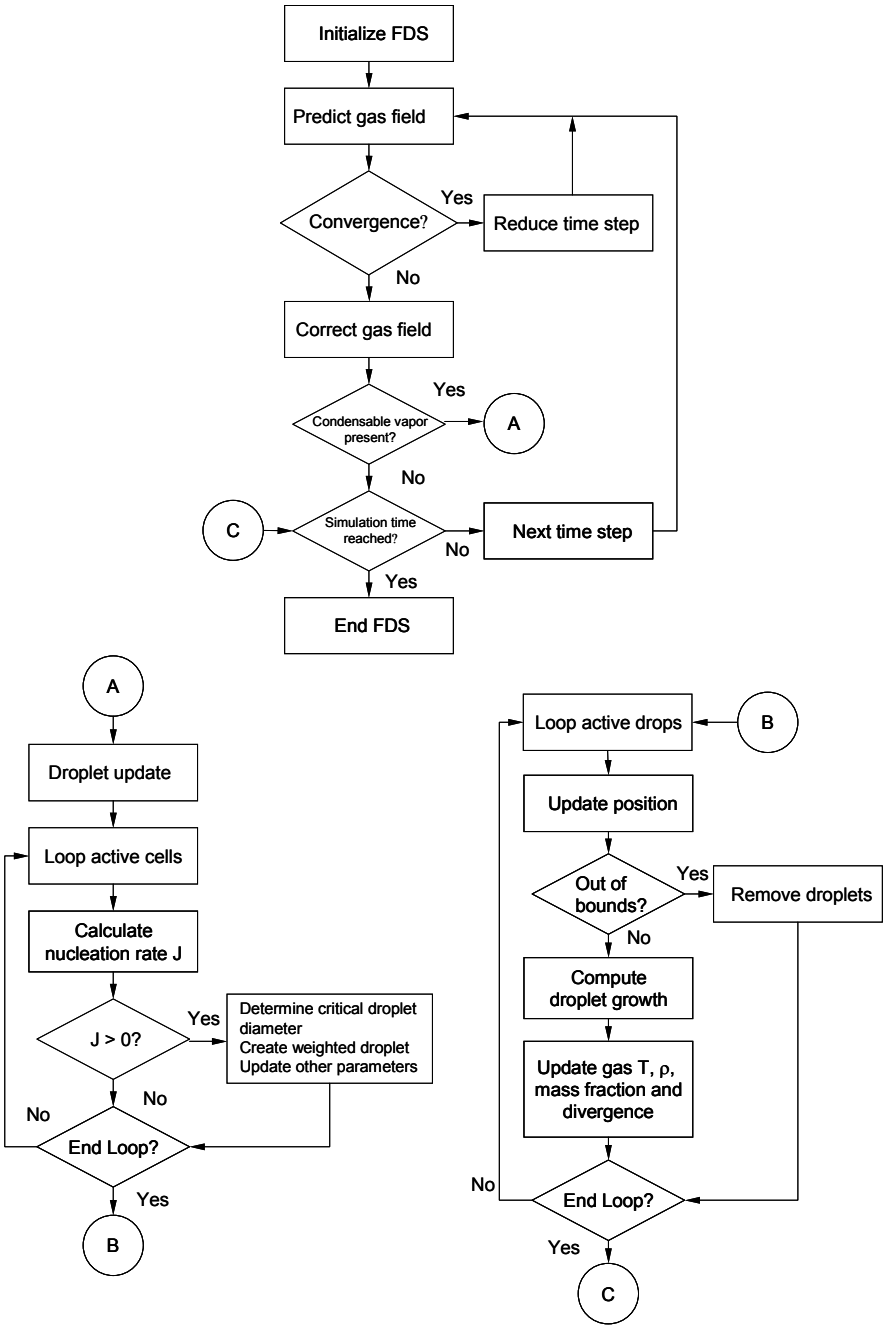

Figure A-1. Flowchart describing the computational procedure.

The near depletion of condensable DBP vapor mass fraction contour in figure A-2 and the aerosol number density contour in figure A-4 indicate nucleation and condensational growth occur in a narrow region near the centerline of the vapor source despite a wide vapor plume originated from the source. This is due to the mixing of entrained cold air with the hot vapor plume, which renders a less favorable condition (lower temperatures) for nucleation to occur near the edge of the plume. Figure A-5 shows the homogeneous nucleation rate (J) of DBP as a function of saturation ratio (S) at two different temperatures. In the figure, the intersection of the curve and the S-axis corresponds to the critical saturation ratio used in the calculations (defined as S at J = 1/cm^3 s). The critical S for nucleation to occur can be very high for DBP at lower temperature.

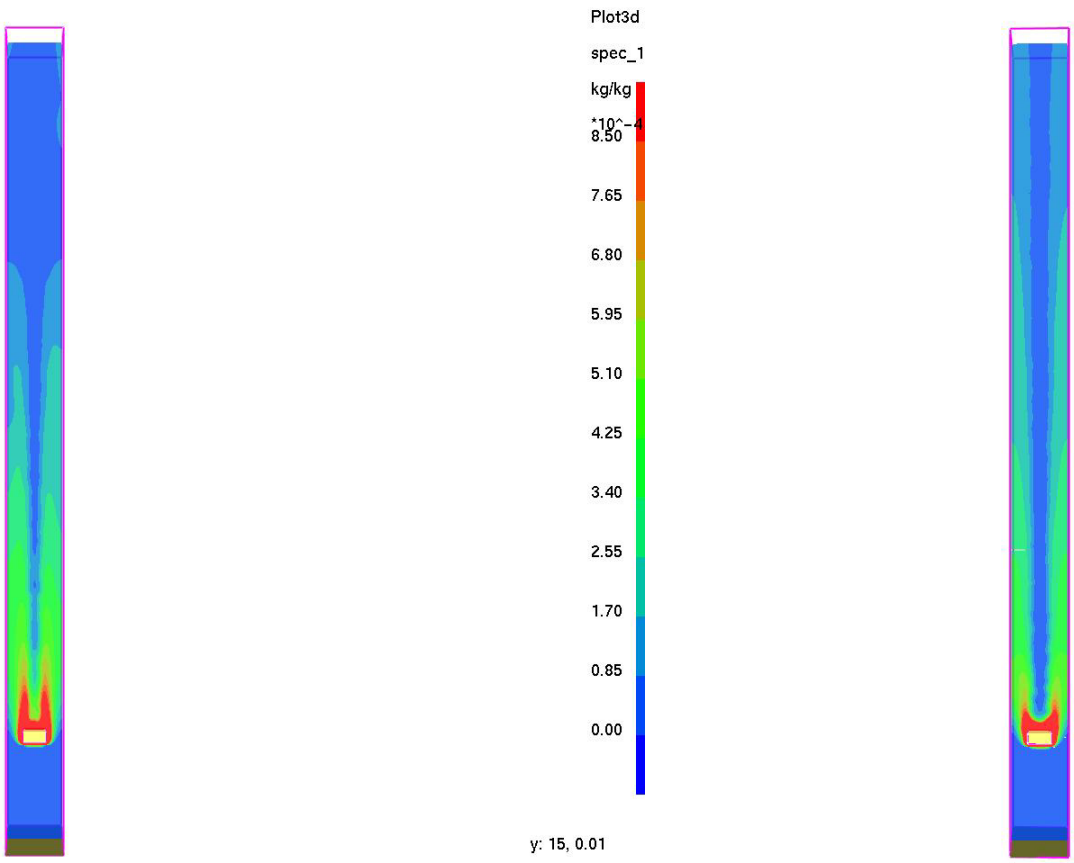

Figure A-2. DBP Mass fraction contours at normal gravity (L) and zero gravity (R) with 5 cm/s airflow.

Computational domain is 2.8 cm square cross-section and 40 cm long.

Figure A-6 shows the number-averaged aerosol diameter as a function of distance downstream of the vapor source at normal and zero gravity and two air flow velocities. Despite the evident differences in the contour plots, the planar averaging obscured the influence of gravity. A representative number-averaged aerosol diameter was obtained from the ratio of the first moment and the zeroth moment of the size distribution (averaged over the entire x-y plane at a fixed z). At lower flow velocities, the droplet size increased. At each flow velocity, the average droplet size appears to remain relatively constant indicating little condensation a short distance downstream of the vapor source. This is also supported by the mass fraction profile of the DBP vapor (see Figure A-2), which shows very low vapor mass fraction available for condensation at downstream locations not far from the vapor source. Note that the values of average droplet size and droplet number density are dependent on the nucleation rate formula used. In the calculations, the homogeneous nucleation rate was artificially increased by 1000-fold to obtain aerosol number density on the order of between 1011 /m^3 and 1012 /m^3, a value typical found in condensable aerosols, otherwise the number density obtained from the calculation without the modified homogeneous nucleation rate was one order of magnitude lower.

Simplified Global Analysis

The second approach that was used to estimate the distance from the vapor source where aerosol condensational growth ceased was based on a global analysis. The intent of this analysis is to use a simple configuration (without the complication of fluid dynamics) to simulate the growth of aerosol as it travels downstream from the source. We examine a situation wherein the aerosol number concentration *N* does not change with time *t*. The aerosol is confined within the control volume.

Condensation growth of the DBP particles in the control volume V (containing air and DBP vapor) is considered. Temperature and total available DBP vapor concentration in the control volume are varying to simulate the time-varying conditions that the aerosol encounters as it travels downstream from the source. The temperature in the control volume is prescribed as T_g, whose instantaneous value is obtained from FDS calculations. The instantaneous total DBP vapor concentration is also obtained from FDS results. The FDS calculations (no nucleation and growth) are performed to obtain steady-state temperature and available total DBP vapor concentration as a function of downstream distance from the source. Knowing the speed of the flow, the spatial profiles can be converted to temporal profiles, which can be used in the following analysis.

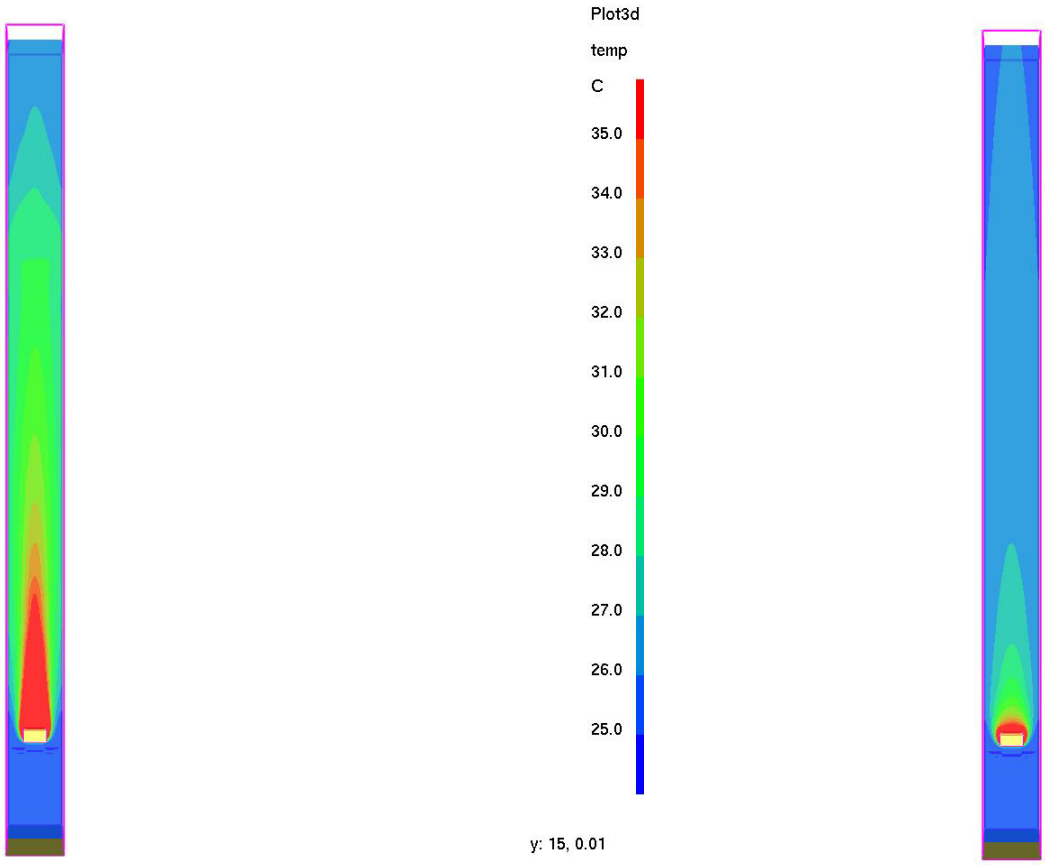

Figure A-3. Temperature contours at normal gravity (L) and zero gravity (R) with 5 cm/s airflow. Computational domain is 2.8 cm square cross-section and 40 cm long.

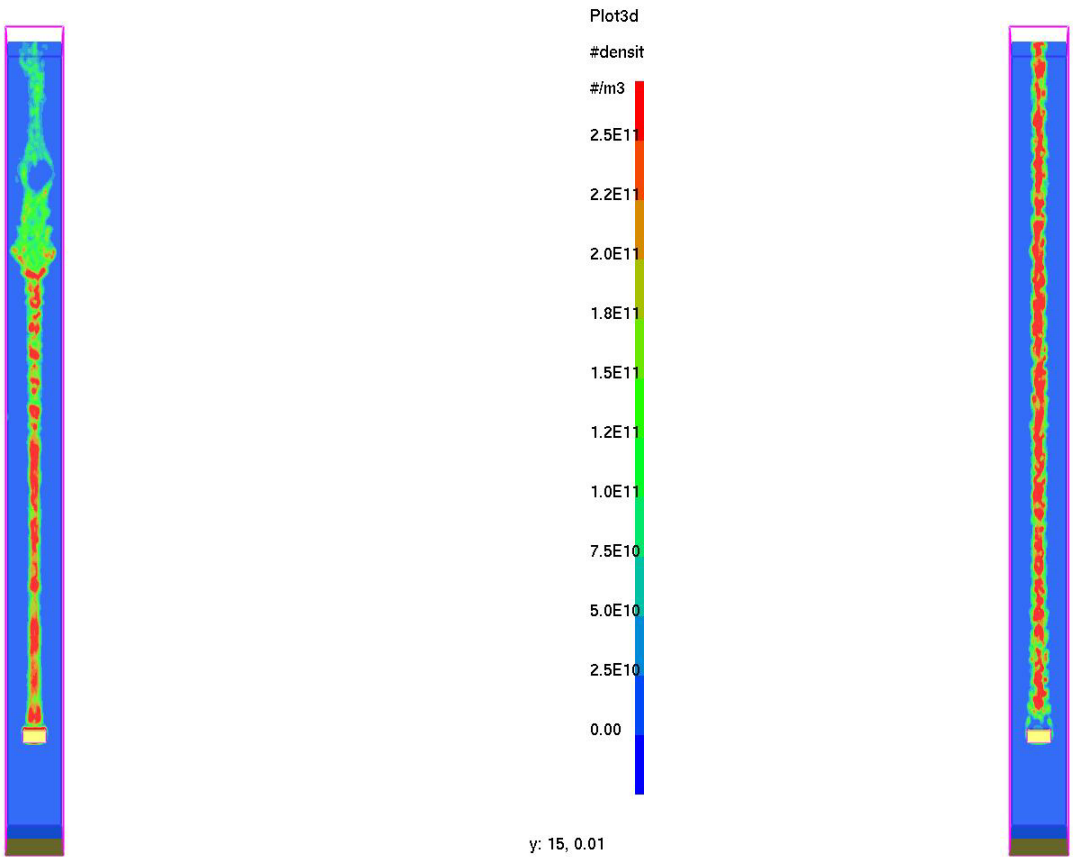

Figure A-4. Aerosol number density contours at normal gravity (L) and zero gravity (R) with 5 cm/s airflow.

Computational domain is 2.8 cm square cross-section and 40 cm long.

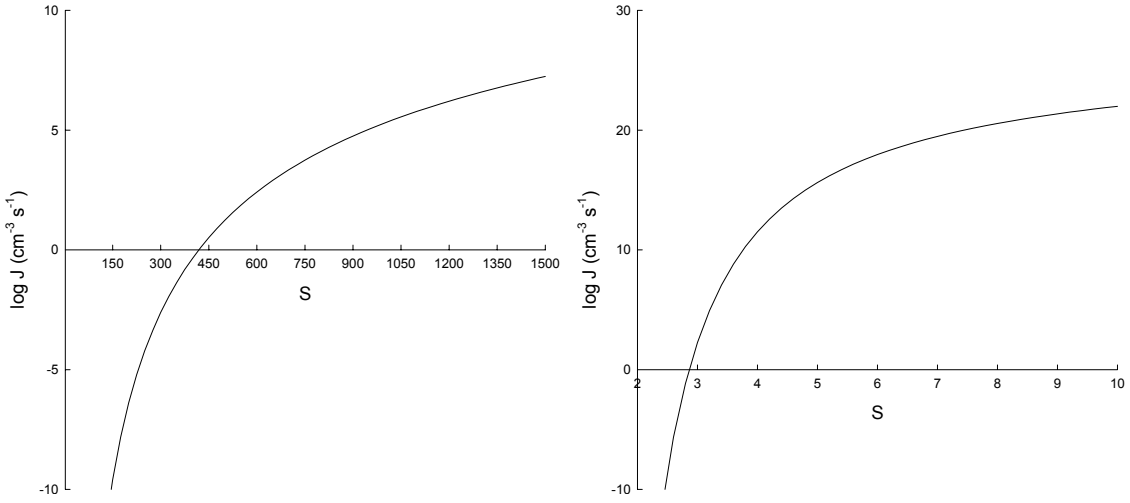

Figure A-5. Homogeneous nucleation rate J of DBP as a function of saturation ratio S at two temperatures (left 300 K, right 500K).

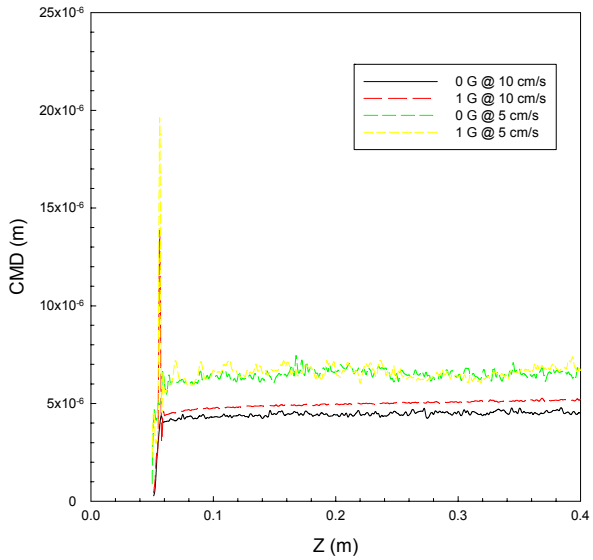

Figure A-6. Steady-state number-averaged aerosol diameter as a function of duct location for 200 C DBP source

The total aerosol mass in the control volume is

$$M_p = N V \rho_p \frac{\pi D_p^3}{6} \qquad \text{(A-1)}$$

Taking the time derivative of Equation (A-1), we obtain

$$\frac{dM_p}{dt} = \frac{N V \rho_p \pi}{2} D_p^2 \frac{dD_p}{dt} \qquad \text{(A-2)}$$

Equation (A-2) can be written in terms of Cpart.

$$\frac{dC_{part}}{dt} \equiv \frac{d}{dt}\left[\frac{M_p}{V}\right] = \frac{N \rho_p \pi}{2} D_p^2 \frac{dD_p}{dt} \qquad \text{(A-3)}$$

A total DBP mass balance gives

$$\left[\frac{dM_{total}}{dt}\right]_{from\ FDS} = \frac{dM_v}{dt} + \frac{dM_p}{dt} \qquad \text{(A-4)}$$

The first term, which is the available DBP vapor for condensation at any given time, is obtained from FDS calculations. The second term in Eq. (A-4) represents the remaining DBP vapor after condensation, and the third term represents the DBP condensed.

$$\frac{dM_v}{dt} = \left[\frac{dM_{total}}{dt}\right]_{from\ FDS} - \frac{dM_p}{dt} \qquad \text{(A-5)}$$

$$\frac{d}{dt}\left[\frac{M_v}{V}\right] = \frac{d}{dt}\left[\frac{M_{total}}{V}\right]_{from\ FDS} - \frac{d}{dt}\left[\frac{M_p}{V}\right]$$

$$\frac{dC_v}{dt} = \left[\frac{dC_{total}}{dt}\right]_{from\ FDS} - \frac{dC_{part}}{dt} \qquad \text{(A-6)}$$

Assuming ideal gas,

$$\left[\frac{dC_{total}}{dt}\right]_{from\ FDS} = \frac{d}{dt}\left[\frac{Y_{v,FDS}\ P_{total}\ MW_{DBP}}{R\,T_{g,FDS}}\right] = \frac{P_{total}\ MW_{DBP}}{R}\left[\frac{T_{g,FDS}\dfrac{dY_{v,FDS}}{dt} - Y_{v,FDS}\dfrac{dT_{g,FDS}}{dt}}{T_{g,FDS}^2}\right]$$

The change of diameter is given by

$$\frac{dD_p}{dt} = \frac{4V_m\,D_{AB}}{k\,D_p}\left[\frac{P_\infty}{T_{g,FDS}} - \frac{P_d}{T_d}\right] f(Kn) \qquad \text{(A-7)}$$

$T_{g,FDS}(t) \approx T_d(t)$ (assuming thermal equilibrium between droplets and ambient) where

$$P_\infty = Y_{v,FDS}\,P_{total}$$

$$P_d = P_{sat}\exp\left(\frac{4\sigma V_m}{k\,T_d\,D_p}\right)$$

$$\sigma = 5.9663\times10^{-2}\left(1-\frac{T_d}{T_c}\right)^{1.2457}$$

$$P_{sat} = \exp\left[160.25 - \frac{16941}{T_d} - 19.254\,\ln(T_d) + 6.6324\times10^{-6}\,T_d^2\right]$$

$$f(Kn) = \frac{1+Kn}{1+1.71\,Kn+1.333\,Kn^2}$$

$$Kn = \frac{2\lambda}{D_p}$$ (Knudsen number)

ρ_p = [A/B**(1 + (1 – T_d/C)**D)]*MW_{DBP}*1000

with A = 0.3087, B = 0.26113, C = 781., and D = 0.31804

$$V_m = \frac{MW_{DBP}}{6.023\times10^{23}\,\rho_p}$$

$$\frac{D_{AB}}{\lambda\bar{c}} = \frac{1}{3}$$ (Fuchs and Sutugin, 1970)

where $\bar{c} = \sqrt{\frac{8kT_g}{\pi m}}$

$$m = \frac{MW_{DBP}}{6.023\times10^{23}}$$

For given P_{total}, $T_g(t)$, N, $Y_v(t)$, $C_v(t=0)$, $C_{part}(t=0)$, $D_p(t=0)$, Equations (A-3), (A-6), and (A-7) can be solved simultaneously to obtain C_{part}, D_p, and C_v as a function of t.

Figure A-7 also shows a typical result using the above global approach, which shows that condensational growth occurs relatively fast and that vapor condensation ceases to occur within a short distance downstream from the vapor source. The results in figure A-6 were obtained using an initial aerosol diameter of 10 nm and number concentration of 1012/m^3. Conditions using different initial aerosol diameter and number concentration also yield similar results, i.e., condensational growth become negligible at a short distance from the source.

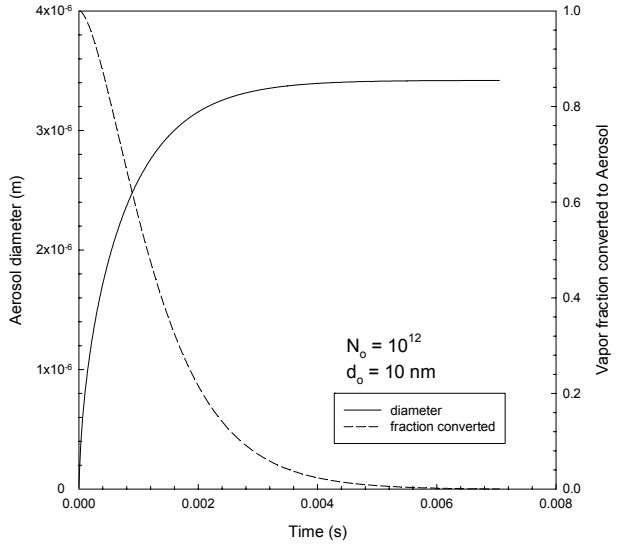

Figure A-7. Aerosol diameter and vapor fraction converted to aerosol as a function of time.

Summary

Based on the calculations from the above two approaches, condensational growth of the liquid DBP aerosol would be completed or become negligible within a duct length of 30 cm or less, which was the proposed length in the original SAME experimental design.

Nomenclature

$\bar{c}$	mean molecular speed (m/s)
C_{part}	aerosol mass concentration (kg/m^3)
C_{total}	total available vapor concentration in control volume (kg/m^3)
C_v	vapor concentration in control volume after condensation (kg/m^3)
D_{AB}	diffusivity of DBP vapor in air (m^2/s)
D_p	droplet diameter (m)
k	Boltzmann constant (= 1.38066×10^{-23} J/K molecule)
MW_{DBP}	molecular weight of DBP (= 278.3×10^{-3} kg/mol)
M_{total}	total DBP vapor mass in control volume (kg)
M_p	total aerosol mass in control volume (kg)
M_v	vapor mass in the control volume (kg)
m	molecular mass (kg/molecule)
N	aerosol number concentration (m^{-3})
P_∞	partial pressure of DBP (Pa)
P_{sat}	saturation vapor pressure of DBP (Pa)
P_{total}	total pressure of the control volume (Pa)
R	universal gas constant (= 8.3143 J/mole K)
t	time (s)
T_c	critical temperature of DBP (= 781 K)
T_d	droplet temperature (K)
T_g	ambient gas temperature (K)
V	control volume (m^3)
V_m	molecular volume of liquid DBP (m^3/molecule)
Y_v	mole fraction of DBP vapor
ρ_p	liquid density of DBP (kg/m^3)
λ	mean free path of the condensing gas molecules (m)
μ	viscosity of DBP vapor (N s/m^2)
σ	surface tension of DBP (N/m)

Appendix B: Evaporation and Condensation of Di-butyl Phthalate from a Heated Porous Cylinder

Experiments were performed to determine the effects temperature and flow on the particle formation from vaporized di-butyl phthalate (DBP). DBP has a normal boiling point of 340 ^{o}C and consequently a very low vapor pressure at room temperature. Upon heating DBP liquid, the vapors tend to form liquid aerosol droplets that persist for a relatively long time due to slow droplet evaporation at ambient conditions. In this study DBP was chosen as a surrogate to study the effects of microgravity on the size distribution of pyrolysis/smolder smokes. As a pure substance with known physical properties, it lends itself to modeling of aerosol generation and growth from established theories.

Experimental Set-up

The geometric configuration studied was a cylinder in a cross flow, where the DBP was absorbed into the porous ceramic material that makes up the cylinder. The cylinder was nominally 12.5 mm long and 9.5 mm in diameter. It was centered in a 50 mm diameter circular tube with air flow emanating from a series of screens 2 cm below the cylinder to provide a laminar, initially top-hat profile, flow. The air was filtered then metered by a mass flow controller to produce particle free air at room temperature. The flow rate uncertainty was 0.05 L/min.

The cylinder was heated electrically; an electric current flowed through a nickel-chromium wire wrapped around a ceramic screw and inserted into the cylinder. Current was supplied by a DC power supply and monitored by an ammeter. At 1.00 amps, the voltage was 4.35 volts, thus the power was 4.35 W. Once the cylinder reached steady elevated temperature, most of the energy input was removed by convection.

Figure B-1 shows a picture of the installed porous cylinder. Wires supplying power lead from the bottom of the cylinder on opposing sides, and two thermocouples (3 mil, bare bead, type K) record the temperature of the top center and bottom center of the cylinder. DBP was deposited on the cylinder by a syringe needle inserted into the tube above the source. Normally, 6 drops were deposited in a fashion to initially cover (wet) the top half of the porous cylinder. Figure B-2 shows the syringe inserted in the tube. Six droplets formed and released from the horizontal needle had an average mass of 82.2 mg with a standard deviation of 2.9 mg (mean droplet mass was 13.7 mg.)

In all cases presented here, the cylinder was preheated to a steady top and bottom surface temperature at the desired power and flow setting. After the droplets are deposited onto the surface, the surface temperature drops, the recovers as the DBP liquid is heated and distributed through the porous cylinder. Figure B-3 shows typical results for the top and bottom cylinder temperature. In this case the current was 1.00 A, and the flow was 10.0 L/min. Six droplets were deposited during a time interval between 145 s and 155 s.

The cases examined include two heating powers at a fixed flow (1.00 A and 1.10 A at 10.0 L/min), and two flows at fixed heating power (10.0 L/min and 15 L/min at 1.00 A.) The flow was sampled at various heights above the source and sent to an electrical, low-pressure impactor (ELPI) to determine mass and number size distributions and concentrations.

The sampling nozzle is an air ejector used here to collect the aerosol-laden flow. The ELPI requires 10 L/min. 1.00 L/min of particle-free air was added at the ejector, so 9 L/min were collected from the tube flow leaving the rest of the flow to bypass the nozzle. The aerosol was located at the center of the tube and the sampling nozzle was placed in the center to assure that all the aerosol was collected. Figure B-4 is a picture of the experiment showing the sampling nozzle.

Measurements

The ELPI is a commercially available instrument that measures the size distribution over an aerodynamic diameter size range of 0.03 – 10 μm in 12 discrete channels. It has a temporal resolution on the order of 5 s. A schematic diagram of the instrument is given is Figure B-5. The instrument consists of a 12-stage multi-orifice, low-pressure impactor that classifies particles according to their aerodynamic size (equivalent diameter unit density sphere.) Beginning at the first stage, particles of a

narrow size range (defined by a cut-off size) impact on that stage's collection plate, while smaller particles move on to the next stage. The process repeats itself until the last stage is reached. The flow through the instrument is 10 l/min.

Typically, cascade impactors rely on a gravimetric determination of the amount of particles collected on any stage, thus the sampling time must be sufficient to gather a weighable amount of material on each stage. This impactor is unique in that it detects particles that impact on the different stages by measuring the charge transferred to the stage from the elemental charges carried by the particles. Aerosol particles will achieve a statistically average charge level based on particle diameter, initial charge state, and exposure to charging mechanisms. The ELPI conditions the aerosol to such a state by a two-step process. The initial charge state is forced to an equilibrium, Boltzmann charge distribution by passing the aerosol through a charge neutralizer (external to the ELPI). Then, a high-voltage corona wire unipolar charger puts known a excess charge on the aerosol particles based on their size and the residence time the aerosol remains in the charging section. Excess ions and very small charged particles are removed by an ion trap just past the charger. Each impactor stage is electrically isolated and connected to an electrometer. As aerosol particles impact on the various stages, they transfer their charges and a current is measured. From the current measurement, impactor stage cut-off sizes, flow through the instrument, and the relationship between the particle size and average charge, the number of particles that impact each stage is computed and the number size distribution is characterized. The number distribution can be converted into diameter, surface area, or mass distribution, etc., and the total number, or mass (assuming spherical unit density particles) can be computed.

In these experiments the condensed liquid aerosols are spherical with a bulk density of DBP liquid (1.049 g/cm^3.) A 10-point running average was recorded at every 10 seconds for these tests.

Results

Table B-1 shows typical top and bottom cylinder surface temperatures for the three conditions examined. No DBP was deposited on the porous cylinder for these measurements. The lower bottom cylinder temperature is due the increased cooling from the flow impingement.

Table B-1: DBP vaporization conditions

Air Flow (L/min)	Current (A)	Top Temperature and (σ) ^{o}C	Bottom Temperature and (σ) ^{o}C
10.0	1.00	151.3 (0.8)	136.3 (0.2)
10.0	1.10	174.2 (0.7)	156.5 (0.2)
15.0	1.00	148.6 (0.7)	126.5 (.02)

Sampling occurred at heights from 11.5 cm to 31.5 cm above the source. Figure B-6 shows the integrated number and mass concentrations at 21.5 cm above the source at 10.0 L/min and 1.00 A. Droplets were deposited at 30 s and at about 200 s the mass concentration peaked. While the mass concentration dropped steadily for some period of time, the number concentration remained relatively flat until about 3000 s when it started to rise, reach a peak, then fall as the DBP completely evaporated from the cylinder.

The mass and number concentrations for repeated tests with sampling at different heights are show in figures B-7 to B-12 for the three separate cases. The number concentration appears to be a function of height and drops as the sampling height increases. The total aerosol mass (integral of curves) for each test is presented in figure B-13. For each separate flow/current condition, the total aerosol mass was not a strong function of height, but more aerosol was measured at higher current and lower airflow.

Arithmetic mean diameters (AMD) and mass mean diameters (MMD) were computed from the size distributions. They are presented as a function of aerosol mass flux instead of time to smooth out temporal variations between different tests. Figures B-14 to B-16 show the results for each test condition. In general, the particle size decreases as the aerosol mass flux (and presumably the total DBP flux) decreases. As the sampling height increases, the mean diameters increase. Since the total mass does not appear to be a function of height, the diameter increase appears to be due to

coagulation, and it appears that nucleation and condensation are essentially over at the first sampling position. Above 20 cm from the source, coagulation growth appears to stop also. Attempts to sample as heights closer to the source appeared to disturb the flow.

Given the constraint on the length of the aerosol growth duct, from these results it can be reasoned that a length on the order of 20 cm appears sufficient to conclude that the bulk of the DBP aerosol nucleation and condensation process has taken place, and that coagulation processes dominate any growth, at a diminishing rate as the distance increases.

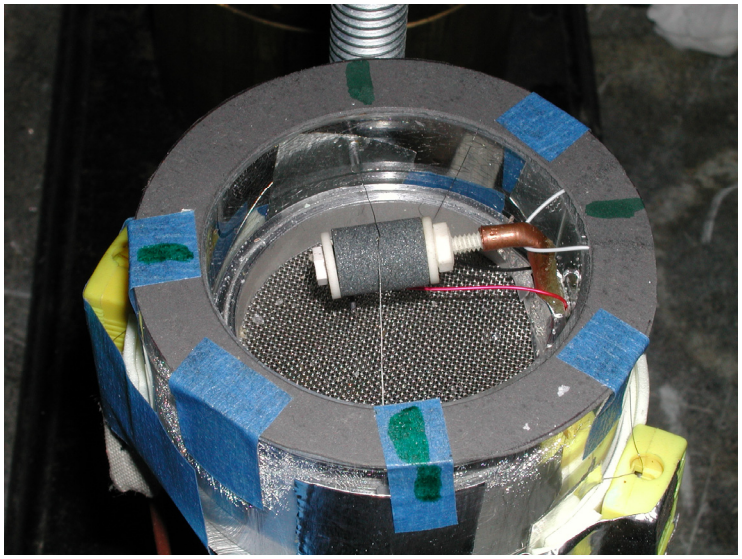

Figure B-1. Electrically-Heated Porous Cylinder.

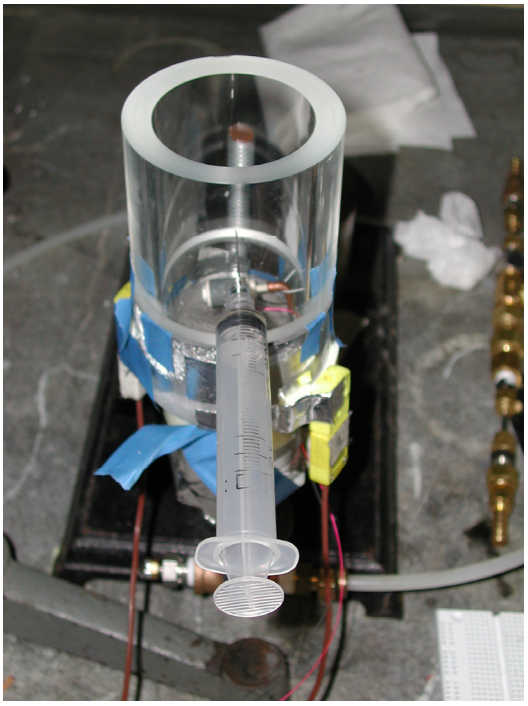

Figure B-2. Droplet deposition

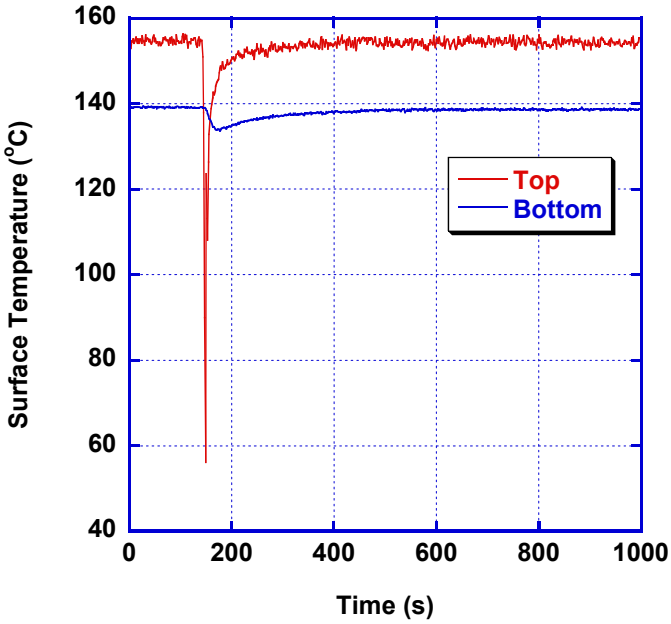

Figure B-3. Cylinder surface temperature.

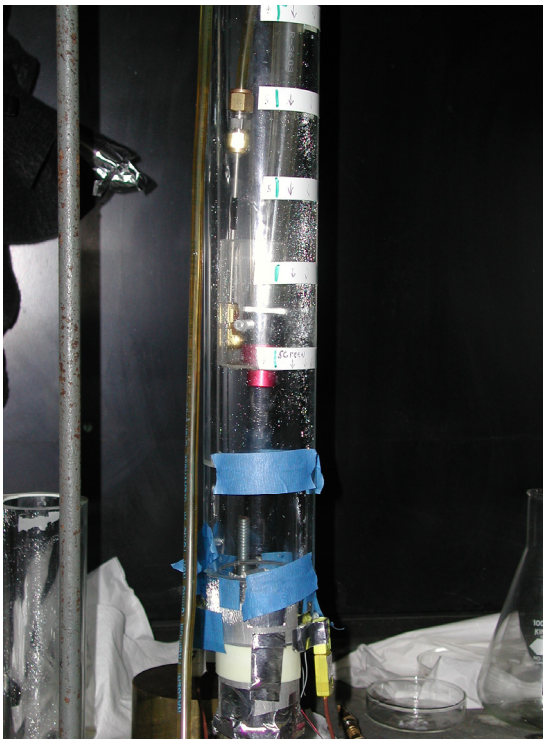

Figure B-4. Sampling nozzle at fixed height.

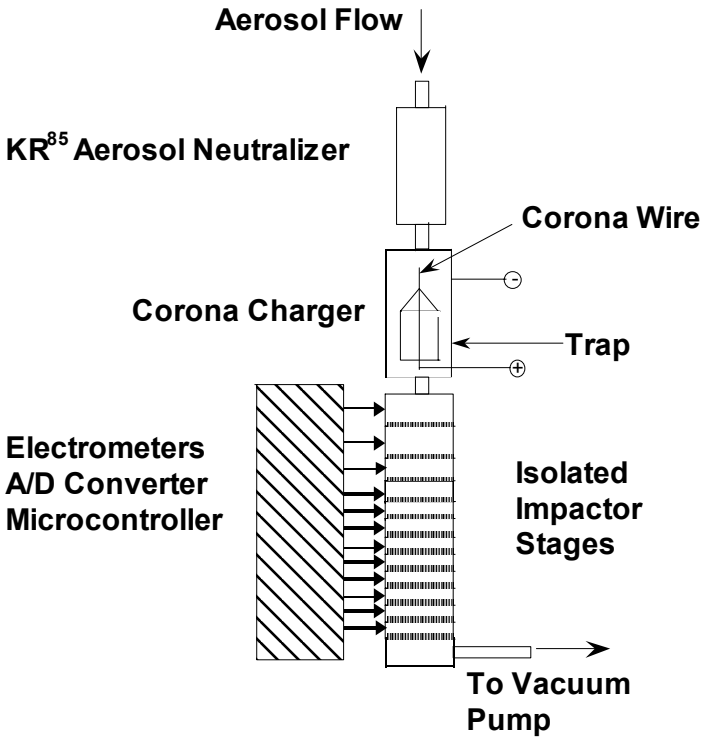

Figure B-5. Schematic of the ELPI

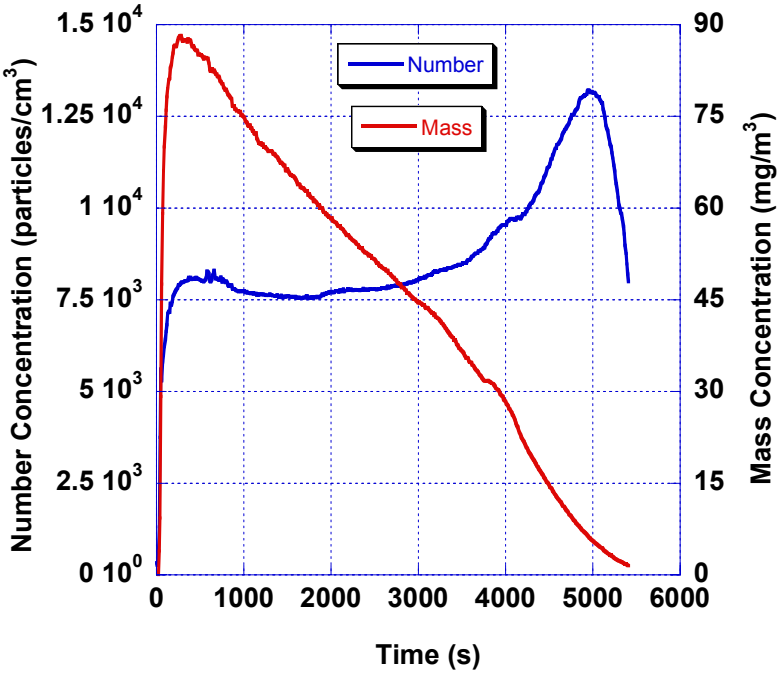

Figure B-6. Number and Mass concentration results for 10 L/min, 1.00 A at 21.5 cm sampling height.

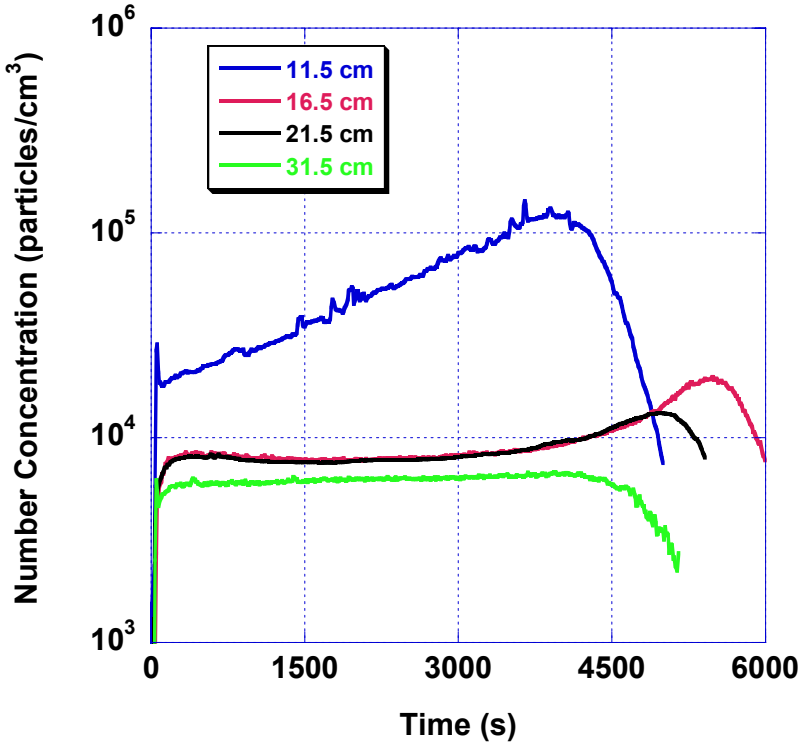

Figure B-7. Number concentration results for 10 L/min, 1.00 A at various sampling heights.

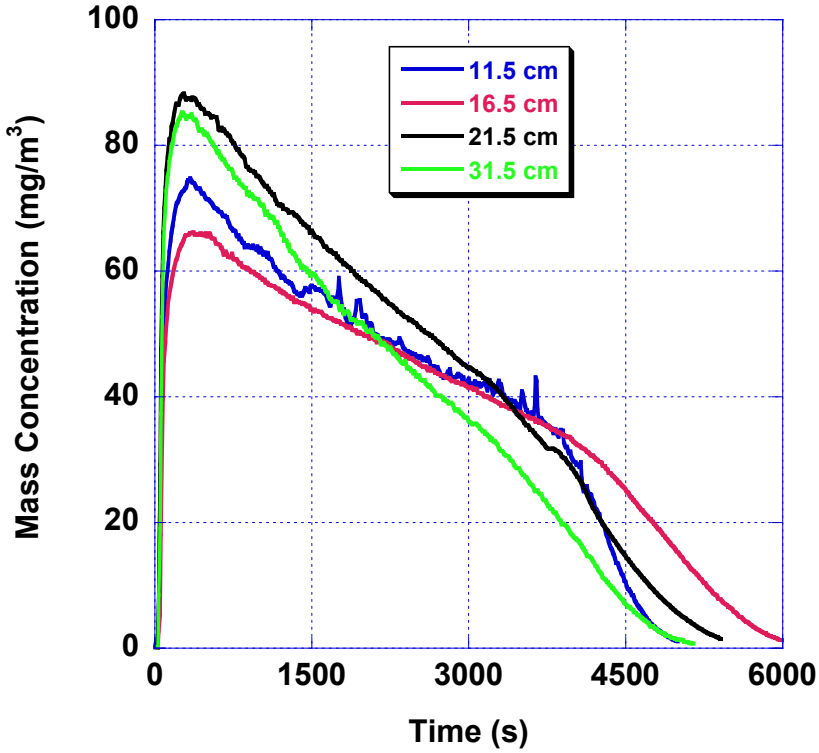

Figure B-8. Mass concentration results for 10 L/min, 1.00 A at various sampling heights.

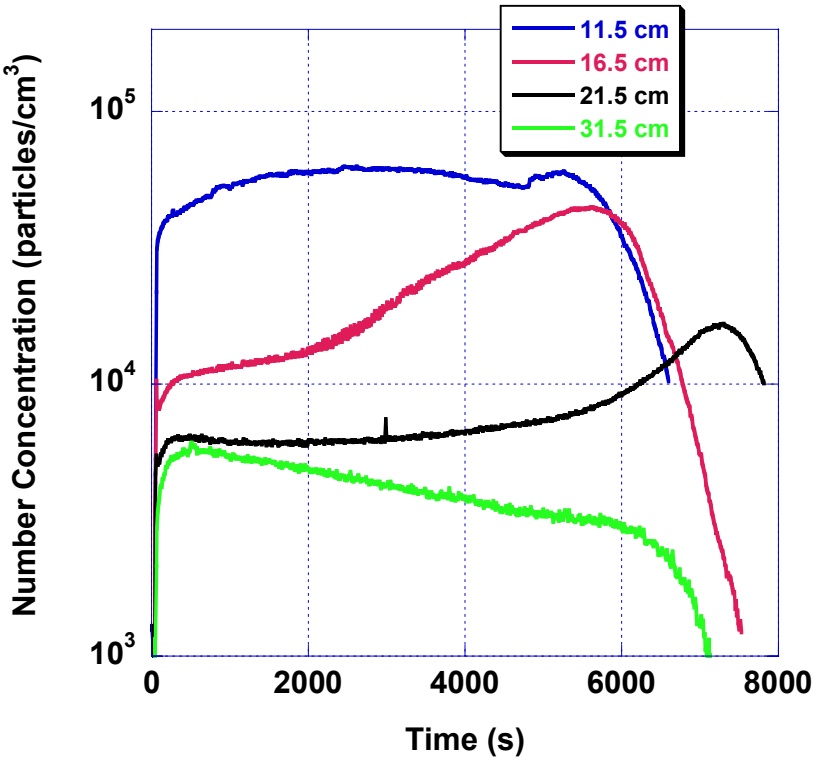

Figure B-9. Number concentration results for 15 L/min, 1.00 A at various sampling heights.

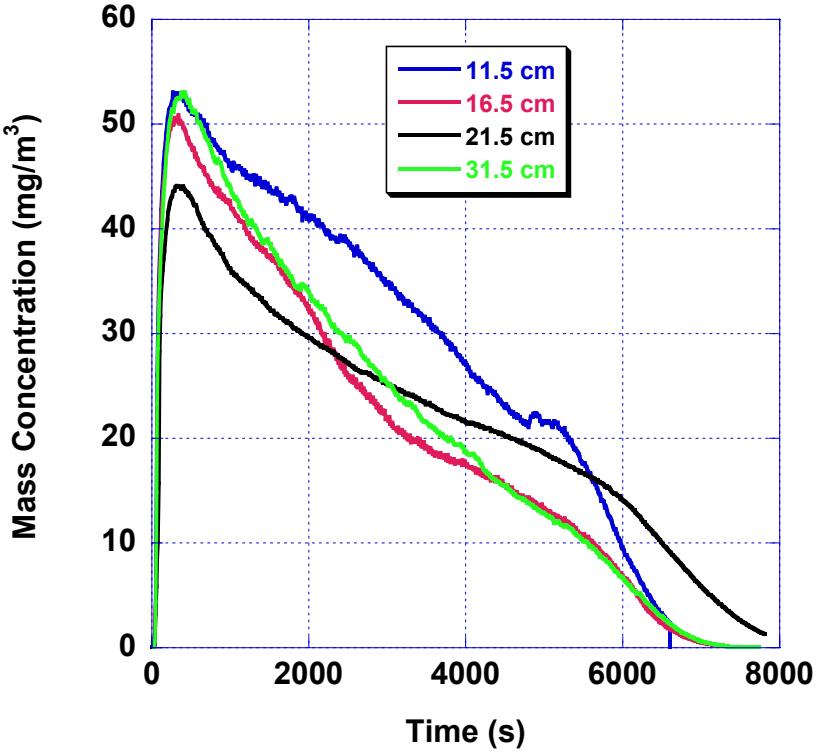

Figure B-10. Mass concentration results for 15 L/min, 1.00 A at various sampling heights.

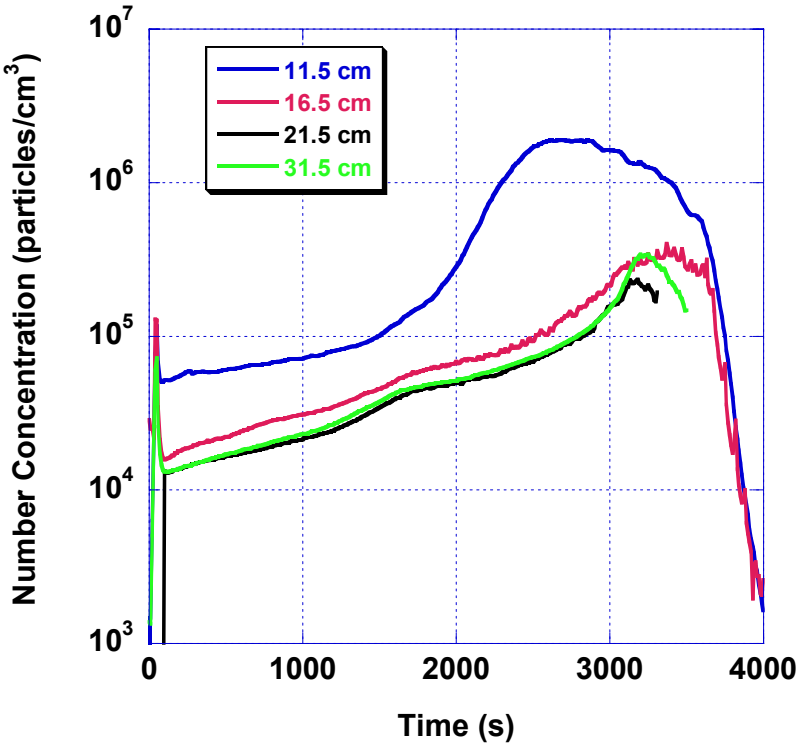

Figure B-11. Number concentration results for 10 L/min, 1.10 A at various sampling heights.

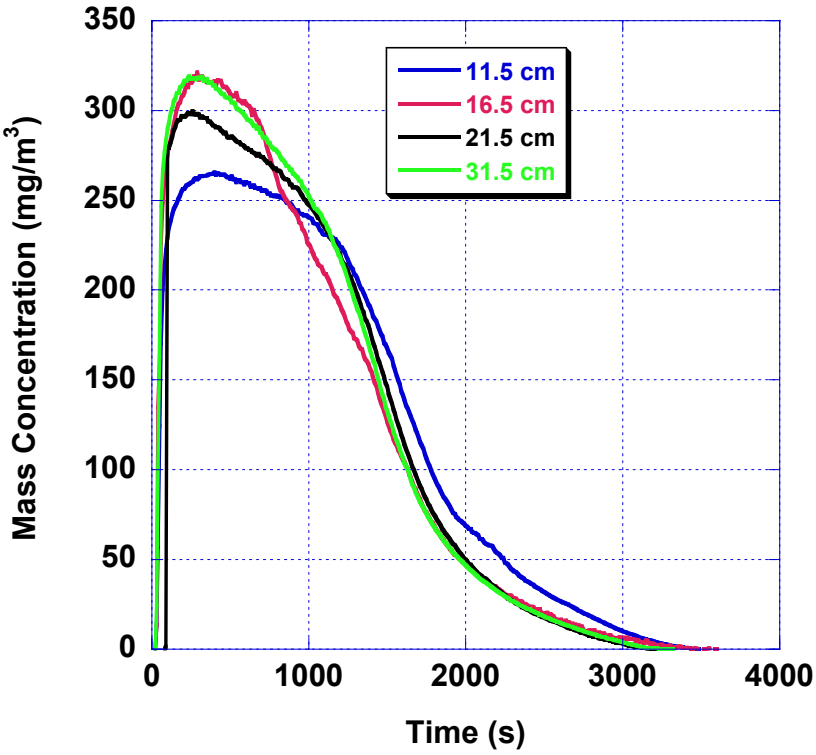

Figure B-12. Mass concentration results for 10 L/min, 1.10 A at various sampling heights.

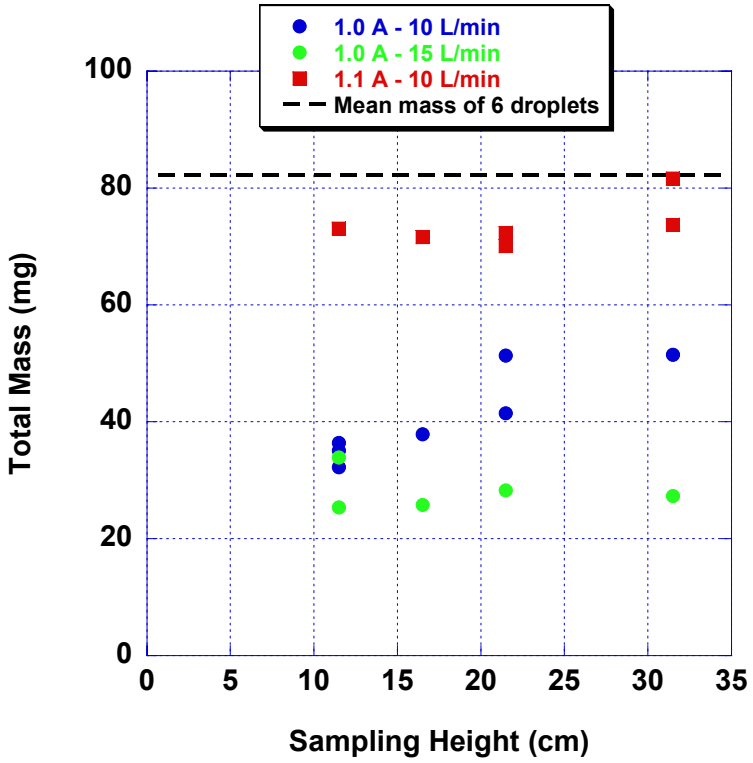

Figure B-13. Integrated aerosol mass.

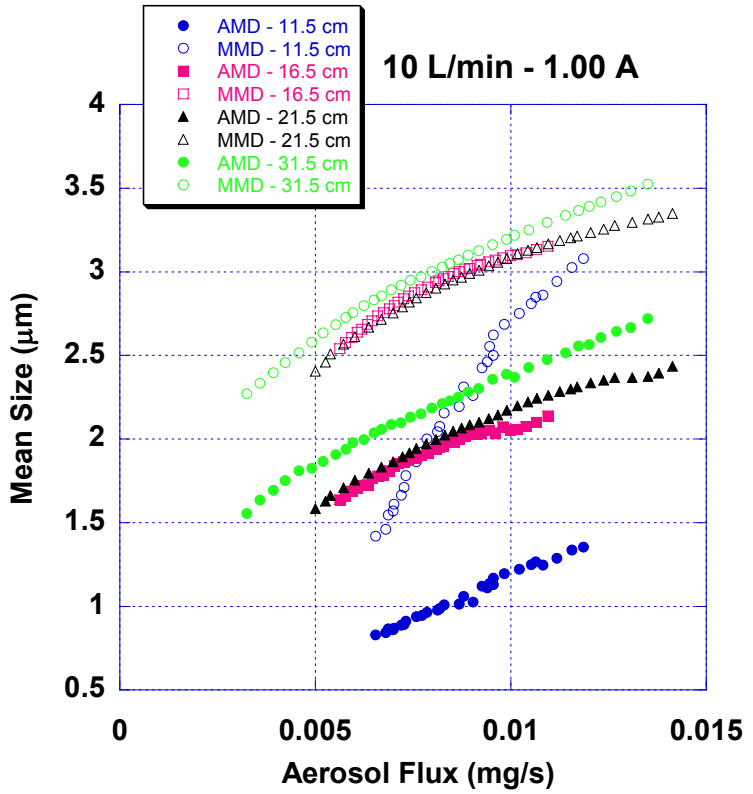

Figure B-14. Mean size as a function of flux.

(reported as Arithmetic Mean Diameter (AMD) and Mass Mean Diameter (MMD))

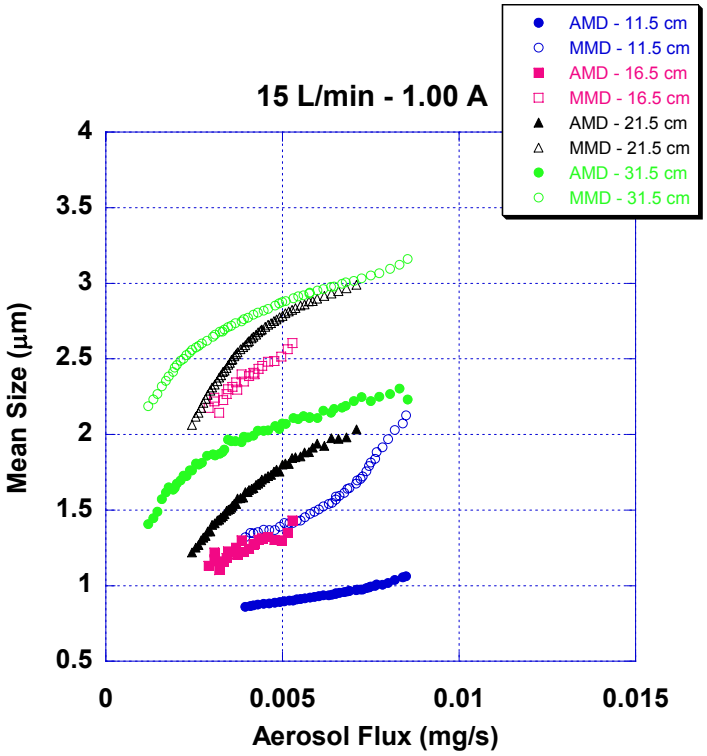

Figure B-15. Mean size a function of aerosol flux

(reported as Arithmetic Mean Diameter (AMD) and Mass Mean Diameter (MMD))

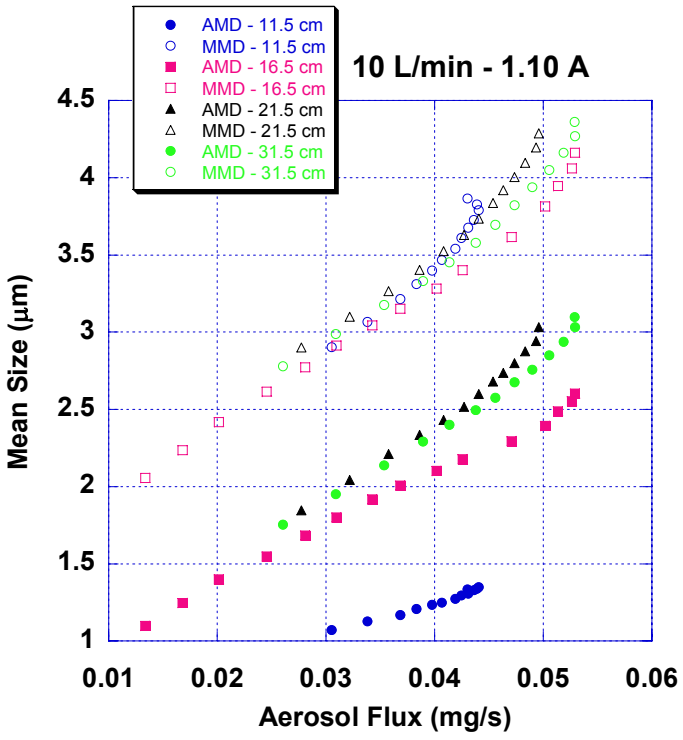

Figure B-16. Mean size as a function of flux

(reported as Arithmetic Mean Diameter (AMD) and Mass Mean Diameter (MMD))

Appendix C: Validation/demonstration of diagnostic systems

Size distribution and calibration measurements

For the ground-based experiments, we will use a suite of aerosol measurement instrumentation, which are not appropriate for flight because of the weight and size requirements and the complexity of operation. By using these instruments, we will be able to compare more accurate moment measures and complete size distribution characterizations with the results obtained using the flight instrumentation and data analysis method described above. The 0^{th}, 1^{st}, and 3^{rd} moments will be directly measured using a laboratory condensation particle counter (TSI model 3022a), an electrical aerosol detector (TSI model 3070a), and a tapered element oscillating microbalance (R&P model 1100). An electrical, low-pressure impactor (ELPI) will be used to measure aerosol size distributions. It records the size distribution over an aerodynamic diameter size range of 0.03 – 10 μm in 12 discrete channels. It has a temporal resolution on the order of 5 s. Additionally, a differential mobility analyzer with a condensation nucleus counter may be used to accurately size particles in the size range from 0.01 μm and 0.3 μm. This method involves charging of the aerosol and then separation based on the electrical mobility of the particle. Limited smoke samples will be collected using thermophoretic sampling for sizing by optical microscopy and transmission electron microscopy.

The condensation particle counter modified for the ISS experiments will be calibrated using singly charged aerosol particles that are counted independently by an aerosol electrometer. The 1^{st} moment measuring device, (ion chamber or other suitable instrument) will be calibrated with an electrical aerosol detector (EAD). The EAD uses a unipoloar corona charger to achieve an average charge level that is a known function of the particle diameter. The total aerosol charge is a function of the sum of the particle diameters (1^{st} moment). Its operating range is wider and its resolution is finer than that of a measuring ionization chamber. Calibration of the DustTrak™ is more involved for an arbitrary aerosol. If the aerosol to be measured has an invariant size distribution, then a single calibration parameter will relate the light scattering measure to the aerosol mass concentration. This is, in effect, the operating assumption of the device as used in field where it comes pre-calibrated for ISO test dust. Generally, the device sensitivity to particle diameter needs to be determined. This will be done be determining the response for monosize PSL spheres, and DOP particles. Computations based on light-scattering theory, using the parallel polarized diode laser light at 780 nm, a detector acceptance angle range (some range around 90^{o}), size, and refractive index of the aerosol particles will be performed to develop an instrument model that predicts measured results. An iterative procedure will be developed to determine the mass concentration of a particular smoke aerosol with an unknown size distribution using calibration data from 1-g tests with that smoke source, the 0^{th} and 1^{st} moments, and light scattering calculations.

Uncertainty estimates, and propagation of errors

The three primary diagnostic instruments used to measure the moments will be calibrated over operating ranges to within some quantified uncertainties. It is desired to make measurements at concentration levels where these uncertainties are low. For computed values a propagation of error approach to combine the individual uncertainties is performed. The computed arithmetic mean diameter ($d_{1,0} = M_1/M_0$), diameter of average mass ($d_{3,0} = (M_3/M_0)^{1/3}$), and the geometric standard deviation (σ_g, Equation 12) have uncertainties related to the individual moment uncertainties. The propagation of error formula (approximate, assuming covariance terms equal zero) is

$$S_Y = \sqrt{\left(\frac{\partial Y}{\partial X}\right)^2 S_x^2 + \left(\frac{\partial Y}{\partial Z}\right)^2 S_z^2 + \ldots} \qquad \text{(C-1)}$$

where s_y, s_x, and s_z are the standard deviations of the Y, X, and Z measurements. $\delta Y/\delta X$ is the partial derivative of the function Y with respect to X, etc. Table C-1 gives examples of propagation of error for various uncertainty measures of the moments and computed values of $d_{1,0}$, $d_{3,0}$, and σ_g of 3.0 μm, 4.0 μm, and 1.70.

Table C-1: Propagation of errors

Measure	Relative Standard Deviations (S_Y/Y) (%)				
M_0	10	5.0	5.0	2.5	10
M_1	10	5.0	2.5	5	10
M_3	10	5.0	10	10	20
$d_{1,0}$	14	7.0	5.6	5.6	14
$d_{3,0}$	4.7	2.4	3.7	3.4	7.5
σ_g	14	6.9	6.2	6.1	15

The uncertainty in the geometric standard deviation does not indicate the goodness of fit to a log-normal distribution, only the uncertainty of the computed value from the Hatch-Choate equations which assume a log-normal distribution. This exercise demonstrates that equal uncertainties in the moment measures do not translate into equal uncertainties in the computed values. Efforts that lead to reduction in the uncertainty of the 3rd moment are not as beneficial as equivalent reductions in either the 0th or 1st moments.